Early magmatic activity on the asteroid 4 Vesta inferred from chronology and geochemistry of HED meteorites

（HED 隕石の年代および化学組成から読み解く小惑星 4 ベスタの初期火成活動）

SAITO, Takaharu

（齊藤　天晴）

A dissertation for the degree of Doctor of Science
Department of Earth & Environmental Sciences,
Graduate School of Environmental Studies, Nagoya University

（名古屋大学大学院環境学研究科地球環境科学専攻学位論文　博士（理学））

2023

Acknowledgements

I would like to express my deepest gratitude to my supervisor, Professor Hiroshi Hidaka. He gave me an opportunity to be involved in isotope cosmochemistry, and has been greatly tolerant and supportive of me throughout my research life in Nagoya University. His suggestions often provided me different perspectives to the chemical data that I had never thought about. I am also deeply indebted to Dr. Keisuke Sakuma for his kind advises and supports to me. He has always been my role model as a cosmochemist since I was a stranger in this field. It has been a great honor for me to study with them.

I am very grateful to the past and present members of Geochemistry & Cosmochemistry Laboratory for their advises and encouragements to this study. Special gratitude I give to Professor Koshi Yamamoto and Associate Professor Yoshihiro Asahara for their kind advices and cooperations in ICP-MS and TIMS analysis at our laboratory.

Some parts of chemical analyses in this study are operated outside our laboratory for the better quality of the chemical data. Neodymium isotope work is supported by Dr. Shigekazu Yoneda (National Museum of Nature and Science, Tsukuba). Hafnium and nickel isotope works are supported by Dr. Seung-Gu Lee (Korea Institute of Geoscience and Mineral Resources, Korea). I am deeply grateful to them for their valuable cooperation in my experiments. Without their supports, the chemical data having sufficient quality for this study would never be obtained.

I am so grateful to Nakayama Foundation for their financial supports by providing a scholarship with me. I would like to express my deep appreciation to my parents, Takeshi Saito and Kayoko Saito, for their supports, understanding, and encouragements to my research life.

Abstract

Howardite–eucrite–diogenite meteorites are believed to originate in the crust of the asteroid 4 Vesta, whose differentiation processes are still controversial. Since Vesta is probably a remnant of protoplanets, its physical properties and internal structure provide fundamental information for understanding accretionary histories of terrestrial planets like Earth and Mars. One of the possible geochemical information to strongly constrain differentiation processes of HED meteorites is chronological data. Despite several decades of studies on HED meteorites, a chronology of diogenite is poorly established due to little compatibilities of typical diogenites to general isotopic dating methods. In this study, experimental methods for applying four dating systems of ^{60}Fe–^{60}Ni, ^{87}Rb–^{87}Sr, ^{146}Sm–^{142}Nd, and ^{176}Lu–^{176}Hf to HED meteorites are developed, and ^{87}Rb–^{87}Sr, ^{176}Lu–^{176}Hf analysis of HED meteorites are performed. In addition to the chronological data, trace element compositions and Sm and Gd isotopic shifts are also used for investigating chemical differentiation processes and cosmic ray exposure histories, respectively. the first ^{176}Lu–^{176}Hf isotopic data of nine diogenites are presented together with their ^{87}Rb–^{87}Sr isotopic compositions and trace element abundances to investigate the differentiation processes of diogenites.

The ^{176}Lu–^{176}Hf data sets of nine diogenites revealed the significantly higher initial ^{176}Hf/^{177}Hf ratio of diogenites than that of eucrites, while there are no resolvable differences between their crystallization ages. On the basis of high initial ratio and the early crystallization ages of diogenites (4.40 ± 0.38 Ga), their source material is estimated to be the Vestan mantle. The ^{87}Rb–^{87}Sr systematics of nine diogenites are entirely disturbed probably due to impact events on the parent body. The significant variation observed in the rare earth element abundances of nine diogenites suggests their crystallization from compositionally divers melts. On the basis of mantle origin and compositional diversity of diogenites, the crystallization of diogenites from partial melts of the Vestan mantle is proposed in this study. The variation of trace element abundances of diogenites can be explained by the variation of the degree of partial melting. The timescale between the crystallization and partial melting of the Vestan mantle is estimated to be ~100–600 Ma from the ^{176}Lu–^{176}Hf isotopic data of nine diogenites and

experimentally obtained mineral/melt partitioning coefficients of several elements, while a heat source for the partial melting is uncertain.

The Sm and Gd data sets of eucrites show significant isotopic shifts caused by (n,γ) type neutron capture reactions due to comic ray exposure. Neutron fluences of eucrites estimated from quantities of their ^{149}Sm–^{150}Sm shifts positively correlate with their CRE ages reported by previous studies. This indicates that cosmic ray exposures during the transition from Vesta to the Earth are dominant for eucrite and those on the surface of Vesta are limited. Except for a desert-find eucrite of DaG 480, model CRE ages of eucrites estimated from their neutron fluences can be attributed to CRE age clusters of eucrites. Significantly long model CRE age of this eucrite might reflect additional cosmic ray exposure on the Vestan surface.

Contents

1. Research background

1.1. HED meteorites and asteroid 4 Vesta

Terrestrial bodies in the solar system are believed to be established as a consequence of accumulation of gases and dusts that composed the solar protoplanetary disk. However, detailed processes that built dusts into planetary bodies are still in debate. The asteroid 4 Vesta, which is the second largest main belt object, is an important target for investigating the evolutionary history of terrestrial planets due to its several unique characteristics. Vesta is one of the differentiated rocky bodies in the solar system that is much smaller than the other rocky bodies, such as the Earth, the Moon, and Mars. Thus, Vesta provides evidence to investigate the scale dependences of the magmatic evolution processes of terrestrial planets. Another uniqueness of Vesta that arises from its small size is a considerably short period of magmatic activity (e.g., Sahijpal et al., 2007). Although the records of physicochemical processes (e.g., differentiation, magmatism, metamorphism, metasomatism, and impacts) on larger terrestrial planets within the first a few hundred million years of the solar system are entirely erased by later magmatic activities, Vesta preserves the records of such early processes because of its short magmatic activity. The information about these processes will allow us to estimate the environment of the earliest stage of terrestrial planets. Moreover, since Vesta is a remnant of protoplanets (e.g., Russell et al., 2012), its physical properties and internal structure will be fundamental information for understanding the accretionary history of terrestrial planets. In this study, the early differentiation processes of Vesta are investigated based on the geochemistry of howardite–eucrite–diogenite (HED) meteorites.

Material scientific evidence for investigating Vesta can be obtained from HED meteorites, which is the most abundant group of achondrites. HED meteorites are long believed to be surface materials of Vesta on the basis of the similarity of their reflectance spectra and dynamic link between Vesta (and Vestoids) and HED meteorites (e.g., McCord et al., 1970; Binzel and Xu, 1993). Furthermore, recent discoveries by the Dawn spacecraft confirmed that lithologic variation of the Vestan surface is similar to HED meteorites (e.g., Russell et al., 2012). Typical eucrites have two subgroups characterized by different petrological features. Basaltic eucrites are basaltic rocks composed of

plagioclase and low-Ca pyroxene, while cumulate eucrites are rarely found cumulate rocks with mineral compositions similar to those of basaltic eucrites. Diogenites are orthopyroxene-rich monomineralic cumulate rocks and a rarely found subgroup containing significant amount of olivine (> 10 vol%; Mittlefehldt, 2015) is generally called as olivine diogenite. Howardites are physical mixtures of fragments of eucrites and diogenites. In addition to HED meteorites, silicate phases of mesosiderites, which are differentiated meteorites that consist of almost equal amounts of silicates and Fe–Ni metal, are also believed to be originated in Vesta (e.g., Greenwood et al., 2006). At present, 1788 eucrites including 55 cumulate eucrites, 615 diogenites including 20 olivine diogenites, 457 howardites, and 349 mesosiderites are identified and approved by The Meteoritical Society (*Meteoritical Bulletin Database*, 2023).

Geochemical, mineralogical, and petrological studies of HED meteorites over several decades have partly revealed the geologic history of Vesta, while many problems still remain unsolved. Similar oxygen isotope compositions (e.g., Clayton and Mayeda, 1996; Greenwood et al., 2014) and comic ray exposure ages of HED meteorites (e.g., Eugster and Michel, 1994; Welten et al., 1997) indicate their break-up from a common parent asteroid (i.e., Vesta). Additionally, the similarity of oxygen isotope compositions of HEDs also suggests an occurrence of planetary-scale homogenization by the formation of global magma ocean on Vesta (e.g., Clayton and Mayeda, 1996; Greenwood et al., 2014). Siderophile element abundances of HEDs are consistent with the planetary-scale magma ocean as well (e.g., Steenstra et al., 2016). Highly siderophile element abundances of HEDs evidence inputs of chondritic materials into their source regions associated with the late accretion (e.g., Dale et al., 2012; Day et al., 2012). ^{40}Ar–^{39}Ar ages of HED meteorites record a period of highly frequent impacts on Vesta at 3.4–4.1 Ga probably related to the bombardment event that caused the lunar cataclysm (e.g., Bogard and Garrison, 2003; Marchi et al., 2013). Zircon U–Pb ages of eucrites revealed an occurrence of global crustal metamorphism on Vesta at 4554.5 ± 2.0 Ma (Iizuka et al., 2015a).

1.2. Differentiation models of HED meteorites

Although the differentiation processes of HED meteorites are still controversial, previous studies have provided two outstanding differentiation models of magma ocean model and partial melting model (Figure 1). The magma ocean model is firstly proposed by Mason (1962) and followed by numerous numbers of studies (e.g., Takeda, 1979; Righter and Drake, 1997; Ruzicka et al., 1997). Mason (1962) pointed out that major element compositions of pyroxenes in eucrites and diogenites are consistent with a sequence of crystallization products of a single igneous system. Eucrites, which are basaltic lava rocks, are formed as upper crust and diogenites, which are orthopyroxenitic cumulate rocks, are formed as lower crust. Later studies by Righter and Drake (1997) and Ruzicka et al. (1997) demonstrated that major element compositions of eucrites and diogenites are also consistent with the Mason's magma ocean model. The other model of partial melting is proposed by Stolper (1977) and Consolmagno and Drake (1977). They demonstrated that partial melting of chondritic materials can successfully explain rare earth element abundances in eucrites. On the basis of this finding, they suggested that eucrites are formed from partial melts of a chondritic primitive material, while diogenites represent residual phases of partial melting. However, at present, the magma ocean model is preferred to the partial melting model on the basis of strong evidence from oxygen isotopic compositions and siderophile element compositions of HED meteorites for the occurrence of a global magma ocean on Vesta (e.g., Greenwood et al., 2014; Steenstra et al., 2016). However, in the framework of the partial melting model, the magma ocean model can be interpreted as an extreme pattern showing high degree of partial melting. Hence, these two differentiation models do not conflict essentially, and even their combination is possible (e.g., large degree of partial melting followed by magma ocean differentiation).

On the basis of previous geochemical studies of eucrites, basaltic eucrites can be divided into three different subgroups of Main Group–Nuevo Laredo (MG–NL) trend, Stannern trend, and residual eucrites (e.g., Stolper et al., 1977; Barrat et al., 2007; Yamaguchi et al., 2009). The MG–NL trend group is most common eucrite and is characterized by wide variations in Mg# (molar ratio of Mg/[Mg + Fe] × 100), moderate variation in incompatible elements. These characteristics are interpreted as consequences

of source melt differentiations caused by fractional crystallization processes that produced MG–NL trend eucrites themselves (e.g., Stolper et al., 1977). The Stannern trend group is relatively rare subgroup and is characterized by similar Mg# to less evolved MG–NL trend eucrites, high incompatible element abundances, and significant negative Eu anomalies. These trace element characteristics are explained by contaminations of MG–NL parental melts by partial melts of the preexisting eucritic crust (Barrat et al., 2007). The residual eucrite group is characterized by strange trace element abundance patterns (e.g., well-pronounced light REE depletions and positive Eu anomalies; Yamaguchi et al., 2009). On the basis of these trace element characteristics, the residual eucrites are interpreted as residual phases of partial melting processes (Yamaguchi et al., 2009).

Considering trace element abundances of diogenites, differentiation processes of HED meteorites should be more complicated than the Mason's magma ocean model. This problem is firstly taken up by Fukuoka et al. (1977) and is addressed by following studies (e.g., Mittlefehldt, 1994; Mittlefehldt et al., 2012; Barrat et al., 2008; 2010; Barrat and Yamaguchi, 2014; Mandler and Elkins-Tanton, 2013). Although most of these studies reach a consensus that diogenites are formed from compositionally diverse multiple melts (not a single magma ocean), formation processes of the "compositionally diverse multiple melts" are still in debate. Barrat et al. (2010) demonstrated that a mixing of partial melts of magma ocean cumulates and eucritic crusts can produce the compositionally diverse melts and proposed formation of diogenites as crustal intrusions. However, Mittlefehldt et al. (2012) suggested that the involvements of eucritic melts are not required for the generation of the compositionally diverse melts.

A lithological map created from the Dawn's remote sensing data provides a further mystery about the differentiation processes of HED meteorites. In contrast to the predictions based on the magma ocean models (e.g., Righter and Drake, 1997; Ruzicka et al., 1997), olivine-rich mantle-like clasts are not found in a Vestan south pole region that exposes subsurface materials from a depth of ~60–100 km, but found in a north pole region that exposes materials from a depth of ~20 km (e.g., Ammannito et al., 2013a; 2013b; Clenet et al., 2014). Based on these observations, Clenet et al. (2014) proposed that the Vestan crust–mantle boundary is deeper than 80 km, which is extremely deep compared with Vestan radius of ~250 km. However, as mentioned in Haba et al. (2019),

considering incompatible element contents in eucrites (CI chondrite × ~10–10^2; e.g., Consolmagno and Drake, 1977; Barrat et al., 2007) and its occupancy in Vestan crust (>60%; Consolmagno et al., 2015), such a thick crust unrealistically requires at least two times higher bulk trace element contents of Vesta relative to those of CI chondrite (Anders and Grevesse, 1989). Therefore, the missing olivine on the Vestan south pole region probably reflects significant lateral heterogeneity of Vestan interior or large-scale disturbance of this region by catastrophic collisional event.

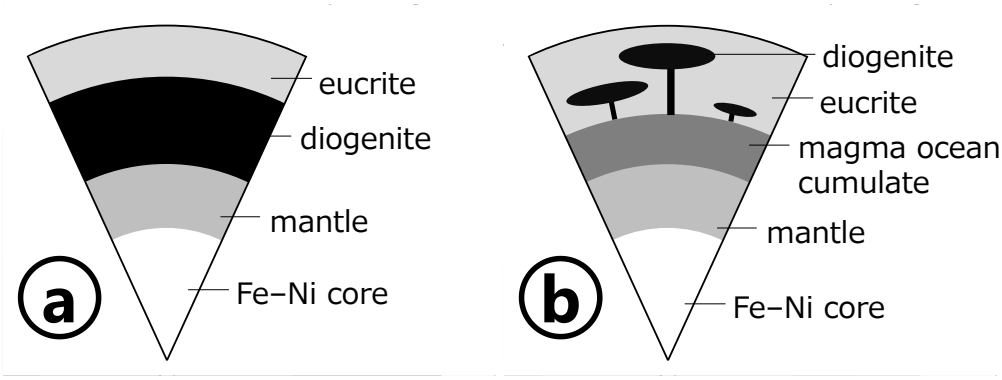

Figure 1. Schematics of (a) magma ocean model and (b) intrusion model for differentiation of HED meteorites.

1.3. Geochronology of HED meteorites

Although the temporal relationship between crystallizations of eucrites and diogenites is one of the key constraints for investigating the differentiation processes of HED meteorites, this relationship has not been established yet. Due to orthopyroxenitic monomineralic compositions and low incompatible element contents in diogenites, applications of the chronological approach using isotopic decay systems for diogenites are limited relative those of eucrites. Furthermore, published isotopic ages of diogenites (Table 1) are not necessarily consistent with each other. Although Takahashi and Masuda (1990) reported significantly younger ^{87}Rb–^{87}Sr ages of two diogenites than that of eucrites (Smoliar, 1993), Nakamura (1979) reported disturbed ^{87}Rb–^{87}Sr and ^{147}Sm–^{143}Nd systematics of four diogenites. Short-lived ^{26}Al–^{26}Mg chronometry indicates that three diogenites crystallized after the complete extinction of ^{26}Al, while eucrites crystallized before that (Hublet et al., 2017). Tang and Dauphas (2012) provided the ^{60}Fe–^{60}Ni isotopic data set of three diogenites exhibiting the correlation between $^{56}Fe/^{58}Ni$ ratios and ^{60}Ni excesses. However, the initial $^{60}Fe/^{56}Fe$ ratio of three diogenites is identical to that of eucrites within the error range corresponding to ~2 Ma. Noble gas ^{40}K–^{40}Ar and ^{40}Ar–^{39}Ar ages of diogenites show a broad range of ~1000–4500 Ma (Kaneoka et al., 1979; Michel and Eugster, 1994), probably representing timings of degassing by impact events. A recent Pb–Pb dating study by Schiller et al. (2014) provides the most reliable internal isochron ages so far for two diogenites (4546.4 ± 4.7 Ma for Dhofar 700 and 4484.5 ± 7.9 Ma for NWA 4215), which are significantly older than the internal Rb–Sr ages reported by Takahashi and Masuda (1990). They interpreted the younger Pb–Pb age of NWA 4215 as a record of secondary thermal events later than the primary crystallization of this diogenite. In contrast, the older Pb–Pb age recoded by Dhofar 700 are interpreted as the primary crystallization age of this diogenite. However, Pb–Pb age data are limited for only these two diogenites and detailed comparison with other age data is difficult at present.

Chronological data of diogenites are also important for detailed comparisons between differentiation models of HED meteorites and thermal evolution models of Vesta. A schematic comparison between the HED meteorite ages (Tang and Dauphas, 2012; Touboul et al., 2015) and thermal evolution model of Vesta (Neumann et al., 2014) is

shown in Figure 2. The differentiation events of Vesta are displayed along with age axis. Meteorite age in the figure represents the age of the events estimated from the geochronological age of HED meteorites obtained by isotopic dating approach. Age for thermal model represents the age of events estimated by numerical calculation approach. In general, the differentiation models based on geochemical approach (described in the section 1.2. Differentiation models of HED meteorites) and numerical calculation approach are difficult to compare directly because of the significant gap between the complexity of the processes that meteorites experienced and the simplification adopted in the numerical calculation approach. However, chronological data of meteorites enables quantitative comparisons between the differentiation models derived from experimental approach and the thermal evolution models derived from theoretical approach as shown in Figure 2.

Table 1. Published isotopic ages of diogenites.

Sample	Decay system	Age	Reference[a]
Noble gas age			
Ellemeet	^{40}K–^{40}Ar	1210 ± 500 Ma	ME
Garland	^{40}K–^{40}Ar	1230 ± 140 Ma	ME
	^{244}Pu–^{136}Xe	4525 ± 40 Ma	ME
Ibbenbühren	^{40}K–^{40}Ar	1600 ± 600 Ma	ME
Roda	^{40}K–^{40}Ar	1880 ± 250 Ma	ME
Shalka	^{40}K–^{40}Ar	4710 ± 500 Ma	ME
Tatahouine	^{40}K–^{40}Ar	4030 ± 2000 Ma	ME
Y 74013	^{40}K–^{40}Ar	1150 ± 250 Ma	ME
Y 74097	^{40}Ar–^{39}Ar	1100 ± 62 Ma	K
Y 75032	^{40}K–^{40}Ar	2930 ± 300 Ma	ME
Internal isochron age			
Dhofar 700	Pb–Pb	4546.4 ± 4.7 Ma	S2
Johnstown	^{87}Rb–^{87}Sr	4390 ± 35 Ma	TM
NWA 4215	Pb–Pb	4484.5 ± 7.9 Ma	S2
Tatahouine	^{87}Rb–^{87}Sr	4398 ± 28 Ma	TM
External isochron or model age			
Bilanga, Johnstown, and Tatahouine	^{26}Al–^{26}Mg	>7 Ma after CAI[b]	H
Bilanga, Tatahouine, and other 21 diogenites	^{26}Al–^{26}Mg	<3 Ma after CAI[c]	S1
Johnstown, Roda, and Tatahouine	^{87}Rb–^{87}Sr	4450 ± 180 Ma	BA
Johnstown, Shalka, and Tatahouine	^{60}Fe–^{60}Ni	identical to eucrite age[d]	TD
Johnstown and Tatahouine	^{87}Rb–^{87}Sr	4394 ± 11 Ma	TM
Johnstown, Tatahouine, and other 4 diogenites	^{53}Mn–^{53}Cr	4564.8 ± 0.9 Ma[e]	D, T

Notes. [a]BA: Birck and Allègre (1981), D: Day et al. (2012), H: Hublet et al. (2017), K: Kaneoka et al. (1979), ME: Michel and Eugster (1994), S1: Schiller et al. (2011), S2: Schiller et al. (2017), T: Trinquier et al. (2008), TD: Tang and Dauphas (2012), TM: Takahashi and Masuda (1990).
[b]This age represents timing of complete extinction of ^{26}Al.
[c]Model age.
[d]The initial ^{60}Fe/^{56}Fe ratio of $(3.31 \pm 0.28) \times 10^{-9}$ calculated from the isotope data set of the three diogenites is not converted to an absolute age due to controversial solar system initial ratio of ^{60}Fe/^{56}Fe.
[e]This external isochron age was calculated from an isotope data set that consists of not only diogenites but also eucrites and mesosiderites.

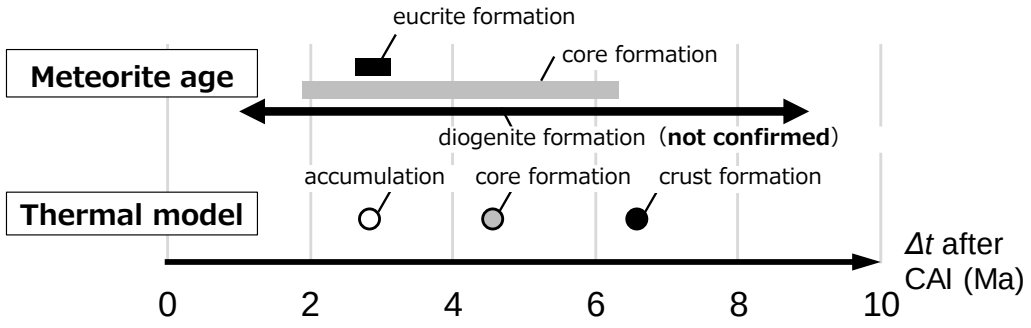

Figure 2. Comparison between timings of differentiation events on Vesta based on meteorite ages and theoretical thermal model. Thermal model is based on Neumann et al. (2014) and meteorite ages are from Touboul et al. (2015) and Tang and Dauphas (2012).

1.4. Approach of this study

As discussed above, chronological data of HED meteorites possibly provide key clues for constructing a differentiation model of Vesta. To obtain accurate and precise chronological data of HED meteorites (especially diogenites), four decay systems of ^{60}Fe–^{60}Ni, ^{87}Rb–^{87}Sr, ^{146}Sm–^{142}Nd, and ^{176}Lu–^{176}Hf systematics are adopted in this study. Since these four decay systems show different heat-resistance and resolution, their combination should be helpful for interpretation of chronological data. Experimental methods to apply these four decay systems to HED meteorites are developed, and ^{87}Rb–^{87}Sr and ^{176}Lu–^{176}Hf analysis of HED meteorites are carried out in this study. In addition to chronological data, REE abundances and Sm and Gd isotopic compositions of HED meteorites are also analyzed. REE abundances provide information about chemical differentiation processes. Sm and Gd isotopic compositions provide record of cosmic-ray exposure history of meteorite samples. Using these cosmochemical data of HED meteorites, possible models for early differentiation and magmatic activity on Vesta are discussed in this study.

2. Separation chemistry for Fe–Ni chronology

2.1. Introduction

Nickel is a moderately refractory and moderately siderophile element with five stable isotopes at mass numbers of 58, 60, 61, 62, and 64. Nickel isotope variability in meteorites provides cosmochemical perspectives of chronology and nucleosynthetic heterogeneity of early solar system objects. ^{60}Fe–^{60}Ni decay system has been used to determine relative chronology of early solar system objects since a discovery of radiogenic excesses in ^{60}Ni derived from a short-lived nuclide ^{60}Fe ($t_{1/2}$ = 2.62 Myr; Rugel et al., 2009) by Shukolyukov and Lugmair (1993a,b). This decay system is especially useful for dating differentiated stony meteorites (i.e., achondrites) because their Fe/Ni ratios were elevated by removal of siderophile elements following metal–silicate segregation on their parent bodies. Non-radiogenic stable isotope anomalies of Ni in primitive meteorites (i.e., chondrites) and their components (e.g., chondrules, matrices, and calcium–aluminum-rich inclusions) provide some constraints on nucleosynthetic sources that contributed to the early solar system (e.g., Elliott and Steele, 2017; Nanne et al., 2019; Regelous et al., 2008; Render et al., 2018; Steele et al., 2012).

Although earlier Ni isotopic works were performed on thermal ionization mass spectrometry (TIMS) (e.g., Birck and Lugmair, 1988; Morand and Allègre, 1983; Shimamura and Lugmair, 1983; Shukolyukov and Lugmair, 1993a,b), currently, most studies employ multi-collector inductively coupled plasma mass spectrometry (MC-ICP-MS) for Ni isotope measurements (e.g., Chernonozhkin et al., 2015; Quitté et al., 2006; 2011; Quitté and Oberli, 2006; Regelous et al., 2008; Render et al., 2018; Tang and Dauphas, 2012). Because of high first ionization potential of Ni (737 kJ/mol), MC-ICP-MS provides significantly efficient ionization of Ni relative to TIMS and, therefore, is more suitable for high-precision isotope measurements. For accurate and precise Ni isotope measurement using MC-ICP-MS, high-quality Ni purification is required for eliminating interferences from matrix elements.

Magnesium is one of the elements that is difficult to separate from Ni, while large numbers of typical rock-forming minerals (e.g., olivine, pyroxene, amphibole, and mica) contain Mg as a major element. For purifying Ni from Mg and most other matrix elements,

generally, an Ni-specific chelating agent of dimethylglyoxime (DMG) is used in solvent extraction (e.g., Morand and Allègre, 1983; Shimamura and Lugmair, 1983; Quitté and Oberli, 2006) and in eluent phase for cation-exchange chromatography (e.g., Chernonozhkin et al., 2015; Gall et al., 2012; Klaver et al., 2020; Regelous et al., 2008; Victor, 1986; Wahlgren et al., 1970; Wu et al., 2019). DMG and Ni forms an insoluble chelate complex at pH = ~8–9 and the Ni–DMG complex can be extracted by organic solvents. An Ni-specific extraction chromatography resin of Nickel Resin (available from Eichrom Technologies) also contains DMG and uses the same chelating reaction as conventional solvent extraction method. These methods can separate Ni efficiently from almost all matrix elements due to selective complexation of Ni–DMG. However, a strong coordinate bond of Ni–DMG also causes a technical issue after the separation chemistry. Since the Ni–DMG bonding is difficult to dissociate through simple ionic reactions, a decomposition of DMG with strong oxidizing agents (e.g., perchloric acid, aqua regia, and nitric acid) is necessary before an isotopic analysis (e.g., Spivak-Birndorf et al., 2018). This decomposition treatment demands an enormous effort. Furthermore, if the decomposition is insufficient, residual DMG may cause several types of non-spectral interferences at an isotope measurement by MC-ICP-MS (e.g., Hughes et al., 2011; Teng and Yang, 2013). While there are a few Ni separation procedures that do not use DMG (e.g., Cook et al., 2006; Ireland et al., 2013; Moynier et al., 2007; Steele et al., 2011; Tang and Dauphas, 2012; Beunon et al., 2020), most of them are applicable only to specific types of samples or requires some special experimental equipment.

Recently, a unique DMG-free Ni separation protocol was developed by Spivak-Birndorf et al. (2018) and Render et al. (2018). They found that a combination of hydrochloric acid–acetic acid mixture with cation-exchange resin provides a sufficient separation between Mg and Ni. However, despite its obvious advantages owing to the elimination of the use of DMG, application of their Ni separation method is limited only to Ni-rich (range of Ni contents was ~0.1–30 wt%) geological samples (dunites and hydrous Ni–Mg silicates, Spivak-Birndorf et al., 2018; a bulk carbonaceous chondrite and Ca–Al-rich inclusions, Render et al., 2018). Since ^{60}Fe–^{60}Ni decay system is based on isotopic excess derived from β^- decay of ^{60}Fe onto ^{60}Ni, it is more beneficial to date samples showing higher Fe/Ni ratios such as achondrites. Thus, the application of their Ni separation method to Ni-poor samples largely enhances its usefulness for the ^{60}Fe–

^{60}Ni dating. In this study, we improved the DMG-free separation method developed by Spivak-Birndorf et al. (2018) and Render et al. (2018) for expanding its applications to Ni-poor silicate samples (e.g., achondrites and especially HED meteorites).

2.2. Experiments

2.2.1. Distribution coefficients of elements between cation-exchange resin and HCl–acetic acid mixture

To identify the optimum condition for the Mg–Ni separation, cation-exchange behavior of Mg, Al, Ca, Ti, and Ni in HCl–acetic acid mixture was analyzed at variable mixing proportions of HCl and acetic acid. The proportions tested in this study are combinations of 0.9, 1.2, 1.5, and 1.8 M HCl with 0, 20, 40, 60, 75, and 85 vol% acetic acid. Cation-exchange resin (Bio-Rad Laboratory, AG50W-X8, 200–400 mesh, ~0.1 mg) and HCl–acetic acid mixture (~5 g) containing Mg, Al, Ca, Ti, and Ni were put into a reaction beaker. After an equilibration for ~12 hours, the HCl–acetic acid mixture was collected from the beaker. This collected fraction was evaporated once and redissolved in 2% HNO_3. Finally, this sample solution was analyzed by a quadruple ICP-MS (Agilent 7700x) for the determination of elemental abundances. The elemental abundances obtained in the ICP-MS analysis was converted to distribution coefficients using a following equation,

$$K_{\mathrm{d}} = \frac{M_{\mathrm{resin}}/W_{\mathrm{resin}}}{M_{\mathrm{sol}}/W_{\mathrm{sol}}} = \frac{(M_{\mathrm{tot}} - M_{\mathrm{sol}})/W_{\mathrm{resin}}}{M_{\mathrm{sol}}/W_{\mathrm{sol}}},$$

where K_{d} represents a distribution coefficient of a certain element between the cation-exchange resin and HCl–acetic acid mixture, M_{resin} and M_{sol} are a weight of an element contained in the resin and solution, respectively, M_{tot} is a total weight of an element put into the reaction beaker, and W_{resin} and W_{sol} are a weight of the resin and solution, respectively.

2.2.2. Separation chemistry

Nickel separation chemistry of this study consists of four steps of ion-exchange chromatography including both cation- and anion-exchange (Table 2). Detailed descriptions for the individual separation steps are shown below.

Step 1: The first step of the separation chemistry is removal of V, Cr, Mn, Fe, Co, Cu, Zn, Cd, and Sn by cation-exchange with HCl–acetone mixture. This step is adapted from Spivak-Birndorf et al. (2018) and Render et al. (2018). A cation-exchange resin (Bio-Rad Laboratory, AG50W-X8, 200–400 mesh, 2 mL) packed in polypropylene

column (Eichrom Technologies, 40 mm length, 8 mm inner diameter) was used for this purpose. After a cleaning and conditioning with 20 mL of H_2O, 10 mL of 6 M HCl, 5 mL H_2O, 5 mL of 2 M HCl–80% acetone mixture (i.e., 1 mL of 10 M HCl + 4 mL of acetone; hereafter "HCl–acetone"), a sample solution dissolved in 3 mL of HCl–acetone was loaded onto the resin. This sample solution was equilibrated in 10 M HCl once and was diluted by acetone just before the loading to promote a coordination of Cr^{3+}–Cl^-. This treatment significantly affects a quality of Cr–Ni separation since Cl^--coordinated Cr-species show significantly lower affinity for a cation-exchange resin relative to that of Ni while the affinity of Cl^--free Cr^{3+} is similar to that of Ni (Larsen et al., 2016; 2018). After the sample loading, V, Cr, Mn, Fe, Co, Cu, Zn, Cd, and Sn were washed out with additional 22 mL of HCl–acetone and 2 mL of H_2O. Nickel and matrix elements of Mg, Al, Ca, and Ti were collected by 5 mL of 6 M HCl.

Step 2: The second step of the separation chemistry is removal of Mg, Al, Ca, and Ti by cation-exchange with HCl–acetic acid mixture. This step is modified after Spivak-Birndorf et al. (2018) and Render et al. (2018). The column used in this step is the same as that of the step 1. After a cleaning and conditioning with 20 mL of H_2O, 10 mL of 6 M HCl, 5 mL of H_2O, and 5 mL of 1.5 M HCl–85% acetic acid mixture (i.e., 0.75 mL of 10 M HCl + 4.25 mL of acetic acid; hereafter "HCl–acetic acid"), the Ni fraction from the step 1 redissolved in 3 mL of HCl–acetic acid was loaded onto the resin. Nickel and matrix elements of Na and K were collected by additional 15 mL of HCl–acetic acid while Mg, Al, Ca, and Ti were retained to the resin. These residual matrix elements were eluted from the resin with 10 mL of 6 M HCl. The Ni fraction collected in this step was processed by hot aqua regia (~100°C) for a decomposition of organic compounds probably derived from acetone and acetic acid.

Step 3: The third step of the separation chemistry is removal of Na and K and clean-up of Cr by cation-exchange with HCl and HNO_3. This step is adapted from Larsen et al. (2018). A cation-exchange resin (Bio-Rad Laboratory, AG50W-X8, 200–400 mesh, 0.5 mL) packed in glass column (40 mm length, 4 mm inner diameter) was used for this purpose. After the cleaning and conditioning with 10 mL of H_2O, 2.5 mL of 6 M HCl, and 2.5 mL of 0.5 M HCl, the Ni fraction from the step 2 redissolved in 4 mL of 0.5 M HCl was loaded onto the resin. For an efficient removal of Cr, this sample solution was equilibrated in 10 M HCl once and was diluted by H_2O just before the loading to promote

a coordination of Cr^{3+}–Cl^{-} (Larsen et al., 2016; 2018). Sodium, K, and Cr were washed out with 10 mL of 0.5 M HNO_3 and 0.5 mL of H_2O. Nickel was collected by 3.5 mL of 6 M HCl.

Step 4: The fourth step of the separation chemistry is clean-up of Fe and Zn, who have isobars for Ni isotopes (^{58}Fe to ^{58}Ni and ^{64}Zn to ^{64}Ni), by anion-exchange with HCl. This step is adapted from Chernonozhkin et al. (2015) and Render et al. (2018). An anion-exchange resin (Bio-Rad Laboratory, AG1-X8, 200–400 mesh, 0.5 mL) packed in glass column (40 mm length, 4 mm inner diameter) was used for this purpose. After a cleaning and conditioning with 10 mL of H_2O, 2.5 mL of 0.5 M HNO_3, 2.5 mL of 0.5 M HCl, and 3 mL of 6 M HCl, the Ni fraction from the step 3 dissolved in 3.5 mL of 6 M HCl was loaded onto the resin. Nickel was collected with additional 3.5 mL of 6 M HCl while Fe and Zn were retained to the resin. After a decomposition of residual organic compounds by aqua regia, this Ni fraction was redissolved in 2% HNO_3 for the isotope measurement by MC-ICP-MS.

For confirming elution behavior of elements in the separation chemistry, a mixture of single-element standard solutions of Na, Mg, Al, K, Ca, Ti, V, Cr, Mn, Fe, Co, Ni, Cu, Zn, Cd, and Sn was used as a test sample. This test sample was loaded onto the column and the eluents were collected at 1 mL interval. The collected eluents are measured by a quadrupole ICP-MS (Agilent 7700x) and atomic absorption spectrophotometer (Hitachi A-2000) to determine the relative abundances of the elements listed above.

Table 2. Four-step Ni purification chemistry.

Step	Volume	Eluent	Element
Step 1 (2 mL, AG50W-X8, 200–400 mesh, 8 mm inner diameter, 40 mm length)			
Washing	20 mL	H_2O	
	10 mL	6 M HCl	
	5 mL	H_2O	
Conditioning	5 mL	HCl-acetone[b]	
Loading sample[a]	3 mL	HCl-acetone[b]	V, Cr, Mn, Fe, Co, Cu, Zn, Cd, and Sn
Eluting matrix	22 mL	HCl-acetone[b]	
	2 mL	H_2O	
Collecting Ni	5 mL	6 M HCl	Mg, Al, Ca, Ti, and Ni
Step 2 (2 mL, AG50W-X8, 200–400 mesh, 8 mm inner diameter, 40 mm length)			
Washing	20 mL	H_2O	
	10 mL	6 M HCl	
	5 mL	H_2O	
Conditioning	5 mL	HCl-acetic acid[c]	
Loading sample	3 mL	HCl-acetic acid[c]	
Collecting Ni	15 mL	HCl-acetic acid[c]	Na, K, and Ni
Collecting matrix	5 mL	6 M HCl	Mg, Al, Ca, Ti, REE, Hf...
Step 3 (0.5 mL, AG50W-X8, 200–400 mesh, 4 mm inner diameter, 40 mm length)			
Washing	10 mL	H_2O	
	2.5 mL	6 M HCl	
Conditioning	2.5 mL	0.5 M HCl	
Loading sample[a]	4 mL	0.5 M HCl	
Eluting matrix	10 mL	0.5 M HNO_3	Na, K, and minor Cr
	0.5 mL	H_2O	
Collecting Ni	3.5 mL	6 M HCl	Ni
Step 4 (0.5 mL, AG1-X8, 200–400 mesh, 4 mm inner diameter, 40 mm length)			
Washing	10 mL	H_2O	
	2.5 mL	0.5 M HNO_3	
	2.5 mL	0.5 M HCl	
Conditioning	2.5 mL	6 M HCl	
Loading sample[d]	3.5 mL	6 M HCl	Ni
Collecting Ni	3 mL	6 M HCl	

[a]This sample solution was equilibrated in 10 M HCl and diluted just before (~30 min) the loading.
[b]2 M HCl–80% v/v acetone mixture (600 μL of 10 M HCl + 2400 μL of acetone). Prepared freshly.
[c]1.5 M HCl–85% v/v acetic acid mixture (450 μL of 10 M HCl + 2550 μL of acetic acid).
[d]This fraction was collected together with lower one.

2.3. Results and discussion

2.3.1. Distribution behavior of metal cations between cation-exchange resin and HCl–acetic acid mixture

Figure 3 shows distribution coefficients of Mg, Al, Ca, Ti, and Ni between the cation-exchange resin and HCl–acetic acid mixture measured in this study. The horizontal axis represents volume fraction of acetic acid. For example, 0 vol% in Figure 3 means that the solvent is pure 0.9 M HCl and 60 vol% means that the solvent is composed of 450 μL of 10 M HCl, 1550 μL of H_2O, and 3000 μL of acetic acid (i.e., 5000 μL of 0.9 M HCl–60 vol% acetic acid).

As shown in Figure 3, when the fraction of acetic acid is low (<60 vol%), affinities of all five elements studied here (Mg, Al, Ca, Ti, and Ni) for the cation-exchange resin increase along with addition of acetic acid. In contrast, when the fraction of acetic acid is high (>60 vol%), an affinity of Ni for the resin declines rapidly along with addition of acetic acid while those of Mg, Al, Ca, and Ti remain increasing or decline gradually. Consequently, the discrepancy between distribution coefficient (K_d) of Ni and other four elements gets larger at higher fraction of acetic acid. Comparing this trend among Figure 3a–d, the declining of K_d of Ni is more notable at higher concentration of HCl. Thus, higher concentration of both of acetic acid and HCl provides better separation of Ni from other four elements. This effect is observed not only in acetic acid but also in other typical organic solvents and is interpreted as a consequence of enhancement of electrostatic interaction in the resin–solvent system (e.g., Korkisch, 1966; Korkisch and Ahluwalia, 1967; Strelow et al., 1971). Most organic solvents show less permittivity relative to water (e.g., water, ε_r = 78.3; ethanol, ε_r = 24.5; acetone, ε_r = 20.7; acetic acid, ε_r = 6.15). Thus, an addition of organic solvent decreases the net permittivity of water–organic solvent medium. According to Coulomb's law, this enhances electrostatic interactions in the solvent. As for cation-exchange with hydrochloric acid–organic solvent medium, an addition of organic solvent to hydrochloric acid probably causes a competing between enhanced cation–resin and cation–Cl^- ionic bonding. An enhancement of a cation–resin bonding results in an increase of affinity for the resin while that of a cation–Cl^- bonding results in a decrease of the affinity. For most metal cations (including Mg, Al, Ca, Ti, Ni), enhancement of a cation–resin bonding is predominant at low fraction of organic solvent

and, contrary, that of a cation–Cl^- bonding turns to prominent along with addition of organic solvents (e.g., Korkisch, 1966; Korkisch and Ahluwalia, 1967; Strelow et al., 1971). Since a mode of this competing effect differs from element to element, hydrochloric acid–organic solvent medium provides much better separation for several metal elements compared with aqueous hydrochloric acid. Figure 4 shows distribution coefficients of Mg, Al, Ca, Ti, and Ni between the cation-exchange resin and 1.0 M HCl–acetone mixture measured in previous study (Strelow et al., 1971). The K_d value of Ni shows the decline at high fraction of acetone (Figure 4) as well as that in HCl–acetic acid (Figure 3). However, the decline in HCl–acetic acid is more pronounced than that in HCl–acetone. Thus, acetic acid provides better separation between Mg and Ni relative to acetone. This is probably due to the difference in permittivity of acetic acid and acetone. Owing to its relatively low permittivity, acetic acid (ε_r = 6.15) can decrease the net permittivity of the mixture with HCl more largely compared with acetone (ε_r = 20.7).

2.3.2. Evaluation of the separation chemistry

Figure 5 shows the elution behavior of important elements for the Ni isotope analysis in four step resin chemistry of this study. The horizontal axis represents cumulative volume of eluent that was loaded onto the column. The vertical axis shows relative fraction of elements that eluted from the column. The total blank throughout the separation chemistry of this study is <2 ng. This blank level is negligible compared with the amount of Ni contained in the samples (~1–2 μg, blank contribution is <0.1%). The recovery yield of Ni is ~80%.

2.3.2.1. The optimum condition for Mg–Ni separation

As mentioned above, the K_d value of Ni gets lower at higher fraction of acetic acid and higher molarity of HCl while those of Mg, Al, Ca, and Ti are relatively stable (Figure 3). Thus, HCl–acetic acid mixture that contains higher amount of acetic acid and HCl provides better separation between Ni and other four elements. Furthermore, low K_d value of Ni is beneficial for eluting Ni with practical amount of the solvent in column chromatography method. Among 24 mixing proportions between HCl and acetic acid tested in this study, 1.8 M HCl–85 vol% acetic acid may be optimum for Mg–Ni separation. However, highly concentrated and pure HCl is difficult to prepare and handle.

Thus, two mixing proportions of 1.5 M HCl–85 vol% acetic acid and 1.8 M HCl–85 vol% acetic acid were tested. Figure 6 shows the elution behaviors of Mg and Ni in the separation step 2 performed with (a) 1.5 M HCl–85 vol% acetic acid and (b) 1.5 M HCl–85 vol% acetic acid. Both of two mixing proportions provides a sufficient separation between Mg and Ni and there are no significant differences in their elution profiles. In this study, for the ease of handling, the 1.5 M HCl–85 vol% acetic acid was employed as an eluent for the separation step 2.

2.3.2.2. Elution behavior of Cr

The elution curve of Cr in the separation step 1 consists of three different peaks probably corresponding to Cr-species of $CrCl_3$ + $CrCl_2^+$, $CrCl^{2+}$, and Cr^{3+} (Figure 7). This unique elution behavior of Cr is due to slow ligand exchange kinetics of Cr^{3+} and differences in the affinities to the cation-exchange resin among the Cl^--coordinated Cr-species (Cr^{3+} > $CrCl^{2+}$ > $CrCl_2^+$ > $CrCl_3$; e.g., Larsen et al., 2016; 2018). In the cation-exchange with HCl media, Cl^--free Cr (i.e., Cr^{3+}) shows the partitioning behavior similar to Ni (e.g., Larsen et al., 2016; 2018). Hence, Cr and Ni are difficult to separate thoroughly only by the step 1. As shown in Figure 7, the fraction of Cr involved into the Ni collection is ~2% of the total. This amount of Cr probably causes no significant effects on the Ni isotope measurements for Ni-rich samples (e.g., chondrites, chondrules, and CAIs), while this is not the case for Ni-poor samples (e.g., achondrites). Typical chondrites show Cr/Ni ratios of ~0.18–0.36 (mean compositions of chondrite groups; Wasson and Kallemeyn, 1988), which will decrease to <0.008 (0.36 × 2%) after the separation. According to previous works that tested the matrix effects on the Ni isotope measurements (e.g., Spivak-Birndorf et al., 2018; Tang and Dauphas, 2012), Cr/Ni < 1 is sufficient for the accurate and precise analysis. Thus, the residual Cr after the separation is not problematic for chondritic (i.e., Ni-rich) samples and the previous works (Spivak-Birndorf et al., 2018; Render et al., 2018) paid little attention to Cr. In contrast to chondrites, howardite–eucrite–diogenite (HED) meteorites, the most abundant subgroup of achondrite, show Cr/Ni ratios of ~10–500 (Mittlefehldt, 2015), which will decrease to <10 (500 × 2%) after the separation. Even though Cr is not a critical interfering element for Ni, such a large amount of Cr probably causes several types of non-spectral

interferences at the isotope measurement; for instance, ionization interference, space charge effect, and obstruction of the orifice of plasma–vacuum interface.

For improving the Cr–Ni separation, the cation-exchange chemistry of Larsen et al. (2018) was adopted as the step 3 of the separation chemistry of this study (Table 2). As mentioned above, unlike Cl^--free Cr(III), chlorinated Cr(III) species can be separated from Ni in cation-exchange chemistry with HCl (Figure 7). Hence, Cr–Ni separation can be improved by increasing fraction of chlorinated Cr(III) species in the sample solution. According to the thermodynamic calculation with PHREEQC (Parkhurst and Appelo, 2013) conducted by Larsen et al. (2016), the fraction of Cl^--free Cr(III) can be decreased to nearly 0% in hot (>120°C) concentrated (>6 mol/L) HCl. Furthermore, owing to slow ligand-exchange rate of Cr(III), the chlorinated Cr(III) does not dissociate to Cl^--free Cr(III) immediately after the solution is cooled and diluted by water (Larsen et al., 2016). In this study, on the basis of these calculation and observation, Cr elution behavior in the separation step 3 was investigated to find appropriate experimental condition to achieve sufficient Cr–Ni separation.

Figure 8 shows elution profiles of Cr-species in four different experimental conditions; (a) Cr was dissolved in 10 M HCl and heated at 120°C overnight

In this separation step, the fraction of Cr involved into the Ni collection is ~0.8% (see Figure 5c). Thus, a combination of the step 1 and step 3 provides a removal of nominally ~99.98% Cr. Applying both of the two separation steps to HED meteorites, Cr/Ni ratios will decrease to <0.08, which is sufficient for avoiding significant interferences from Cr.

2.3.2.3. Elution behavior of Mg

For the Ni isotope analysis of Ni-poor planetary materials, large amounts of the samples should pass through the chromatographic column to obtain sufficient amount of Ni. In this case, the adsorption capacity of the ion-exchange resin becomes a critical factor for the attainment of sufficient separation, especially in the separation step 2. In this separation step, Al, Mg, and Ca, which are major constituents of rock-forming minerals, should be retained on the resin while Ni is eluted (Figure 5b). However, if the amount of Mg loaded onto the resin exceeds its adsorption capacity, Mg may elute from the resin

together with Ni. Hence, the Mg adsorption capacity of the resin was investigated prior to dealing with natural rock samples.

As shown in Figure 9, an elution peak of Mg appears at smaller eluent volume when larger amount of Mg is loaded onto the resin. This elution behavior of Mg can be attributed to an ion-adsorption capacity of the cation-exchange resin. The nominal wet capacity of the AG50W-X8 cation exchange resin of 2.0 mEq/mL (Bio-Rad Laboratory) corresponds to ~24 mg/mL of Mg. In the case of the separation step 2 of this study, which 2 mL of the cation-exchange resin is used in, the capacity is equal to ~48 mg of Mg. The amount of Mg loaded onto resin here is comparable with this capacity. Thus, when 15 mg of Mg was loaded onto the resin, its adsorption capacity was probably saturated. This idea is also consistent with the fact that the elution peak of Mg is not gaussian but trapezoidal (Figure 9c). Judging from the three elution curves obtained in this study (Figure 9), <10 mg of Mg is not problematic for the Mg–Ni separation, which corresponds to <0.8 mEq. Since typical stony meteorite contain ~10% of Mg, this amount is equal to ~100 mg of meteorites samples. For analyzing meteorite samples whose weight exceed 100 mg, the sample should be divided so that the adsorption capacity of the resin is not saturated.

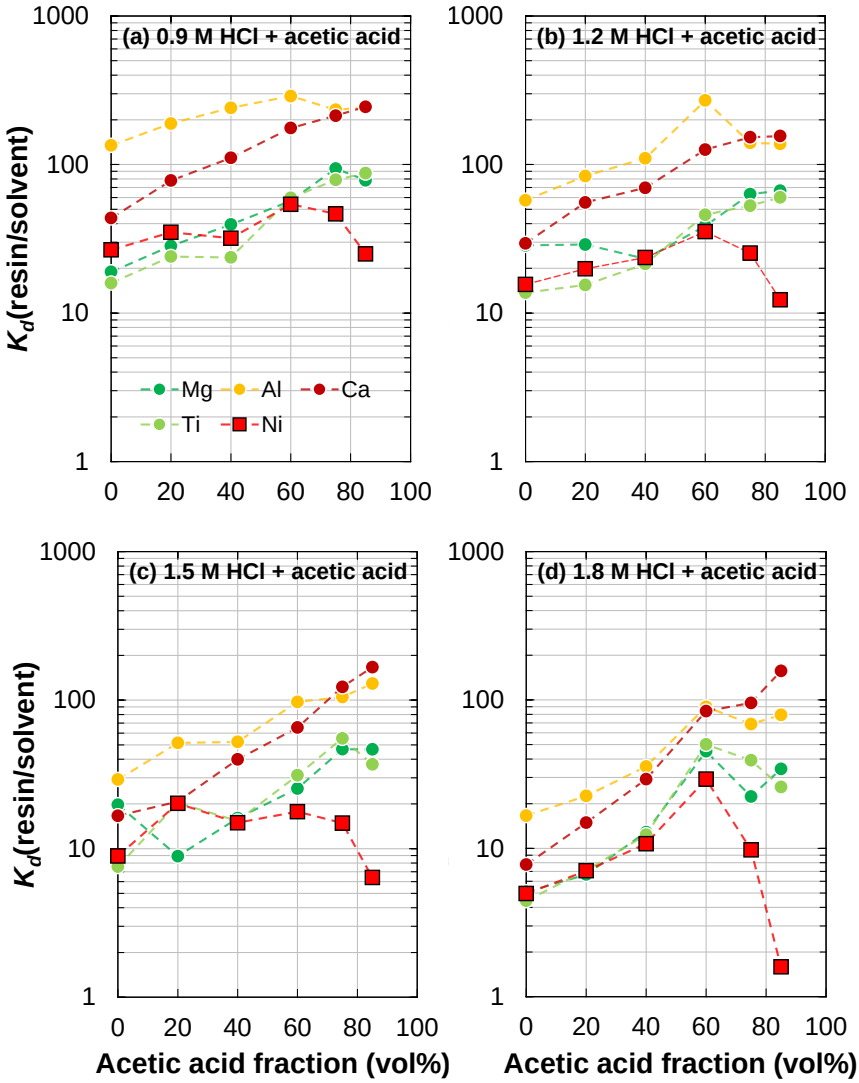

Figure 3. Distribution coefficients of Mg, Al, Ca, Ti, and Ni between AG50W-X8 cation exchange resin and HCl–acetic acid mixture.

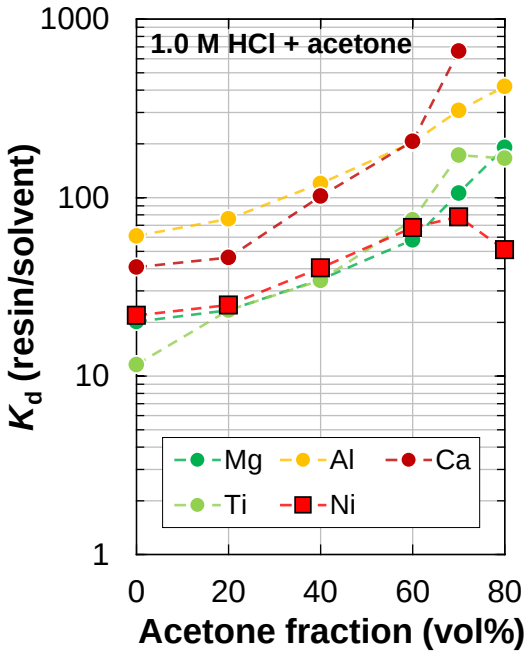

Figure 4. Distribution coefficient of Mg, Al, Ca, Ti, and Ni between AG50W-X8 cation-exchange resin and HCl–acetone mixture. Data is from Strelow et al. (1971).

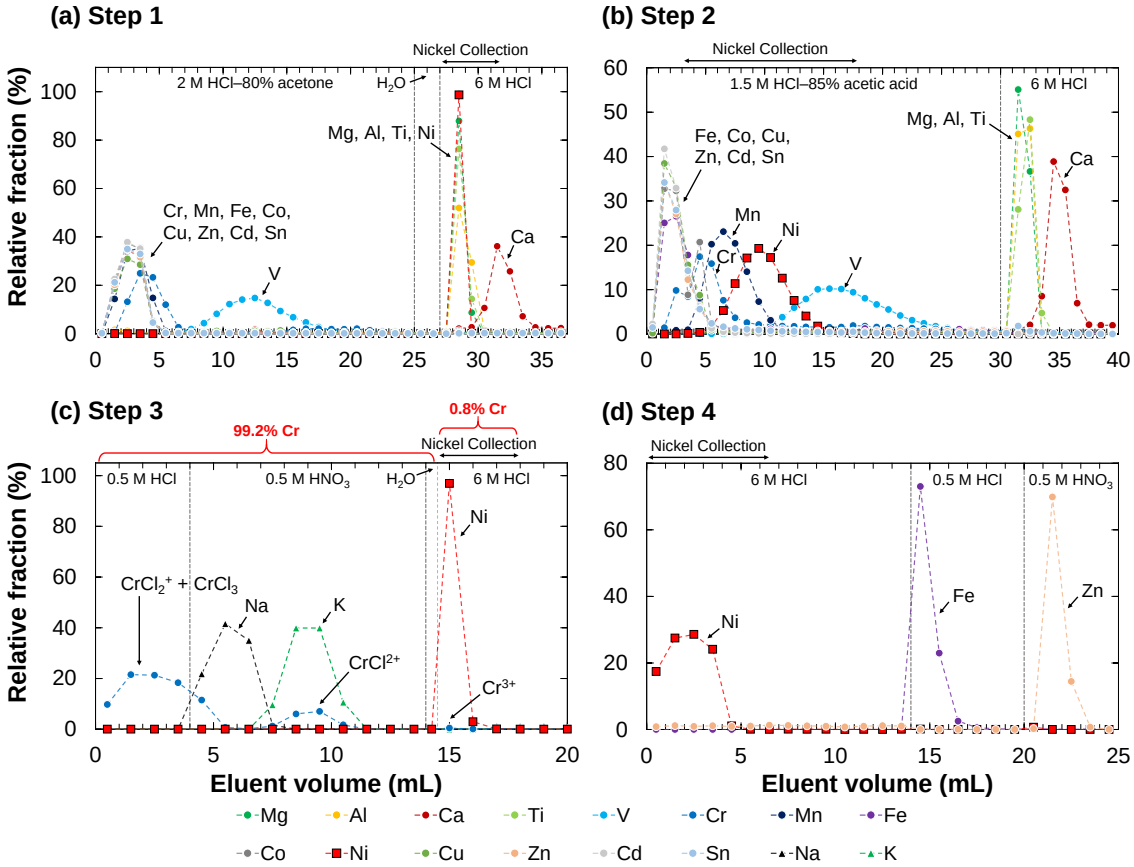

Figure 5. Elution curves for the four-step separation chemistry of this study.

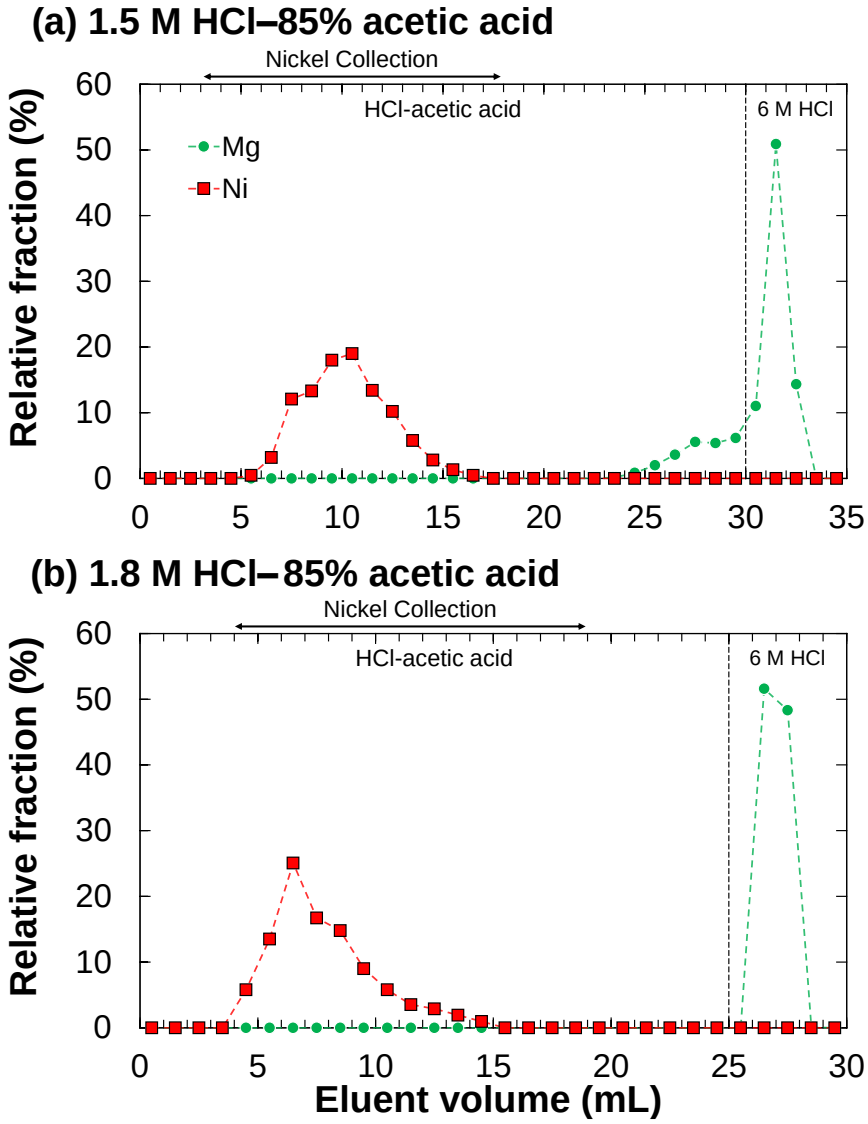

Figure 6. Elution behavior of Mg and Ni in the separation step 2 performed with (a) 1.5 M HCl and (b) 1.8 M HCl.

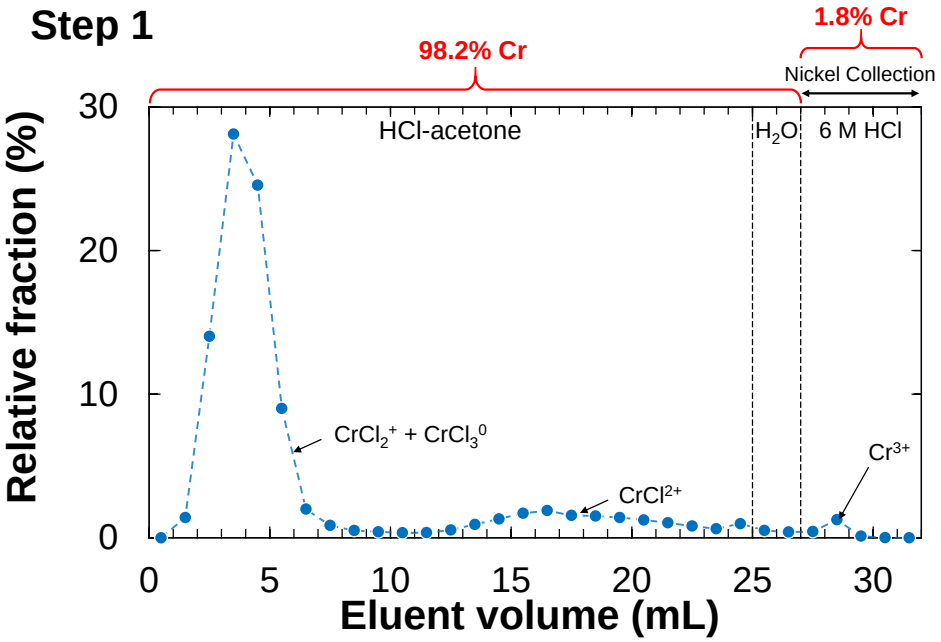

Figure 7. Elution behavior of Cr in the separation step 1.

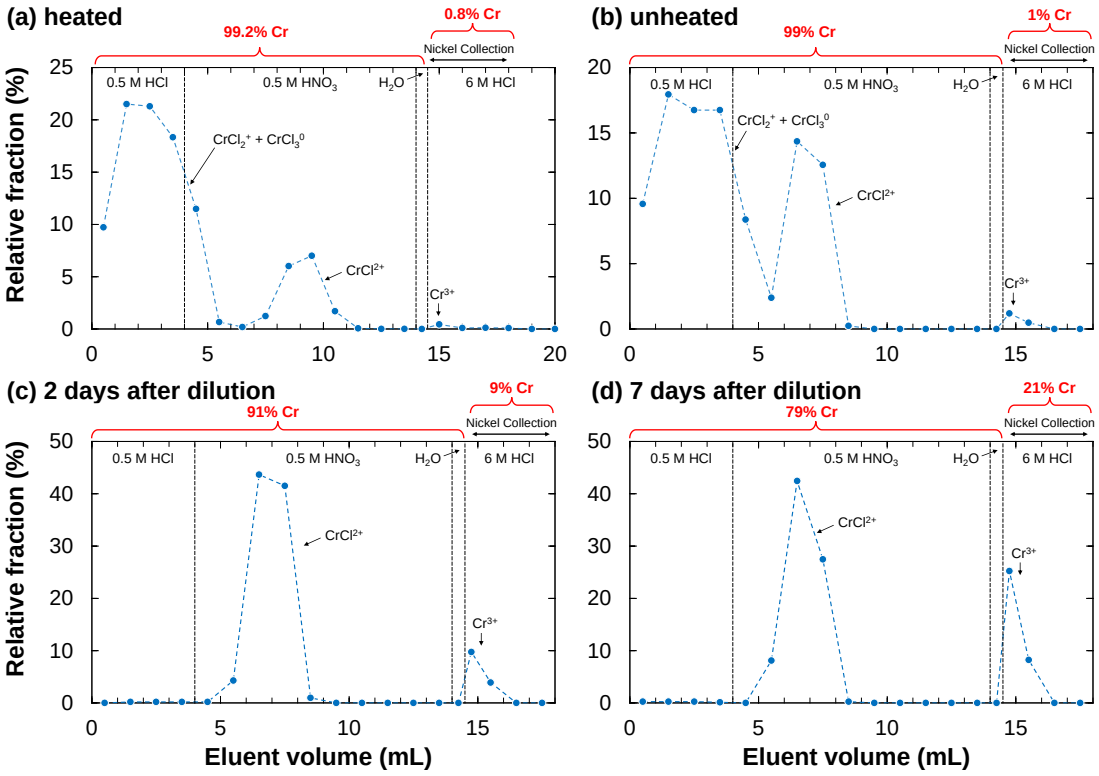

Figure 8. Elution behavior of Cr in the separation step 3.

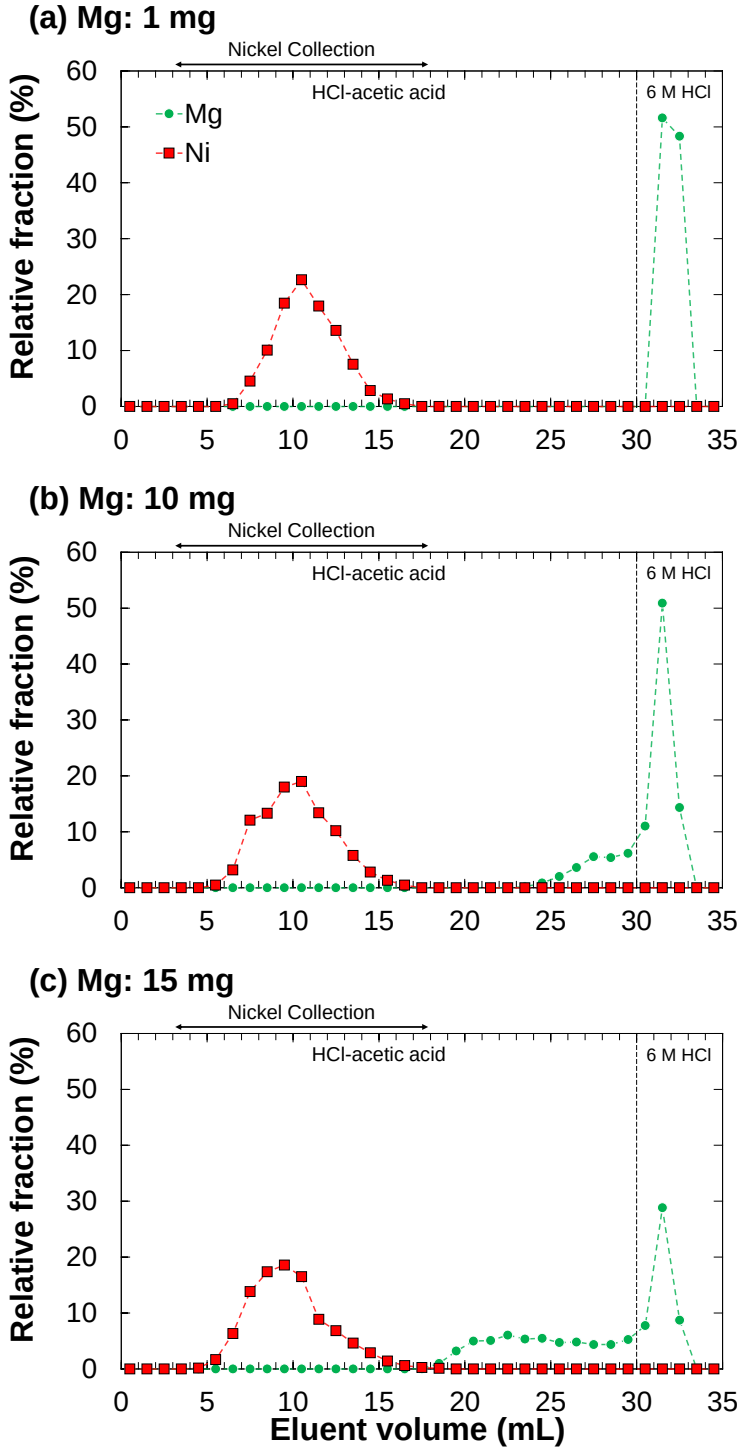

Figure 9. Elution behavior of Mg and Ni in the separation step 2 tested in Mg amount of (a) ~1 mg, (b) ~10 mg, and (c) ~15 mg.

2.4. Summary

Modifying the Ni separation methods by Spivak-Birndorf et al. (2018) and Render et al. (2018), an efficient and practical chemical separation method for applying ^{60}Fe–^{60}Ni chronology to Mg-enriched and Ni-depleted silicate samples (especially HED meteorites) is developed in this study. For obtaining sufficient amount of Ni from Ni-depleted samples, large amount of the samples should be used. This simply results in large amounts of matrix elements in the separation chemistry, which cause some technical issues. The most important matrix elements here are Cr and Mg. Chromium exists in HCl media as four different coordination states of $CrCl_3$, $CrCl_2^+$, $CrCl^{2+}$, and Cr^{3+}, and Cr^{3+} is difficult to separate from Nd by the original methods of Spivak-Birndorf et al. (2018) and Render et al. (2018) (Figure 7). This problem is resolved by adding the separation step 3 (Figure 8), which is modified after Larsen et al. (2016; 2018). For Mg, the capacity of cation-exchange resin is problematic in the separation step 2 of this study (Figure 5). To avoid this issue, the maximum amount of Mg that can be retained to the resin is identified (Figure 9). These two improvements made in this study expand the applicability of the DMG-free Ni separation method originally developed by Spivak-Birndorf et al. (2018) and Render et al. (2018) to Mg-enriched and Ni-depleted silicate samples.

3. Separation chemistry for Sm–Nd chronology

3.1. Introduction

^{146}Sm–^{142}Nd chronometry has been used as a powerful cosmochemical tool for dating early solar system materials since the first application by Notsu et al. (1973). This dating method is based on α decay of an extinct nuclide ^{146}Sm to ^{142}Nd with a half-life of 103 Ma (Friedman et al., 1966; Meissner et al., 1987); note that a recent measurement by Kinoshita et al. (2012) provided a shorter half-life of 68 Ma while the former value is widely accepted by researchers at present (e.g., Marks et al., 2014). Owing to its short half-life, ^{146}Sm–^{142}Nd decay system provides more precise chronological data relative to other decay systems that are commonly applied for terrestrial samples (e.g., ^{87}Rb–^{87}Sr, ^{147}Sm–^{143}Nd, and ^{176}Lu–^{176}Hf decay systems). As for HED meteorites, ^{146}Sm–^{142}Nd systematics of eucrites are investigated by previous studies (diogenites are not suitable to ^{146}Sm–^{142}Nd dating due to low Nd contents).

For the sufficient separation of Sm from other REEs (especially Ce and Sm) to perform highly accurate and precise isotope measurement, two types of chemical separation methods using Ln resin are calibrated in this study. The ^{146}Sm–^{142}Nd short-lived dating requires a Ce/Nd ratio of the separated sample lower than 10^{-5} to avoid an interference from ^{142}Ce onto ^{142}Nd (e.g., Boyet and Carlson, 2005; Boyet et al., 2010). The first Nd separation method uses fine-particle Ln resin and is based on Mizutani et al. (2020). Although Ce and Nd is difficult to resolve with course-particle Ln-resin, they found that fine-particle resin is capable to provide better separation for them. The second is a separation method using a strong oxidizing agent of potassium bromate ($KBrO_3$). In this method, Ce is oxidized to become tetravalent form other trivalent REEs including Nd. Here, these two separation methods are calibrated and modified to purify Nd from HED meteorite samples.

3.2. Experiments

3.2.1. Calibration of the separation method using fine-particle Ln resin

Firstly, the separation method using fine-particle Ln resin (Mizutani et al., 2020) is calibrated. This method is a simple combination of Ln resin (Eichrom Technologies, particle size 20–50 μm) and hydrochloric acid. Lanthanides loaded onto Ln resin can be eluted in the order of atomic number together with hydrochloric acid flow. This tendency reflects the fact that affinity of lanthanides to Ln resin differs slightly, depending on their ionic radii (e.g., Ireland et al., 2013) and concentration of hydrochloric acid. For the sake of sufficient separation of Nd from Ce and Sm, concentration and amount of hydrochloric acid are calibrated.

Judging from the results of calibration by Mizutani et al. (2020), Ce–Nd separation is much more difficult relative to Nd–Sm separation. Hence, a resolution of Ce–Nd separations is estimated prior to calibration experiments. A resolution between gaussian elution peaks of two elements in column chromatography can be expressed as

$$\mathrm{Res.}_{\mathrm{A\text{–}B}} = \frac{V_\mathrm{B} - V_\mathrm{A}}{2\sigma_\mathrm{B} + 2\sigma_\mathrm{A}}. \quad (1)$$

V is mean volume of gaussian elution peak, σ is standard deviation of gaussian elution peak, and A and B represents certain elements in interests. According to the plate theory in chromatography, this equation can be rewritten as

$$\mathrm{Res.}_{\mathrm{A\text{–}B}} = \frac{1}{4}\sqrt{N}\,\frac{k'_\mathrm{B}/k'_\mathrm{A} - 1}{k'_\mathrm{B}/k'_\mathrm{A}}\,\frac{k'_\mathrm{B}}{1 + k'_\mathrm{B}}. \quad (2)$$

N is number of theoretical plates and k' is capacity factor defined as

$$k' = k\frac{v_\mathrm{s}}{v_\mathrm{m}}, \quad (3)$$

where k is distribution coefficient of element between resin and eluent and v_s and v_m are volume of solid phase (i.e., resin) and mobile phase (i.e., eluent) in chromatographic column respectively. A requirement of chemical separation is Res. = 1 and larger value of Res. means better separation. Since the distribution coefficients of lanthanides between Ln resin and hydrochloric acid depend on concentrations of hydrochloric acid, the resolution in equation (2) can be drawn as a function of HCl concentrations in two-dimensional graph. The resolutions of $\mathrm{Res.}_{\mathrm{Ce\text{–}Nd}}$ and $\mathrm{Res.}_{\mathrm{Pr\text{–}Nd}}$ estimated from equation (2)

are shown in Figure 10. Although Pr dose not cause isobaric interferences in Nd isotope measurements, presence of Pr prevents an ionization of Nd in the ion source of mass spectrometer. Thus, a removal of Pr by chemical separation is favorable for Nd isotope measurements. Number of theoretical plates in equation (2) is assumed to be $N = 300$ based on the elution profile obtained by Mizutani et al. (2020), v_s/v_m is assumed to be 0.55 (Yokoyama et al., 2020), and distribution coefficients measured by Ireland et al. (2013) are adopted as value of k. Capacity factors (k') of Ce and Pr are also shown in Figure 10 together with the estimates for resolutions. Since the value k' is proportional to the volume of HCl required to elute the element from the resin, it is useful to estimate the required time of chemical separation. As shown in Figure 10, both resolution and k' show higher values at lower molarity of HCl. This means that the separations of Ce–Nd and Pr–Nd get better in lower molarity of HCl while the required time gets larger simultaneously. The requirement of chemical separation (Res. = 1) can be achieved at >0.5 M HCl for Ce–Nd. However, it is difficult to achieve $Res._{Pr–Nd} > 1$ at practical concentration of HCl. Based on the relationships among resolution, HCl concentration, and k' shown in Figure 10, two concentrations of 0.15 M and 0.17 M (shown as black solid lines) are chosen for calibration of Ce, Pr–Nd separation in this study. k' value of Pr at 0.15 M HCl ($k' \approx 30$) corresponds to ~24 hours of required time for the chemical separation treatment, which is upper limit of the required time to conduct the experiments repeatedly.

A column for chromatographic separation is prepared by packing the Ln resin into a thin quartz column (0.5 mL volume, 2.5 mm inner diameter, 100 mm length). Following the loading of a few drops of standard sample solution for calibration (0.15 M or 0.17 M HCl containing La, Ce, Pr, Nd, and Sm) onto the resin, 0.15 M or 0.17 M HCl is loaded to wash out La, Ce, and Pr. Nd is collected by 7 mL of 0.25 M HCl and REEs heavier than Sm are eluted by 5 mL of 6 M HCl.

3.2.2. Calibration of the separation method using $KBrO_3$

Secondly, the separation method using an oxidizing agent of $KBrO_3$ (Kagami and Yokoyama, 2016) is calibrated. This method consists of two steps of column chemistry; Step 1 is separation of Ce from other REEs, Step 2 is separation of Nd from La, Pr, and Sm, which is similar to the separation chemistry of Mizutani et al (2020). A column for

both the separation step 1 and 2 is prepared by packing medium-particle Ln resin (Eichrom Technologies, particle size 50–100 μm) into a thin quartz column (0.5 mL volume, 2.5 mm inner diameter, 100 mm length). A few drops of standard solution (10 M HNO_3 containing La, Ce, Pr, Nd, and Sm) are loaded onto the resin that is conditioned by 10 M HNO_3 + $KBrO_3$ (10 M HNO_3 containing ~20 mM of $KBrO_3$). REEs except for Ce are collected by 6 mL of 10 M HNO_3 + $KBrO_3$. Ce can be washed out by 2 mL of 10 M HNO_3, 2 mL H_2O, and 3 mL of 6 M HCl. The Ce-free REE fraction collected in the Step 1 is redissolved in a few drops of 0.15 M HCl and loaded onto the same resin. La and Pr are eluted by 0.15 M HCl and Nd is collected by 7 mL of 0.25 M HCl.

In addition to the calibration of the separation method of Kagami and Yokoyama (2016), a single step separation of Nd from La, Ce, Pr, and Sm is also tested in this study. A few drops of standard solution (0.15 M HNO_3 containing La, Ce, Pr, Nd, and Sm) are loaded onto the resin that is preconditioned by 0.15 M HNO_3 + $KBrO_3$ (0.15 M HNO_3 containing ~20 mM of $KBrO_3$). La, Pr, and Nd elutes successively with 0.15 M HNO_3 + $KBrO_3$ while the resin retains Ce.

All the solutions eluted from the column in the calibration experiments are collected in 1 mL interval and measured by ICP-QMS (Agilent 7700x) at Nagoya University to obtain abundances of REEs. These data are used to draw elution curves of elements and to judge whether a quality of the separation is sufficient for ^{146}Sm–^{142}Nd isotope measurements.

Table 3. Cup configuration for Nd isotope measurement by TIMS in static mode.

Cup	L4	L3	L2	L1	C	H1	H2	H3	H4
Mass	140	142	143	144	145	146	148	150	152
Element	Ce	Ce+Nd	Nd	Nd+Sm	Nd	Nd	Nd	Nd	Sm

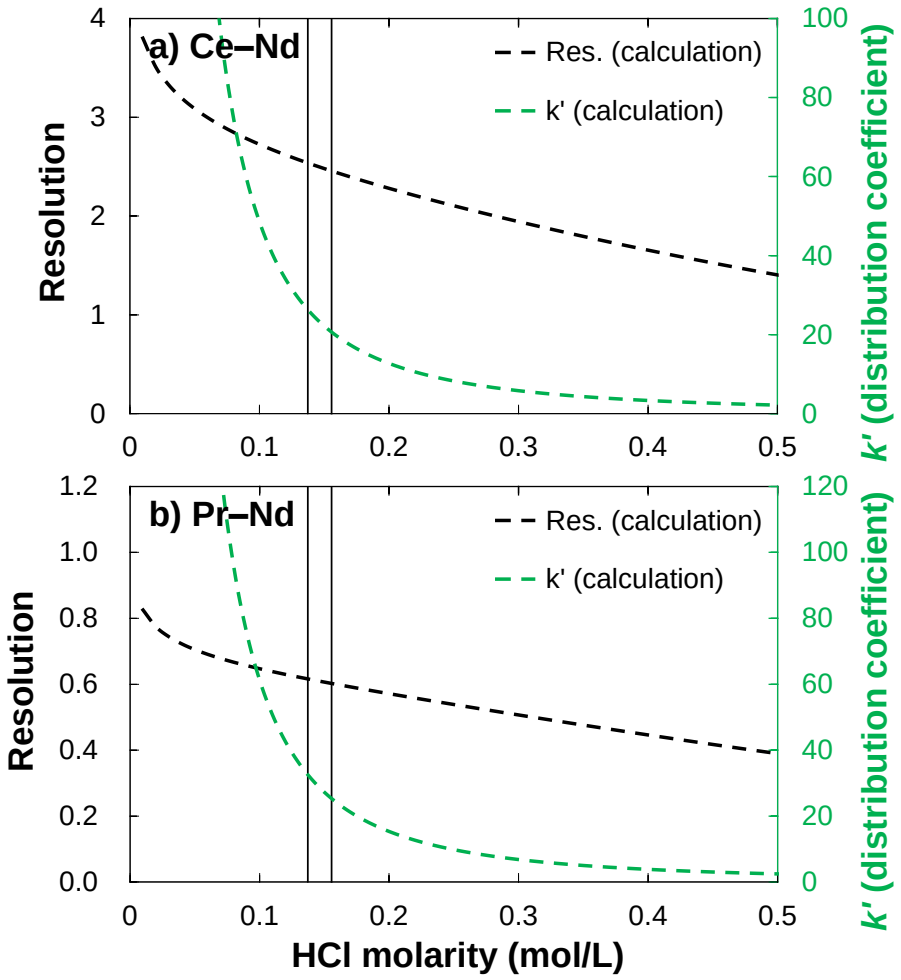

Figure 10. Estimated resolution for (a) Ce–Nd and (b) Pr–Nd separation. The black dashed line represents resolution calculated by equation (2). The green dashed line represents capacity factor calculated by equation (3), which is proportional to mean volume of gaussian elution peak of Ce and Pr respectively (data from Ireland et al., 2013). Two black solid lines correspond to molarities of 0.15 M and 0.17 M, which are the concentrations chosen for calibration in this study.

3.3. Results and discussion

3.3.1. Calibration results for the separation method using fine-particle Ln resin

Elution curves for the separation method using fine-particle Ln resin measured in this study are shown in Figure 11 and Figure 12. As shown in these two figures, both 0.15 M and 0.17 M HCl appear to successfully separate La, Ce, and Sm from Nd, whereas Pr is obviously difficult to separate from Nd. To assess a quality of the separation quantitatively, parameters that characterize elution curves of each element shown in Figure 11and Figure 12 are listed in Table 4. With respect to the values of Res., gaussian fitting curves for the elution data of La and Ce can be separated from those of Nd (Res. > 1) in both 0.15 M and 0.17 M HCl, whereas those of Pr and Nd are difficult to separate (Res. < 1). However, considering the recovery yields in the Nd fractions, there are problems of the separation not only for Pr but also for La and Ce. Although elution curves of La and Ce are apparently separated from those of Nd (Figure 11 and Figure 12), they show considerably high recovery yields in the Nd fraction (La = 7.0% and Ce = 12.0 % for 0.17M HCl, La = 2.1% and Ce = 3.8% for 0.15 M HCl; Table 4). This may be caused by the tailing effect, which is a well-known phenomenon in column chromatography (e.g., Giddings, 1963). As shown in the elution curves in log-scale (Figure 11 and Figure 12), right shoulders of the elution curves do not follow the gaussian distributions and their declination are extremely gradual. While quantities of the tailing elements included in individual 1-mL fractions are lower than 1%, their summations can reach >1% of the recovery yields of La and Ce in the Nd fractions, which are problematic for accurate and precise isotope measurements of Nd; note that the requirement is Ce/Nd < 10^{-5}. Because the tailing effects are ubiquitous in chromatographic processes and are difficult to avoid, the Nd separation method using fine-particle Ln resin is not appropriate for ^{146}Sm–^{142}Nd dating. It should be noted that Mizutani et al. (2020), who proposed the original of the separation method of this study, did not mention about the significant tailing of La and Ce in their text and elution curves. It is unclear whether they missed this tailing effect or successfully controlled that. However, since their main concern was isotope measurements of Dy, Er, and Yb, it is not unlikely that they overlooked the tailing of La and Ce, which do not interfere the isotope measurements of these three elements.

Changing the molarity of HCl is one of the possible approaches to improve the Pr–Nd separation. Comparisons between the estimated resolutions for the Ce–Nd and Pr–Nd separations shown in Figure 10 and the experimental results in this study are presented in Figure 13. Although the calculations overestimate the resolutions of Ce–Nd and underestimate that of Pr–Nd, relations between the resolution and the HCl molarity are qualitatively consistent between the experiments and the estimations as shown in the figure. Considering the estimation for the Pr–Nd separation and experimental results of this study shown in Figure 13(b), HCl whose concentration is lower than ~0.05 mol/L may achieve the resolution value higher than 1.0. However, it should be noted that the resolution increases linearly along with decrease of HCl molarity in the range of the molarity higher than ~0.05 mol/L whereas *k'* increases exponentially (Figure 13(b)). Since *k'* value is proportional to the peak volume of elution curve, the separation experiment using ~0.05 M HCl should require considerably long time that is absolutely impractical for a routine experiment. Furthermore, the problem of peak-tailing still remains if >0.05 M HCl are used. Thus, changing HCl the molarity is not efficient for improving the Pr–Nd separation.

Another possible way for improving the Pr–Nd separation is changing experimental equipment. In general, extension of length of chromatographic column is helpful to increase resolution of separation. Resolutions of the Pr–Nd separation improved by this approach is estimated by simple calculation. Using the experimental data in this study and equation (2), $\mathrm{Res.}_{\mathrm{Pr–Nd}}$ values were estimated for extended length of chromatographic column (Figure 14). The experiments in this study corresponds $N \approx 270$ and $\mathrm{Res.}_{\mathrm{Ce–Nd}} \approx 0.9$. For achieving $\mathrm{Res.}_{\mathrm{Ce–Nd}} = 1$, $N > 300$ is required. For $\mathrm{Res.}_{\mathrm{Ce–Nd}} = 2$, $N > 1400$ is required. Assuming N is proportional to the length of the chromatographic column, the column with >500 mm length, which is five times longer than the column regularly used, is required for the Res. = 2. Such a long column is not commercially available and is difficult to put into the clen experimental space in the laboratory. Furthermore, the tailing problem may be more severe in the longer column. Thus, extension of chromatographic column is not efficient for improving the Pr–Nd separation.

3.3.2. Calibration results for the separation method using $KBrO_3$

Elution curves for the separation method using $KBrO_3$ with concentrated and diluted HNO_3 are shown in Figure 15 and Figure 16, respectively. As mentioned in the section 3.2.2. Calibration of the separation method using $KBrO_3$, the method using concentrated HNO_3 (Figure 15) is almost the same as Kagami and Yokoyama (2016). The method using diluted HNO_3 (Figure 16) is based on a combination of the concepts of the two separation methods that the Ce removal using $KBrO_3$ (e.g., Kagami and Yokoyama, 2016) and the mutual separation of REEs using the fine-particle Ln resin (e.g., Mizutani et al., 2020). For the determination of the concentration of HNO_3 to use in the mutual separation, the same calculation approach as the HCl methods (e.g., Figure 10) is adopted. Figure 17 shows the estimated resolutions for the La–Nd and Pr–Nd separations calculated by this approach. Owing to the oxidation reaction of Ce^{3+} to Ce^{4+} caused by $KBrO_3$, the Ce–Nd separation does not have to be cared about in this separation method. This is the reason why the medium-particle Ln resin, which should show worse resolution quality relative to the fine-particle one, is chosen for this method. In general, a coarser-particle resin provides a faster elution speed in exchange for the resolution. Hence, if the separation quality is enough for the isotope measurement, a coarser-particle resin is obviously favorable for routine experiments.

As shown in Figure 15, the separation method using $KBrO_3$ with concentrated HNO_3 can remove Ce successfully from the other REEs. Though medium to heavy REEs are not shown in the figure, they are also collected by HNO_3 + $KBrO_3$ together with La, Pr, Nd, and Sm because of high molarity of HNO_3. Hence, this fraction can be applied for further isotopic studies for REEs other than the Sm–Nd dating. The recovery yield of Ce in the Nd fraction is less than 0.01% of the total amount of Ce (Table 5), which is enough to achieve the requirement for ^{146}Sm–^{142}Nd isotope measurement of Ce/Nd < 10^{-5}. The high-level elimination of Ce is a clear advantage of this method compared with the method using fine-particle Ln resin described above. Interestingly, Ce has two distinct gaussian elution peaks around ~8 mL and ~11 mL, respectively (see the log-scale elution curve in Figure 15). The minor peak around ~8 mL probably corresponds Ce^{3+} that are reduced mildly by $KBrO_3$-free HNO_3. The major peak around ~11 mL consists of Ce^{3+} that are reduced efficiently by a reducing agent of HCl + H_2O_2. Though the Ce removal

was successful in this method, a separation protocol to purify Nd from other REEs is required. For this additional separation, the separation method using fine-particle resin described above is useful (Figure 12). Here, the medium-particle Ln resin is adopted instead of the fine-particle one because the medium-particle one provides sufficient resolution for the separation of Nd from REEs other than Ce and show faster elution rate relative to the fine-particle one. As shown in Figure 18, this separation method successfully removes La and Sm from Nd. The recovery yields of La in the Nd fraction is 0.08% (Table 6). Interestingly, this recovery yield is obviously better than that of the separation method using fine-particle resin (4.91%; Table 4b), despite better La–Nd resolution in the fine-particle resin (4.91 in fine-particle and 3.89 in medium particle; Table 4 and Table 6). This difference reflects weaker tailing effect of La in the medium-particle Ln resin (<0.1%-level; Figure 18) relative to that in the fine-particle one (>0.1%-level; Figure 12). Although a clear cause of a difference of magnitudes of the tailings is difficult to identify, one possibility is an elution rate. The elution rate in the fine-particle resin is extremely slow (e.g., Ireland et al., 2013; Mizutani et al., 2020; Yokoyama et al., 2020); for instance, <0.01 mL min^{-1} in the experimental setup of this study. In such a slow flow of eluent, vertical diffusion of REE cations in the chromatographic column may show significant effect. Assuming eluent/resin ratio in the column to be 1:1, it takes ~25 min for a drop of eluent passing through the top from bottom of the 0.5-mL column (0.5 mL × 0.5 ÷ 0.01 mL min^{-1}). Adopting a diffusion coefficient of Sm^{3+} in water (5.05 × 10^{-10} m^2 s^{-1}; Sato et al., 1996) as a representative value for trivalent REE cations, a diffusion length of REE cations during ~25 min is calculated to be ~1.2 mm using the relation of $d = (2Dt)^{1/2}$, which corresponds ~1% of the column length (~100 mm) used in this study. For the elution peak volume of La (4.50 mL; Table 4b), the diffusion length is ~5.2 mm, corresponding ~5% of the column length. Though it is difficult to judge whether the diffusion is responsible for the whole tailing effects observed in the fine-particle resin (Figure 11 and Figure 12), the vertical diffusion of cations is probably one of the causes of the tailing effects. The removal of 90% of Ce (i.e., 10% of Ce recovery yield in the Nd fraction; Table 6) in the separation method using medium particle-resin is also helpful for the elimination of Ce.

As shown in Figure 16, the separation method using $KBrO_3$ with diluted HNO_3 can remove Ce and most of other REEs from Nd through a single-step column chemistry.

Only two exceptions are La and Pr. For Pr, elution peaks of this element and Nd overlap obviously that is recognized even in the linear-scale elution curve (Figure 16). For La, significant overlap of a tailing of La and elution peak of Nd can be confirmed in the log-scale elution curve (Figure 16), though this overlap is not recognizable in the linear-scale. The recovery yields in the Nd fraction are 1.8% for La and 95.5% for Pr, respectively (Table 5). However, remaining La and Pr do not cause critical problem for Nd isotope measurement because these two elements do not have any isobars of Nd isotopes. These elements only prevent efficient ionization of Nd at the isotope measurement by TIMS. Although it is invisible in the linear-scale elution curve, Ce show a small elution peak around ~13 mL in the log-scale elution curve, probably due to low oxidation ability of diluted HNO_3. This results in slightly higher Ce recovery in the Nd fraction (0.08; Table 5b) relative to that of the method using concentrated HNO_3 (<0.01; Table 5a). Since the Ce removal is the most essential requirement for the ^{146}Sm–^{142}Nd dating, the method using concentrated HNO_3 (Figure 15) is adopted as a Nd separation method in this study. It should be noted that though the method using diluted HNO_3 can separate Nd from other REEs in single step chemistry, it requires additional separation step for removing K that derived from $KBrO_3$. Hence, there are no significant difference between convenience of the method using diluted and concentrated HNO_3.

Table 4. Parameters characterizing elution curves in Figure 11 and Figure 12.

(a) Parameters for Figure 11 (i.e., fine-particle resin with 0.17 M HCl).

	La	Ce	Pr	Nd
V^a (mL)	3.66	9.04	12.63	15.33
σ^a (mL)	0.53	0.82	0.91	0.74
N^b	48	120	190	430
k'	11.2	29.1	41.1	50.1
Res. with Nd[c]	4.60	2.01	0.82	—
Recovery yield in Nd fraction (%)	7.0	12.0	78.4	91.6

(b) Parameters for Figure 12 (i.e., fine-particle resin with 0.15 M HCl).

	La	Ce	Pr	Nd
V^a (mL)	4.50	11.15	15.83	19.45
σ^a (mL)	0.43	0.72	0.96	1.10
N^b	110	240	270	320
k'	14.0	36.2	51.8	63.8
Res. with Nd[c]	4.91	2.29	0.88	—
Recovery yield in Nd fraction (%)	2.1	3.8	45.6	98.5

[a]Gaussian fitting parameters. V corresponds an average and σ corresponds a standard deviation of the distribution.
[b]N is an equivalent number of theoretical plates calculated from individual gaussian fitting curves.
[c]Res. between each element and Nd is calculated using V, σ, and equation (2).

Table 5. Parameters characterizing elution curves in Figure 15 and Figure 16.

(a) Parameters for Figure 15 (i.e., $KBrO_3$ with concentrated HNO_3).

	La	Ce	Pr	Nd
V^a (mL)	0.37	10.75	0.39	0.40
σ^a (mL)	0.21	0.20	0.23	0.23
N^b	—	—	—	—
k'	0.2	—	0.3	0.4
Res. with Nd[c]	0.04	11.86	0.02	—
Recovery yield in Nd fraction (%)	100.0	<0.01	100.0	100.0

(b) Parameters for Figure 16 (i.e., $KBrO_3$ with diluted HNO_3).

	La	Ce	Pr	Nd
V^a (mL)	4.14	23.02	12.69	17.51
σ^a (mL)	0.37	0.59	1.09	1.31
N^b	130	—	140	120
k'	12.8	—	41.3	47.6
Res. with Nd[c]	3.11	2.22	0.39	—
Recovery yield in Nd fraction (%)	1.8	0.08	95.5	91.5

*Detailed descriptions for the parameters shown here are the same as Table 4.

Table 6. Parameters characterizing elution curves in Figure 18.

	La	Ce	Pr	Nd
V^a (mL)	5.47	13.56	22.66	30.50
σ^a (mL)	0.51	1.07	1.41	1.69
N^b	110	160	180	180
k'	17.2	44.2	62.0	74.5
Res. with Nd[c]	3.89	1.65	0.61	—
Recovery yield in Nd fraction (%)	0.08	10.5	99.7	99.9

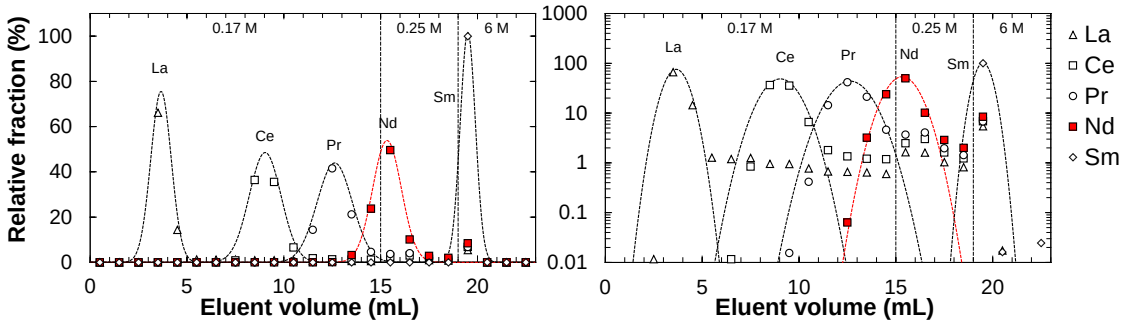

Figure 11. Elution profile for the separation method using fine-particle (20–50 μm) Ln resin with 0.17 M HCl. Horizontal axis shows cumulative volume of eluents loaded onto column, and vertical axis shows relative fraction of elements measured in this study. Symbols shows analytical data, and dashed lines are least-square gaussian fitting curves of them. The left is linear-scale, and the right is log-scale.

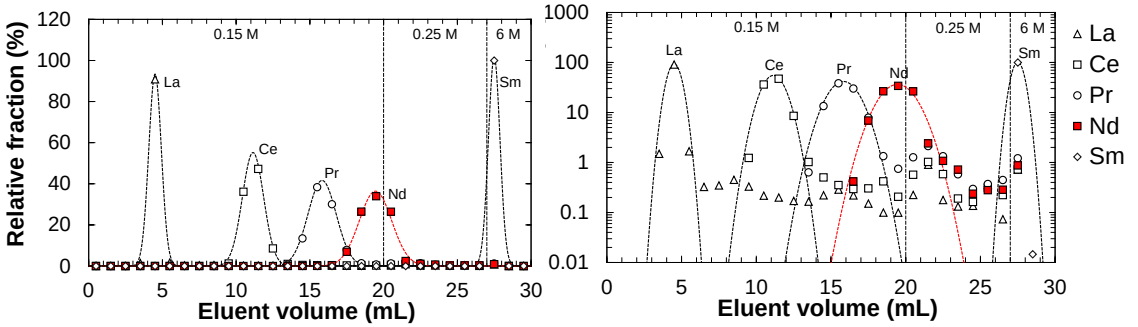

Figure 12. Elution profile for the separation method using fine-particle (20–50 μm) Ln resin with 0.15 M HCl. Legend is the same as Figure 11.

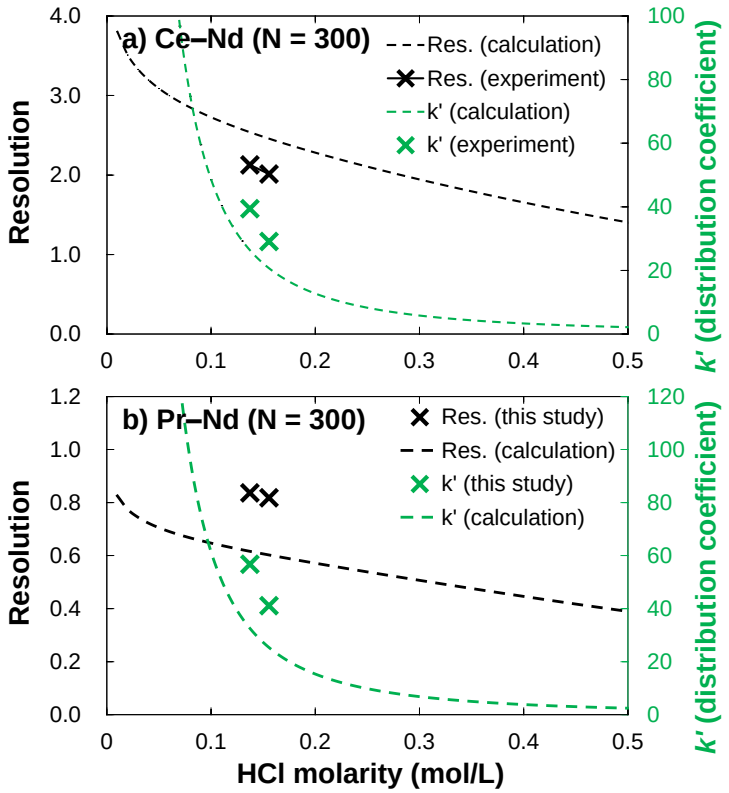

Figure 13. Comparisons between the estimated resolutions for (a) Ce–Nd and (b) Pr–Nd separations using HCl as eluent and the experimental results of this study. Green and black dashed lines show estimations for *k'* and resolution, respectively. Green and black crosses show experimentally obtained values of *k'* and resolution, respectively.

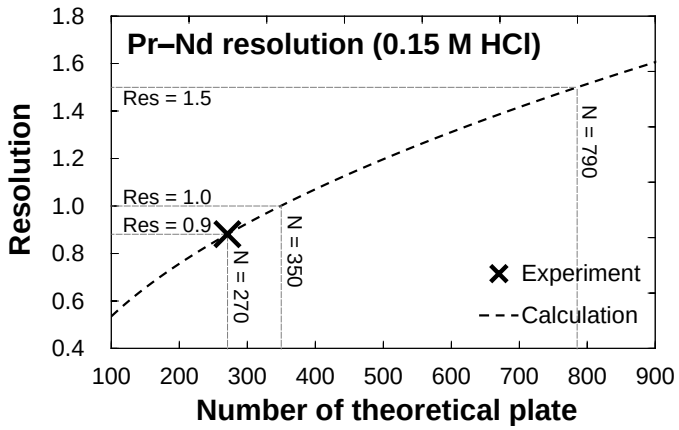

Figure 14. Estimated resolution of Pr–Nd separation. On the basis of the value of $Res._{Ce–Nd}$ of 0.15 M HCl in this study, $Res._{Ce–Nd}$ at different length of the column (i.e., number of theoretical plate) are estimated.

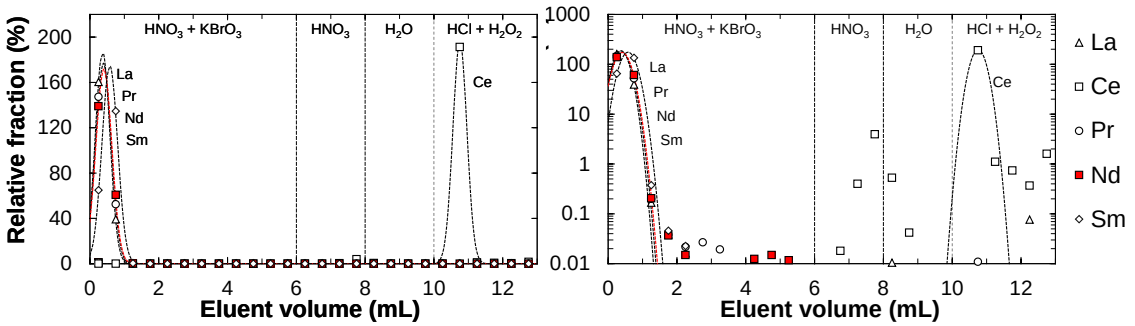

Figure 15. Elution profile for the separation method using $KBrO_3$ with concentrated HNO_3. Legend is the same as Figure 11. The medium-particle (50–100 μm) Ln resin is used for this experiment.

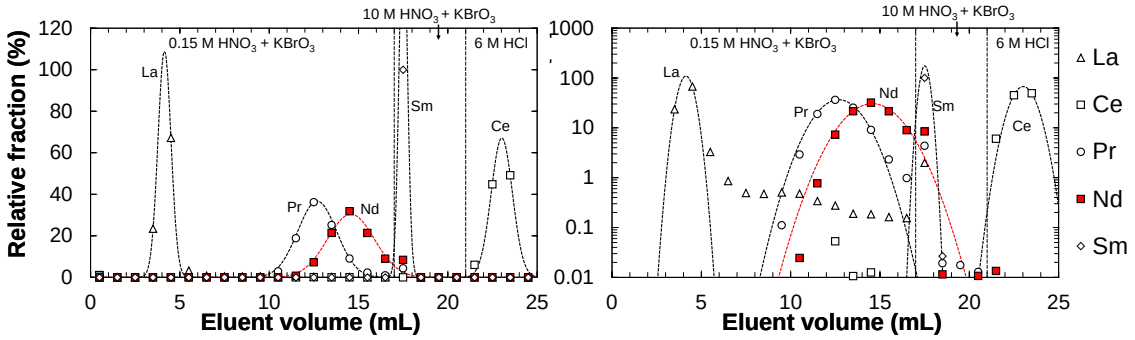

Figure 16. Elution profile for the separation method using $KBrO_3$ with diluted HNO_3. Legend is the same as Figure 11. The medium-particle (50–100 μm) Ln resin is used for this experiment.

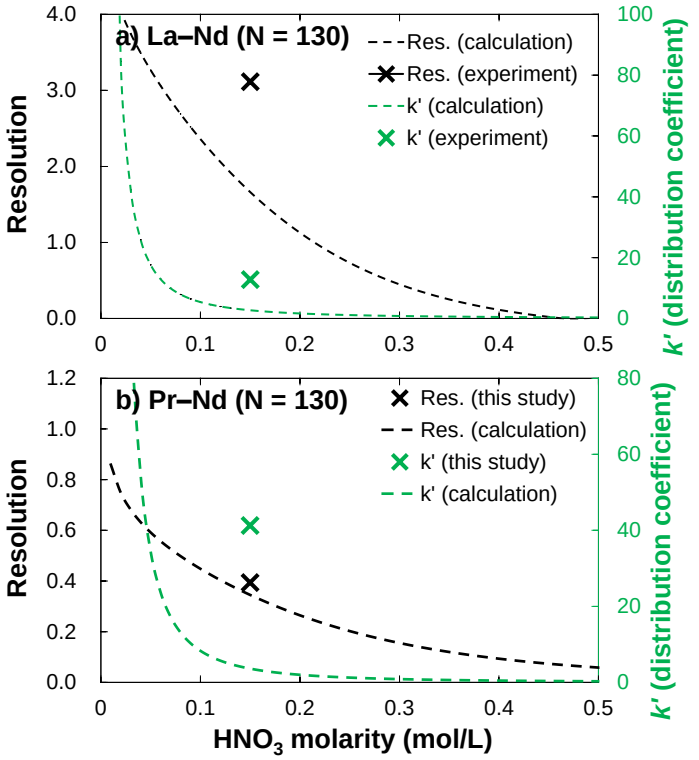

Figure 17. Comparisons between the estimated resolutions for (a) La–Nd and (b) Pr–Nd separations using HNO_3 as eluent and the experimental results of this study. Green and black dashed lines show estimations for *k'* and resolution, respectively. Green and black crosses show experimentally obtained values of *k'* and resolution, respectively. $N = 130$ corresponds medium-particle (50–100 μm) Ln resin that is used for the separation method using $KBrO_3$.

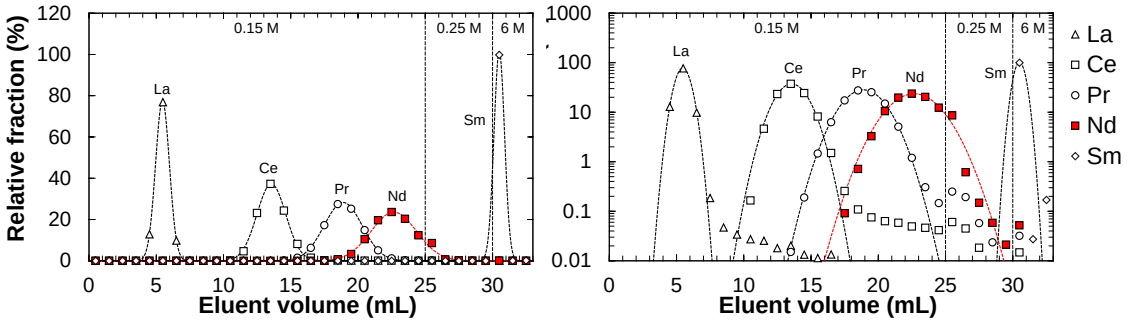

Figure 18. Elution profile for the separation method using medium-particle (50–100 μm) Ln resin with 0.15 M HCl, which is an additional La–Pr separation protocol for the separation method using concentrated HNO_3 + $KBrO_3$. Legend is the same as Figure 11.

3.4. Summary

For adopting the ^{146}Sm–^{142}Nd short-lived chronometry to HED meteorites, two different concepts for chemical purification of Nd are calibrated and compared in this study. The Nd separation method using fine-particle Ln-resin (Mizutani et al., 2020) cannot separate Ce from Nd successfully, probably due to significant tailing effect of Ce in the column chromatographic separation. The amount of the remaining Ce in the Nd fraction is problematic for accurate ^{146}Sm–^{142}Nd dating because of the isobaric interference form ^{142}Ce onto ^{142}Nd. In contrast, the Nd separation method using $KBrO_3$ (Kagami and Yokoyama, 2016) can remove Ce from Nd successfully owing to the efficient oxidation of Ce^{3+} to Ce^{4+}. This method can be applied to HED meteorite samples to obtain accurate and precise ^{146}Sm–^{142}Nd isotopic data.

4. Rb–Sr and Lu–Hf chronology of diogenites

4.1. Introduction

As discussed in chapter 1. Research background, chronological data is one of key factors that strongly constrain differentiation processes of Vesta. Here, ^{176}Lu–^{176}Hf systematics (λ^{176}Lu = 1.867 × 10^{-11}; Söderlund et al., 2004) of nine diogenites are firstly investigated to determine the crystallization ages of diogenites and to reveal the chronological relationship between eucrites and diogenites. Although ^{176}Lu–^{176}Hf systematics of eucrites were investigated systematically by Blichert-Toft et al. (2002) and Bouvier et al. (2015), that of diogenites have not yet been investigated. Hence, new ^{176}Lu–^{176}Hf isotope data of diogenites will allow detailed comparisons between formation ages of eucrites and diogenites. Furthermore, because of its high closure temperature (e.g., Scherer et al., 2000; Anczkiewicz et al., 2007) due to low diffusivities of Lu and Hf (e.g., Bloch et al., 2017), ^{176}Lu–^{176}Hf systematics is not largely affected by impact disturbance. This is helpful for determining accurate crystallization ages of diogenites.

In addition to ^{176}Lu–^{176}Hf systematics, ^{87}Rb–^{87}Sr systematics (λ^{87}Rb = 1.42 × 10^{-11}; Steiger and Jäger, 1977) of nine diogenites are also investigated in this study. Although Takahashi and Masuda (1990) provided statistically meaningful ^{87}Rb–^{87}Sr isochron ages of two diogenites, other two studies reported disturbances of ^{87}Rb–^{87}Sr systematics of diogenites within subsamples of single diogenites (Birck and Allègre, 1981) and among three different diogenite samples (Nakamura, 1979). ^{87}Rb–^{87}Sr systematics possibly records temporal information of different events from ^{176}Lu–^{176}Hf systematics because of the relatively weak refractoriness of ^{87}Rb–^{87}Sr systematics against thermal disturbances (e.g., Harrison et al., 1979). Therefore, a combination of ^{87}Rb–^{87}Sr and ^{176}Lu–^{176}Hf systematics may provide detailed thermal history of HED meteorites.

For investigating the differentiation processes of igneous rocks, rare earth element (REE) abundance pattern is a powerful and well-established geochemical tool (e.g., Masuda and Matsui, 1966). Although REE abundances of diogenites are investigated in several previous studies (e.g., Barrat et al., 2008; Barrat et al., 2010; Mittlefehldt et al., 2012), a combination of REE abundance pattern and chronological information from ^{87}Rb–^{87}Sr and ^{176}Lu–^{176}Hf systematics will allow a construction of more detailed

differentiation model of diogenites than those in previous studies. In this study, based on the new ^{87}Rb–^{87}Sr and ^{176}Lu–^{176}Hf isotopic data sets and REE abundances of nine diogenites, the differentiation processes of HED meteorites are discussed.

4.2. Experiments

Three fall diogenites (Bilanga, Johnstown, and Tatahouine), three desert-find diogenites (Hamara, LMT 042, and NWA 5480, where Hamara and LMT 042 are provisional names), and three Antarctic diogenites (Y 74013, Y 74097, and Y 002875) were used in this study for investigating their ^{87}Rb–^{87}Sr and ^{176}Lu–^{176}Hf systematics and REE abundances. Details of these diogenite samples are described in Table 7. The nine samples include brecciated, unbrecciated, ordinary, and olivine-bearing diogenites.

4.2.1. Sample digestion

In this study, each diogenite sample was analyzed after the division into three fractions of whole-rock, acid-residue, and acid-leachate. Since meteorites, especially desert-finds, often suffer both chemical and isotopic alterations during terrestrial residence (e.g., Nishikawa et al., 1990; Crozaz et al., 2003; Bland et al., 2006), the removal of terrestrial contaminants from meteorite samples is a key to obtain correct geological records of their parent bodies. Furthermore, the presence of Ca-phosphates in diogenites also causes two significant problems. First, since Ca-phosphate is a major host phase of incompatible elements despite being an accessory mineral in diogenites, an abundance of Ca-phosphates strongly controls whole-rock trace element compositions of diogenites. Therefore, whole-rock trace element data of diogenites generally reflects not only variations of parental melt compositions but also variations of Ca-phosphate contents (e.g., Barrat et al. 2008; 2010), which is problematic for modeling the differentiation processes of digenites. Second, isotope systems in Ca-phosphate are easily disturbed relative to those in pyroxene due to its low melting point (Yamaguchi et al., 2013). In fact, a significantly younger apatite U–Pb age relative to a whole rock age was reported for the Béréba eucrite (Zhou et al., 2011). Presence of such a young Ca-phosphate may disturb isotope systems in whole-rock diogenites. For the removal of these phases (i.e., terrestrial contaminants and Ca-phosphates) from the diogenite samples, an HCl-leaching treatment adjusted to complete digestion of Ca-phosphates was applied in this study.

For the HCl-leaching experiment, ~1 g of each sample fragment was used in this study. After an ultrasonic acetone wash to remove the terrestrial organic contaminants

from the sample fragment, the fragment was powdered using an agate mortar and pestle. The powder was leached using 5 mL of hot (100°C) 0.5 M HCl for 24 hours. After the collection of the acid-leachate fraction, the acid-residue fraction was completely digested by concentrated HF–$HClO_4$ mixture. These two sample fractions obtained in these procedures in this study were defined as "leachate" and "residue" respectively. Dry weights of these two fractions are shown in Table 8. The two olivine diogenites (LMT 042 and NWA 5480) display considerably high dry weights of leachate fractions relative to those of the seven ordinary diogenites due to weak acid-resistance of olivine (Table 8).

For the whole-rock analysis, ~200–800 mg of each sample fragment was used in this study. After the ultrasonic acetone wash and the powdering using an agate mortar and pestle, the sample powder was completely digested by the HF–$HClO_4$. This sample fraction was defined as "WR" in this study. Note that the sample fragments used for the whole-rock analysis and HCl-leaching experiment were obtained from different parts of the original meteorite samples. Finally, the three sample fractions (i.e., WR, residue, and leachate) were evaporated to dryness once and redissolved in ~5 mL of 3 M HCl ("mother solution"). A major portion (~90%) of the mother solution was used for the separation chemistry. The minor portion (~10%) was taken up with ~5 mL of 2% HNO_3 for the determination of trace element abundances by an inductively coupled plasma mass spectrometry (ICP-MS).

4.2.2. Separation chemistry

Prior to handling the meteorite samples, the Hf separation procedure following Yang et al. (2010) was calibrated. A mixture of standard solutions of Rb, Sr, REE, and Hf was loaded on an Ln-Spec resin (produced from Eichrom Technologies Corp., particle size of 100–150 μm) packed in 2 mL (~0.8 cm inner diameter and ~4 cm length) polypropylene column (produced by Eichrom Technologies Corp.) to confirm the elution behaviors of Sr, Nd, and Hf. Contents of several elements in eluted fractions were semi-quantitatively measured by an Agilent 7700x ICP-MS at Nagoya University. The result of the calibration is shown in Figure 19. Rubidium, Sr, Nd, and Sm were efficiently eluted by 3 M HCl with other matrix elements. Hafnium was successfully separated from interfering elements of Yb and Lu (^{176}Yb and ^{176}Lu on ^{176}Hf). Titanium, causing significant shifts of Hf isotope ratios in multi-collector ICP-MS (MC-ICP-MS) measurements (Münker et al., 2001), was

also cut off from the Hf fraction. Although this separation method purified Hf properly as described by Yang et al. (2010), an occurrence of flow-preventing bubbles from 4 M HCl–0.5% H_2O_2 was found to be a significant problem of this method, which had been pointed out by Bast et al. (2015) yet. For reducing the occurrence of the bubbles, the HCl–H_2O_2 was freshly prepared and kept at the low temperature environment (~5°C) just before its use.

Combining the result of the calibration (Figure 19) and well-confirmed Sr separation method used in Sakuma et al. (2018), purifications of Hf and Sr were achieved through a two-step resin chemistry (Table 9). In the first step of the resin chemistry to purify Hf, 5 mL of the mother solution of the sample (3 M HCl) was loaded on the Ln-spec resin (i.e., column I in Table 9), following the washing and conditioning by 60 mL of 6 M HCl–0.2 M HF and 21 mL of 3 M HCl. A matrix fraction containing Sr was collected with additional 10 mL of 3M HCl for the next separation chemistry. Interfering elements of Yb, Lu, and Ti were eluted from the resin with 15 mL of 4 M HCl, 20 mL of 6 M HCl, and 20 mL of 4 M HCl–0.5% H_2O_2 successively. Note that the volume of 4 M HCl–0.5% H_2O_2 depends on the Ti contents in the sample solution (see Yang et al., 2010). Finally, Hf was collected with 5 mL of 2 M HF. The Hf fraction was evaporated once and redissolved in 2% HNO_3 for the isotope measurement by MC-ICP-MS.

In the second step of the resin chemistry to purify Sr, an Sr-spec resin (produced from Eichrom Technologies Corp., particle size of 100–150 μm) packed in 0.5 mL (about 0.2 cm i.d. and 4 cm length) glass column (i.e., column II in Table 9) was used. After the washing and conditioning by 20 mL of H_2O and 2.5 mL of 3 M HNO_3, the matrix fraction collected in the first step of the resin chemistry, which was evaporated once and redissolved in 0.5 mL of 3 M HNO_3, was loaded on the Sr-spec resin. Matrix elements were eluted with additional 2.5 mL of 3 M HNO_3, and Sr was collected by 3 mL of hot (~50°C) H_2O. Organic compounds that present in the Sr fraction were decomposed by aqua regia for avoiding some technical problems at the Sr isotope measurement by TIMS.

4.2.3. Mass spectrometry

Hafnium isotope analysis of the nine diogenites was performed using a Thermo Scientific Neptune Plus MC-ICP-MS at Korea Institute of Geoscience and Mineral Resources. Eight Faraday cups were used to monitor the ion-beam intensities of $^{172}Yb^{+}$,

$^{174}Hf^+$, $^{175}Lu^+$, $^{176}Hf^+$, $^{177}Hf^+$, $^{178}Hf^+$, $^{179}Hf^+$, and $^{180}Hf^+$ with the static mode (Table 10). In the low mass-resolution mode of the MC-ICP-MS, 200 ppb Hf standard solutions yielded ion-beam intensities of ~3 × 10^{-11} A for $^{177}Hf^+$. Isobaric interferences from ^{176}Yb and ^{176}Lu on ^{176}Hf were corrected by $^{172}Yb/^{177}Hf$ and $^{175}Lu/^{177}Hf$ ratios assuming $^{176}Yb/^{172}Yb$ = 0.6125 and $^{176}Lu/^{175}Lu$ = 0.02668, while the interferences from ^{180}Ta and ^{180}W on ^{180}Hf could not be corrected due to a limitation of the number of Faraday cups. The exponential law (Russell et al., 1978) and the normalization value of $^{179}Hf/^{177}Hf$ = 0.7325 (Patchett and Tatsumoto, 1980) were used for instrumental mass bias corrections. The Hf fraction collected from the column I (Table 9) was introduced into the MC-ICP-MS through a wet sample introduction system. Each sample measurement comprised 128 integrations of the isotope ratios.

Strontium isotope analysis of the nine diogenites was performed using a VG Sector 54-30 TIMS at Nagoya University. Five Faraday cups were used to monitor the ion-beam intensities of $^{84}Sr^+$, $^{85}Rb^+$, $^{86}Sr^+$, $^{87}Sr^+$, and $^{88}Sr^+$ with the dynamic mode (Table 11). The Sr fraction collected from the column II (Table 9) was loaded on a Re filament with a Ta_2O_5 activator to stabilize an ionization behavior of Sr. Heating currents of 3–4 A were applied to the filaments and 200 ng of Sr standard samples yielded ~2 × 10^{-11} A of $^{88}Sr^+$ ion currents. Isobaric interferences from ^{87}Rb on ^{87}Sr were corrected by $^{85}Rb/^{87}Sr$ ratios, assuming $^{87}Rb/^{85}Rb$ = 0.3559. The exponential law (Russell et al., 1978) and the normalization value of $^{88}Sr/^{86}Sr$ = 8.37861 (Moore et al., 1982) were used for instrumental mass bias corrections. Each sample measurement comprised 200 integrations of the isotope ratios. Note that abundances of ^{84}Sr could not be determined in this measurement due to low signal/noise ratio and insufficient calibrations of the Faraday cup position. However, the defect of ^{84}Sr data was not problematic in this study because the target of this measurement was detection of the radiogenic ^{87}Sr excesses and the nucleosynthetic isotope anomalies were not considered.

Trace element (Rb, Sr, REE, and Hf) abundances of the nine diogenites were measured by an Agilent 7700x ICP-MS at Nagoya University. The measurement was performed using the He mode of the ICP-MS to decrease the interferences from polyatomic ions onto the target isotopes. Concentrations of the trace elements were determined by calibration curve method. Interferences from oxides of Ba and lighter REE

onto heavier REE were corrected using factors of the oxide formation obtained from analyses of test solutions.

Table 7. Details of diogenite samples used in this study.

Sample	Abbreviation	Type[a]	Brecciation[b]	Comment
Recent-fall				
Bilanga	BL	D	brecciated	
Johnstown	JT	D	brecciated	
Tatahouine	Ta	D	unbrecciated	
Desert-find				
Hamara	HM	D	brecciated	provisional sample
LMT 042	LMT	Ol D	brecciated	provisional sample
NWA 5480	NWA	Ol D	unbrecciated	impact-melt breccia[d]
Antarctic-find				
Y 74013	Y13	D	unbrecciated	recrystallized texture[e], pair with Y 74097[e]
Y 74097	Y97	D	unbrecciated	recrystallized texture[e], pair with Y 74013[e]
Y 002875	Y875	D	unbrecciated	

Notes. [a]D: diogenite, Ol D: olivine diogenite. Cited from Barrat et al. (2010) and *Meteoritical Bulletin Database* (2020).
[b]Cited from Barrat et al. (2010) and *Meteoritical Bulletin Database* (2020).
[d]Totally remelted by shock event except for olivine grains (Yamaguchi et al., 2015).
[e]Recrystallized by shock event (Takeda et al., 1981; Yamaguchi et al., 2011).

Table 8. Dry weights of residue and leachate fractions.

Sample	Sample powder (g)[a]	Residue (g)[b]	Leachate (g)[c]
Bilanga	1.2397	1.2196	0.0511
Johnstown	1.3085	0.6771	0.0559
Tatahouine	1.0306	0.6693	0.0505
Hamara	1.1171	—	0.0490
LMT 042	0.9652	—	0.1292
NWA 5480	1.2595	(1.6406)[d]	0.2106
Y 74013	1.0125	0.9825	0.0555
Y 74097	1.0612	1.0322	0.0477
Y 002875	1.0190	1.0022	0.0317

Notes. [a]Weights of sample powders used for the HCl-leaching experiments.
[b]Dry weights of residue fractions of the HCl-leaching.
[c]Dry weights of leachate fractions of the HCl-leaching.
[d]This value is unrealistically higher than the weight of the sample powder probably due to insufficient dryness.

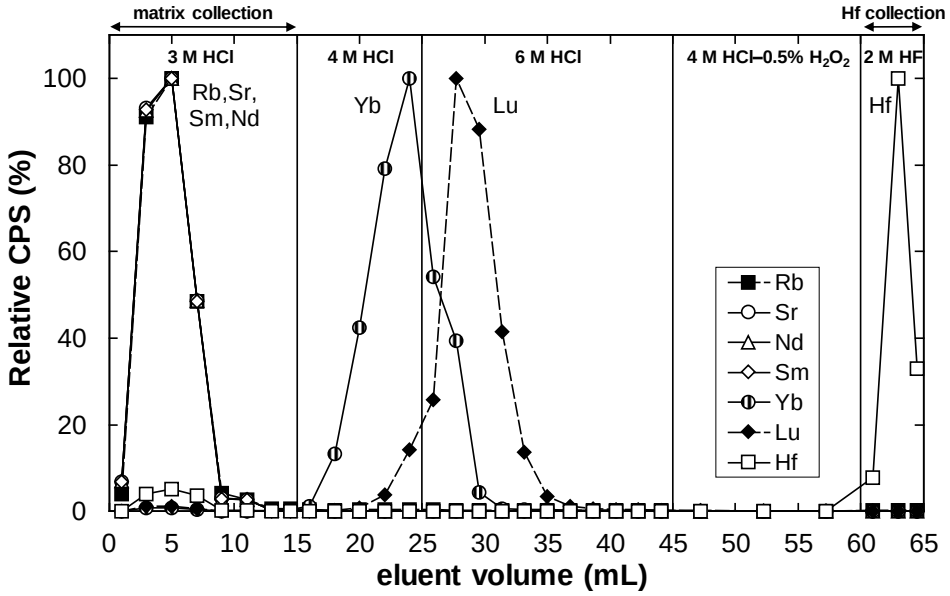

Figure 19. Elution behaviors of Rb, Sr, Nd, Sm, Yb, Lu, and Hf from Ln-Spec resin measured by ICP-MS. The vertical axis shows relative values of count per second (CPS) of elements in each eluted fraction normalized by the maximum value. The horizontal axis represents cumulative volume of solution eluted from the column. Strontium and Nd are efficiently eluted with 3 M HCl. Hafnium is collected by 2 M HF after the elution of Yb and Lu with 4 M HCl and 6 M HCl respectively.

Table 9. Resin chemistry procedure for the separation of Sr and Hf.

Step	Eluent volume	Acid
Column I (Ln-Spec 2mL, 0.8 cm inner diameter, 4 cm length)		
Preparation	20 mL × 3 times	6 M HCl–0.2M HF
Preconditioning	7 mL × 3 times	3 M HCl
Loading sample[a]	5 mL	3 M HCl
Eluting matrix[a]	5 mL × 2 times	3 M HCl
Eluting matrix	5 mL × 3 times	4 M HCl
Eluting matrix	5 mL × 4 times	6 M HCl
Eluting Ti[b]	10 mL × several times[c]	4 M HCl–0.5% H_2O_2[d]
Collecting Hf	5 mL	2 M HF
Column II (Sr-Spec 0.5 mL, 0.2 cm inner diameter, 4 cm length)		
Preparation	5 mL × 3 times	H_2O
Preconditioning	2.5 mL	3 M HNO3
Loading sample	0.5 mL	3 M HNO3
Eluting matrix	2.5 mL	3 M HNO3
Collecting Sr	3 mL	Hot H_2O (50°C)

Notes. Column I and II are based on Yang et al. (2010) and Sakuma et al. (2018) respectively.
[a]The eluted portions were collected for Sr purification in column II step.
[b]High abundance of Ti causes systematic shifts of $^{176}Hf/^{177}Hf$ ratio in MC-ICP-MS measurement (Münker et al., 2001).
[c]This acid was loaded on the column until eluted solution appeared to be colorless; Color of the solution is orange to red when Ti is present. In this study, 2 times were enough for the diogenite samples.
[d]For reducing the occurrence of flow-preventing bubbles in the column, this acid was freshly prepared and had been kept at the low temperature environment (~5°C) just before its use.

Table 10. Cup configuration for Hf isotope measurement by MC-ICP-MS in static mode.

Cup	L4	L3	L2	L1	C	H1	H2	H3
Mass	172	174	175	176	177	178	179	180
Element	Yb	Yb+Hf	Lu	Yb+Lu+Hf	Hf	Hf	Hf	Hf+Ta+W

Table 11. Cup configuration for Sr isotope measurement by TIMS in dynamic mode.

Cup	L2	L1	Ax	H1	H2
Sequence 1	^{84}Sr	^{85}Rb	^{86}Sr	$^{87}Rb + {}^{87}Sr$	^{88}Sr
Sequence 2	^{85}Rb	^{86}Sr	$^{87}Rb+{}^{87}Sr$	^{88}Sr	—
Sequence 3	^{86}Sr	$^{87}Rb+{}^{87}Sr$	^{88}Sr	—	—

4.3. Results and discussion

4.3.1. REE abundances of diogenites

The trace element abundances of the nine diogenites measured by the ICP-MS are listed in Table 12 and the CI-chondrite normalized REE abundance patterns are shown in Figure 20 and Figure 21. Concentrations of the elements in the residue and leachate fractions shown in Table 12 represent the weight proportions of the elements in individual fractions to the sample powders used for the HCl-leaching experiments. $(La/Lu)_n$, $(La/Sm)_n$, $(Dy/Lu)_n$, and $(Lu/Hf)_n$ are concentration ratios of these elements normalized by the CI-chondrite values (Anders and Grevesse, 1989), where $(La/Sm)_n$ and $(Dy/Lu)_n$ represent slopes of lighter REE (LREE) and heavier REE (HREE) enrichments in the REE-pattern plot, respectively. Ce/Ce* and Eu/Eu* show magnitudes of abundance anomalies of Ce and Eu in the REE-pattern plot relative to neighbor elements, i.e., $Ce/Ce^* = Ce_n/(La_n \times Pr_n)^{1/2}$ and $Eu/Eu^* = Eu_n/(Sm_n \times Gd_n)^{1/2}$, where La_n, Ce_n, Pr_n, Sm_n, Eu_n, and Gd_n are CI-normalized concentrations of these elements. Concentrations of the elements in the residues and leachates expressed as the weight proportion of the elements to dried sample weights after the HCl-leaching are shown in Table 13. Note that since the fragments used for the whole-rock and HCl-leaching analysis were obtained from individually different parts of the original meteorite samples, trace element data are not necessarily consistent between the WR and residue and leachate.

4.3.1.1. Characteristics of REE abundances of diogenites and effects of HCl-leaching

Most of the WR and residue fractions of the nine diogenites show sub-chondritic REE abundances (Figure 20) characterized by HREE enrichments (WR, $(Dy/Lu)_n = 0.25–0.89$; residue, $(Dy/Lu)_n = 0.21–0.92$; Table 12) and negative Eu anomalies (WR, $Eu/Eu^* = 0.33–0.88$; residue, $Eu/Eu^* = 0.11–0.57$; Table 12). These characteristics are consistent with REE partitioning coefficients between orthopyroxene, major constituent of diogenites, and melts (Figure 22; Schwandt and McKay, 1998; Sun and Liang, 2013), while the LREE abundance patterns of the nine diogenites (Figure 20a and b) are not necessarily consistent with the partitioning coefficients. The disagreement between the LREE patterns and partitioning coefficients is simply explained by lower abundances of LREE in diogenite pyroxenes relative to those of HREE. LREE abundance patterns of

diogenites are easily affected by the presence of terrestrial contaminants and Ca-phosphates, which generally show LREE-enriched REE abundances. In contrast to WRs and residues, most of the leachate fractions of the nine diogenites show positive Eu anomalies and flat to LREE-enriched REE patterns (Figure 20c). These characteristics are obviously opposite to those of orthopyroxene/melt partitioning coefficients (Figure 22), indicating that accessory minerals and terrestrial contaminants are effectively dissolved by the HCl-leaching.

Comparing the REE abundance patterns between the WRs and residues (Figure 21), those of the residues are more consistent to the patterns of partitioning coefficients (Figure 22). Values of $(La/Sm)_n$ and Eu/Eu* ratios are generally lower in the residues than in the WRs (Figure 23a and d), i.e., LREE depletions and negative Eu anomalies are clearer in the residues. This suggests that accessory LREE and Eu-rich components are effectively removed from the residue samples by the HCl-leaching and that the residue fractions represent trace element compositions of diogenite pyroxenes more correctly than the WR fractions. However, despite the effective removal of the HCl-soluble accessory phases from the samples, some of the residue fractions of the diogenites show LREE enrichments (Figure 20b) that are apparently inconsistent with the REE partitioning coefficients (Figure 22). This is probably due to the presence of HCl-resistant LREE-rich components in these samples. Such LREE enrichments were also observed in 6 M HCl-washed residue samples of diogenites analyzed by Barrat et al. (2010). Hence, LREE abundance patterns of diogenites do not necessarily represent trace element compositions of pure pyroxenes in diogenites.

Contrary to $(La/Sm)_n$ ratios, values of $(Dy/Lu)_n$ ratios do not show considerable changes between the WRs and residues (Figure 23a and b). Furthermore, the HREE abundance patterns of the WRs and residues (Figure 20) are consistent with the pyroxene/melt partitioning coefficients (Figure 22). This indicates that HREE compositions of the diogenites are robust to presence of Ca-phosphates and terrestrial contaminants. Therefore, it is plausible to assume that HREE abundance patterns of the residue fractions correctly reflect trace element compositions of pure diogenite pyroxenes.

4.3.1.2. Cerium anomalies in diogenites and terrestrial weathering

Some of the nine diogenite samples show slight but significant both positive and negative Ce anomalies (Ce/Ce* = 0.92–1.3; Table 12) in the REE abundance patterns (Figure 20). Since recent-fall (i.e., non-weathered) eucrites and their constituent minerals, including zircon, do not show significant Ce anomalies (e.g., Barrat et al., 2007; Haba et al., 2014), the Ce anomalies in the diogenites are probably related to terrestrial weathering and contamination. LREE abundance patterns of diogenites are easily modified by these processes due to lower LREE contents in diogenites relative to those in eucrites.

For the three Antarctic diogenites, positive Ce anomalies (Ce/Ce* ~ 1.1; Table 12) observed in the WR fractions are probably due to dissolution of easily soluble minerals (e.g., Ca-phosphates) during Antarctic weathering. Since Ce^{4+} is less soluble than trivalent REE, Ce^{4+} retains on the meteorite samples while other REE are removed following the dissolution of minerals (e.g., Crozaz et al., 2003). Significantly lower REE contents in the leachate fractions of the three Antarctic diogenites relative to those of the other samples (Table 12) support this idea. A large positive Ce anomaly in the leachate of Y 002875 (Ce/Ce* = 1.3) is also consistent with presence of such a residual Ce^{4+} in the WR samples. The HCl-leaching in this study removed the residual Ce from the Antarctic diogenite samples and, consequently, the residue fractions do not show clear Ce anomalies.

In the case of the recent-fall and desert-find diogenites, the WR fractions of Tatahouine and NWA 5480 show significant positive Ce anomalies (Tatahouine, Ce/Ce* = 1.2; NWA 5480, Ce/Ce* = 1.1; Table 12), while other four samples do not show significant anomalies (Figure 20a). Contrary to the Antarctic diogenites, the leachate fractions of these diogenites contain large amount of REE comparable with the residue fractions (Figure 21). Therefore, Ce anomalies in the WR fractions of these diogenites is difficult to explain only by the dissolution processes and an additional process of a formation of iron-hydroxides should be considered. Iron-hydroxides, which display positive Ce anomalies, are often formed on clacks in meteorites during their terrestrial residence (e.g., Barrat et al., 1999). This process possibly causes significant positive Ce anomalies in weathered meteorite samples. Iron-hydroxides in the non-Antarctic diogenites are dissolved by the HCl-leaching because of their weak acid-resistance and, consequently, the residue fractions do not show significant Ce anomalies (Figure 20b).

However, acid-resistant terrestrial contaminants showing no Ce anomalies may remain in the residue fractions. Therefore, chemical and isotopic data of the diogenite samples showing significant Ce anomalies should be carefully addressed. A large Ce anomaly in the residue fraction of Johnstown digenite (Figure 23c) is due to anomalously steep LREE depletion in its REE pattern (Figure 20b) and is not a genuine anomaly.

4.3.1.3. Europium anomalies in diogenites

The residue fractions of the nine diogenites show a large variation of magnitudes of negative Eu anomalies (Eu/Eu* = 0.11–0.59; Table 12). Since the residue fractions are likely to represent REE compositions of pure diogenite pyroxenes (see 4.3.1.1. Characteristics of REE abundances of diogenites and effects of HCl-leaching), the variation of Eu anomalies is probably related to parent body processes.

A possible origin of Eu anomalies of diogenites is a variation of oxygen fugacities in diogenite source regions. Since Eu anomaly is caused by a divalent behavior of Eu in reduced conditions, oxygen fugacity primarily controls a degree of Eu anomaly. On the bases of a thermochemical modelling of diogenite differentiations using the pMELTS program (Ghiorso et al., 2002), Mitchel and Tomkins (2019) proposed presence of slight but significant variations of fO_2 values (ΔIW of −1.6 to −1.8) in diogenite source regions. However, an Eu partitioning model by McKay et al. (1994) demonstrates that this fO_2 variation do not result in significant variation of Eu anomalies and insufficient to reproduce the large variation of Eu anomalies in the nine diogenites. Therefore, a contribution of a fO_2 variation on the Eu anomalies of the nine diogenites should be negligible.

According to Barrat et al. (2010), the Eu anomalies in diogenites are explained by involvements of partial melts of eucritic crusts on differentiation processes of diogenites. In their model, parental melts of diogenites are formed by remelting of magma ocean cumulates after the solidification of global magma ocean. Parental melts of diogenites interact with eucritic upper crust and mixed with its partial melts during their uplifts. Diverse $(Dy/Lu)_n$ and Eu/Eu* ratios of diogenites can be explained by variations of mixing ratios between partial melts of magma ocean cumulate and eucritic upper crust. Alternatively, Mittlefehldt et al. (2012) suggested that subsolidus diffusion played a significant role to produce the variation of Eu anomalies in diogenites. Since a diffusion

of divalent Eu^{2+} is much faster than those of trivalent REE^{3+} (Cherniak and Liang, 2007), Eu^{2+} in diogenite pyroxenes may have reequilibrated with adjacent accessory minerals by later thermal events (e.g., impact events) after their crystallization, while REE^{3+} did not mobilized. This process also can reproduce the variation of Eu anomalies in diogenites.

4.3.1.4. Flat to La-enriched LREE patterns of Bilanga, Tatahouine, and NWA 5480

Although most of the residue fractions of the nine diogenites show La-depleted and Sm-enriched patterns in LREE regions of the REE abundance patterns, Bilanga, Tatahouine, Hamara, and NWA 5480 display anomalously La-rich (i.e., $(La/Sm)_n \geq 1$; Table 12) LREE abundance patterns (Figure 20b). These LREE enrichments suggests presence of acid-resistant LREE-rich components in these diogenite samples. For Tatahouine and NWA 5480, such La-rich REE patterns were also reported by previous studies (Takahashi and Masuda, 1990; Barrat et al., 1999; 2008; 2010), while the origin of La enrichments was not discussed in detail there.

For Bilanga, the presence of a significant amount of plagioclase in the sample may be contribute to the LREE enrichment. According to the petrographic analysis by Domanik et al. (2004), Bilanga contains large exotic plagioclase clasts derived from different source rocks. Because of its high LREE contents, plagioclase can vary LREE abundance patterns of diogenites significantly even if its abundance in diogenites is as low as 1% (Barrat et al., 2010). However, the largest negative Eu anomaly of the Bilanga among the residue fractions of the nine diogenites ($Eu/Eu^* = 0.11$; Table 12) rules out significant contributions of plagioclase on the REE abundance of Bilanga. If the REE abundance pattern of Bilanga were affected by plagioclase, the negative Eu anomaly of Bilanga should be erased or strongly decreased due to large positive Eu anomaly of plagioclase (Barrat et al., 2010). Although a contamination of chondritic materials through brecciation processes (e.g., Zolensky et al., 1996; Gounelle et al., 2003; Prettyman et al., 2012) is also capable to contribute LREE enrichments in diogenites, low highly siderophile element abundances in Bilanga ($CI \times 10^{-4}$; Dale et al., 2012) rule out significance of this effect.

The LREE enrichments in the residue fractions of Tatahouine and NWA 5480 are more difficult to explain. In contrast to Bilanga, these two diogenites show non-brecciated textures and do not contain a significant amount of plagioclase (Barrat et al., 1999;

Yamaguchi et al., 2015). Therefore, their LREE enrichments should not be produced by the presence of plagioclase clasts. For NWA 5480, an impact melting brecciation might be related to its LREE enrichment. Although NWA 5480 do not show obvious evidences of chondritic contaminations in their texture, its high platinum group element (PGE) abundances (CI × 10^{-3}; Dale et al., 2012; Day et al., 2012; Yamaguchi et al., 2015) record significant chondritic contaminations by an impact melting brecciation (Yamaguchi et al., 2015). However, the degree of chondritic contamination in NWA 5480 inferred from its PGE abundances (0.1%; Yamaguchi et al., 2015) is not enough to account for the LREE abundances of NWA 5480. For reproducing the La enrichment in NWA 5480 (CI × 10^{-2}; Figure 21f), ~1% of chondritic contamination is required. Hence, an impact melting brecciation cannot simply explain the La enrichment in NWA 5480.

Interestingly, the WR and residue fractions of Tatahouine and NWA 5480 show quite similar characteristics of REE abundances (i.e., positive Ce anomalies, La enrichments, and strong HREE enrichments), despite different types and degrees of terrestrial weathering that they suffered from. This strongly suggests that characteristics of their REE abundances are originated in their parent body, while processes that produced their La enrichments are unclear.

4.3.1.5. Characteristics of REE abundances of olivine diogenites

Two olivine diogenites analyzed in this study (LMT 042 and NWA 5480) show no remarkable similarities in their REE abundances. On the one hand, NWA 5480, together with Tatahouine, is the most REE-poor sample among the nine diogenites used in this study (Figure 20b), suggesting its crystallization from non-fractionated primitive melt. On the other hand, LMT 042 is the most REE-rich sample among the nine diogenites (Figure 20 b), suggesting its crystallization form highly fractionated melt. This indicates that presence of olivine does not significantly affect REE abundances of diogenites.

4.3.2. ^{176}Lu–^{176}Hf systematics of diogenites

The ^{176}Lu–^{176}Hf isotope compositions of the nine diogenites determined by the MC-ICP-MS are listed in Table 14. Elemental ratios of Lu/Hf determined by the ICP-MS (Table 12) are converted to ^{176}Lu/^{177}Hf ratios (Table 14) using recommended values of standard isotope ratios of these elements (Meija et al., 2016). A ^{176}Hf/^{177}Hf ratio of

0.281876 ± 0.000008 was obtained for an Hf standard material of JMC 475 by the MC-ICP-MS measurement in this study, which is slightly higher than the recommended value of 0.282163 ± 0.000009 by Blichert-Toft et al. (1997).

The external ^{176}Lu–^{176}Hf isochron diagrams for the WR, residue, and leachate fractions of the nine diogenites are shown in Figure 24 and the internal isochron diagrams are shown in Figure 25. The ^{176}Lu–^{176}Hf data set of the residue fractions defines a meaningful regression line on the isochron diagram (Figure 24b), while the other two data set of WRs and leachates are scattered (Figure 24a and c). Note that contributions of elemental fractionations of Lu and Hf during the HCl-leaching experiments on the $^{176}Lu/^{177}Hf$ ratios of the residue fractions should be insignificant, considering the lower contents of Lu and Hf in the leachate fractions than those in the residues (Table 12).

4.3.2.1. ^{176}Lu–^{176}Hf age and initial $^{176}Hf/^{177}Hf$ ratio of diogenites

The ^{176}Lu–^{176}Hf age of 4.40 ± 0.38 Ga and initial $^{176}Hf/^{177}Hf$ ratio of 0.2820 ± 0.0013 are calculated from the ^{176}Lu–^{176}Hf data set of the residue fractions of the nine diogenites (Figure 24b) using the model 3 fit (McIntyre et al., 1966) of the Isoplot software (Ludwing, 2012). This initial $^{176}Hf/^{177}Hf$ ratio is significantly higher than the reference eucrite value (0.27977 ± 0.00008; Bouvier et al., 2015), while the ^{176}Lu–^{176}Hf age is identical to that of eucrites (4.59 ± 0.15 Ga; Bouvier et al., 2015) within the error range. The ^{176}Lu–^{176}Hf age of the nine diogenites is also consistent with published formation ages of diogenites determined by ^{26}Al–^{26}Mg (Schiller et al., 2011; Hublet et al., 2017), ^{53}Mn–^{53}Cr (Lugmair and Shukolyukov, 1998; Trinquier et al., 2008; Day et al., 2012), ^{60}Fe–^{60}Ni (Tang and Dauphas, 2012), and ^{87}Rb–^{87}Sr (Birck and Allègre, 1981; Takahashi and Masuda, 1990) decay systems within the error range.

The substantial discrepancy in the initial $^{176}Hf/^{177}Hf$ ratios between eucrites and diogenites indicates their differentiation from individually distinct source materials. Note that, although a neutron capture reaction can induce a positive shift of $^{176}Hf/^{177}Hf$ ration in meteorite sample thorough its cosmic-ray exposure, the magnitude of this shift (up to ~+4 ε-unit in typical neutron fluence conditions; Sprung et al., 2010) is negligible, compared with the uncertainty of the initial $^{176}Hf/^{177}Hf$ ratio of the nine diogenites (~50 ε-unit). The significant scattering of data points of the residue fractions around the

regression line (MSWD = 30; Figure 24b) possibly reflects variations of ^{176}Lu–^{176}Hf ages and initial $^{176}Hf/^{177}Hf$ ratios of the individual diogenite samples.

4.3.2.2. Disturbance by terrestrial contamination

The disturbance of the ^{176}Lu–^{176}Hf systematics of the WRs is probably due to the presence of terrestrial contaminants in the samples. As mentioned in 4.3.1.2. Cerium anomalies in diogenites and terrestrial weathering, positive Ce anomalies in WR fractions of Tatahouine and NWA 5480 (Figure 23c) indicate the presence of significant amounts of terrestrial contaminants in these samples. Hence, $^{176}Hf/^{177}Hf$ ratios of these samples may be affected by low terrestrial values. Since these two diogenites originally have the highest $^{176}Hf/^{177}Hf$ ratios among the nine diogenites (Figure 24b), even minute amounts of terrestrial contaminations can largely change their $^{176}Hf/^{177}Hf$ ratios. This is consistent with significant deviations of ^{176}Lu–^{176}Hf data points of these two diogenites from the reference eucrite line (Figure 24a). Note that Ce anomalies in the WR fractions of the three Antarctic diogenites of Y 74013, Y 74097, and Y 002875 (Figure 23c) were probably generated by the dissolution processes during Antarctic residence (see 4.3.1.2. Cerium anomalies in diogenites and terrestrial weathering) and, therefore, non-significant deviations of their ^{176}Lu–^{176}Hf compositions from the eucrite line (Figure 24c) do not conflict with this idea.

The ^{176}Lu–^{176}Hf compositions of the leachate fractions of six diogenites (Bilanga, Johnstown, Tatahouine, Hamara, LMT 042, NWA 5480) strongly suggest the presence of terrestrial contaminants in these diogenite samples. All of the ^{176}Lu–^{176}Hf isotope data of the leachates are plotted on righter part of the internal isochron diagrams relative to those of the WRs and leachates (Figure 25), indicating the presence of terrestrial contaminants in all of the six diogenites. Furthermore, the $^{176}Hf/^{177}Hf$ ratios of the leachate fractions of Tatahouine, Hamara, and NWA 5480 are largely different from those of the residue fractions of them (Figure 25c, d, and f), suggesting significant contributions of terrestrial contaminations on Hf isotope compositions of WR fractions. The negative correlation between the Lu/Hf ratios and $^{176}Hf/^{177}Hf$ ratios shown in the external isochron diagram for the leachate fractions (Figure 24c) also suggests the presence of terrestrial Hf in these samples. This negative correlation probably represents the mixing between meteoritic Hf (upper-left endmember) and terrestrial Hf (lower-right endmember). These terrestrial

contaminants are effectively removed from the samples by the HCl-leaching and, consequently, the residue fractions provided the meaningful regression line on the isochron diagram (Figure 24b).

4.3.3. ^{87}Rb–^{87}Sr systematics of diogenites

The ^{87}Rb–^{87}Sr isotope compositions of the nine diogenites determined by the TIMS are listed in Table 14. Elemental ratios of Rb/Sr determined by the ICP-MS (Table 12) are converted to ^{176}Lu/^{177}Hf ratios (Table 14) using recommended values of standard isotope ratios of these elements (Meija et al., 2016). A mean value of ^{87}Sr/^{86}Sr = 0.710248 ± 0.000002 was obtained for an Sr standard material of NIST SRM 987 by the TIMS measurements in this study.

The external ^{87}Rb–^{87}Sr isochron diagrams for the WR, residue, and leachate fractions of the nine diogenites are shown in Figure 26 and the internal isochron diagrams are shown in Figure 27. All of the ^{87}Rb–^{87}Sr data sets of the WR, residue, and leachate fractions do not define meaningful regression lines on the external isochron diagrams (Figure 26).

4.3.3.1. Disturbance by terrestrial contamination and impact event

In contrast to the ^{176}Lu–^{176}Hf systematics, the ^{87}Rb–^{87}Sr systematics of the nine diogenites, are totally disturbed. Disturbances of ^{87}Rb–^{87}Sr systematics of diogenites were also reported by Nakamura (1979) and Birck and Allègre (1981). Since terrestrial contaminations generally induce left-ward shifts of ^{87}Rb–^{87}Sr data points on the isochron diagram (e.g., Nishikawa et al., 1990), the substantial presence of the ^{87}Rb–^{87}Sr data points on the righter part of the isochron diagram (Figure 26) suggests contributions of additional processes other than terrestrial contaminations on the disturbance of the ^{87}Rb–^{87}Sr systematics.

In the external ^{87}Rb–^{87}Sr isochron diagram for the WR fractions (Figure 26a), the data points of Tatahouine and NWA 5480 show the largest deviations from the reference diogenite line (Takahashi and Masuda, 1990) among those of the nine diogenites. This is consistent with the fact that the ^{176}Lu–^{176}Hf compositions of the WR fractions of these two diogenites are strongly affected by terrestrial contaminants (Figure 24a). However, considering the ^{87}Rb–^{87}Sr composition of the leachate fraction of Tatahouine,

mechanisms of the disturbance of the ^{87}Rb–^{87}Sr systematics of diogenites should be more complicated than those of ^{176}Lu–^{176}Hf systematics. In contrast to the case of ^{176}Lu–^{176}Hf systematics (Figure 24c), the ^{87}Rb–^{87}Sr data point of the residue fraction of Tatahouine shows larger deviations from the reference diogenite line relative to that of the leachate (Figure 26c). If the disturbance of the ^{87}Rb–^{87}Sr systematics of the nine diogenites were caused only by terrestrial contaminations, the ^{87}Rb–^{87}Sr compositions of the residue fractions should have been more consistent with the reference line relative to those of the leachates. Therefore, the large deviation of the ^{87}Rb–^{87}Sr data point of the residue of Tatahouine from the reference diogenite line indicates significant contribution of additional processes other than terrestrial contaminations on its ^{87}Rb–^{87}Sr composition. The ^{87}Rb–^{87}Sr composition of the residue of Johnstown also shows such large deviation from the reference line (Figure 27b), supporting this idea. For the desert-find diogenites, the disturbances of their ^{87}Rb–^{87}Sr systematics (Figure 27d, e, and f) are probably due to intensive contaminations of terrestrial Sr, which is also recorded by desert-find eucrites (Hidaka and Yoneda, 2016). On the basis of non-contaminated REE abundance patterns of the three Antarctic diogenites (Figure 21g, h, i), their ^{87}Rb–^{87}Sr systematics should not be severely affected by terrestrial contaminants. Considerably low $^{86}Sr/^{87}Sr$ ratio of the leachate fraction of Y 74013 (0.699208 ± 0.000007; Figure 27e) rules out significant invasion of terrestrial Sr into Antarctic diogenites.

Considering a lower closure temperature of ^{87}Rb–^{87}Sr system (~700°C for whole-rock; Harrison et al., 1979) than that of ^{176}Lu–^{176}Hf system (>900°C for garnet; Anczkiewicz et al., 2007), the ^{87}Rb–^{87}Sr systematics of the nine diogenites are likely to be affected by impact heating on their parental body. ^{40}K–^{40}Ar and ^{40}Ar–^{39}Ar ages of diogenites are mostly younger than 4.0 Ga (Kaneoka et al., 1979; Michel and Eugster, 1 994), indicating impact-resetting of these isotope systems of diogenites after their crystallization. Although ^{87}Rb–^{87}Sr system resists more intense heating relative to ^{40}K–^{40}Ar and ^{40}Ar–^{39}Ar systems (e.g., Harrison et al., 1979), some of impact events which disturbed these noble gas isotope systems of diogenites probably disturbed ^{87}Rb–^{87}Sr isotope system of them.

4.3.3.2. Internal ^{87}Rb–^{87}Sr impact ages of diogenites

As discussed above, ^{87}Rb–^{87}Sr systematics of diogenites probably suffered from impact disturbances. Although the ^{87}Rb–^{87}Sr systematics of the three desert-find diogenites are likely to be severely affected also by terrestrial contaminants, those of the six recent-fall and Antarctic-find diogenites do not significantly affected by terrestrial contaminants. Therefore, a regression for the ^{87}Rb–^{87}Sr data set of the three fractions of individual diogenites can be assumed to represent impact reset ages of them.

Calculated internal ^{87}Rb–^{87}Sr model impact ages of the six recent-fall and Antarctic-find diogenites are listed in Table 15. Since Y 74013 is paired with Y 74097 (Takeda et al., 1981), their model age is calculated together. All of the six diogenites show the initial $^{87}Sr/^{86}Sr$ ratios higher than basaltic achondrite best initial of 0.6989 (Papanastassiou and Wasserburg, 1969; Smoliar, 1993; Hans et al., 2013), suggesting that the regressions represent not mixing trends with terrestrial contaminants but chronologically meaningful relations of ^{87}Rb–^{87}Sr decay system. Interestingly, in contrast to Takahashi and Masuda (1990), Tatahouine do not provide meaningful internal ^{87}Rb–^{87}Sr regressions and Johnstown show relatively young ^{87}Rb–^{87}Sr age of 1626 ± 950 Ma (Table 15). This indicates significantly heterogeneous impact disturbances in these two diogenites. Such heterogeneities in diogenites are also reported by Birck and Allègre (1981). Model ^{87}Rb–^{87}Sr impact ages of Y 74013 and Y 74097 (3305 ± 1500 Ma; Table 15) are significantly older than their noble gas ages of 1150 ± 250 Ma for Y 74013 (Michel and Eugster, 1994) and 1100 ± 250 Ma for Y 74097 (Kaneoka et al., 1979), indicating that these meteorites experienced at least two times of intense impacts. An earlier intense impact at ~3000 Ma probably induced recrystallizations of these two diogenites (Takeda et al., 1981; Yamaguchi et al., 2011) and, subsequently, a relatively moderate impact at ~1000 Ma caused a degassing of noble gases from these two diogenites. A large variation of model ^{87}Rb–^{87}Sr impact ages of the six diogenites (Table 15) indicate frequent occurrences of intense impacts on the Vestan surface later than the lunar cataclysm period of 3.4–4.1 Ga (e.g., Bogard and Garrison, 2003; Marchi et al., 2013).

4.3.3.3. Implication for the origin of Eu anomalies in diogenites

As mentioned in 4.3.1.3. Europium anomalies in diogenites, there are two hypotheses for the origin of the variation of Eu anomalies in diogenites; contaminations

of eucritic melts (Barrat et al., 2010) and subsolidus reequilibration (Mittlefehldt et al., 2012). The disturbances of ^{87}Rb–^{87}Sr systematics of the nine diogenites strongly support the occurrence of significant subsolidus diffusions of Eu in these diogenites. Since the ionic radius of Sr^{2+} (1.25 Å, 8-fold coordination; Shannon, 1976) similar to that of Eu^{2+} (1.26 Å, 8-fold coordination; Shannon, 1976), they show similar diffusion behaviors (e.g., Liang et al., 2004; Cherniak and Liang, 2007). Therefore, the disturbance of ^{87}Rb–^{87}Sr systematics of the diogenites, which indicates a reequilibration of Sr isotope composition in the diogenites, also indicates a reequilibration of Eu^{2+} in the diogenites. Furthermore, non-disturbed ^{176}Lu–^{176}Hf systematics of the residue fractions of the nine diogenites indicates that REE^{3+} and Hf^{4+} in the diogenites are not reequilibrated by thermal events that reequilibrate Sr^{2+} and Eu^{2+} in the diogenites due to relatively low diffusivities of REE^{3+} and Hf^{4+} (e.g., Cherniak and Liang, 2007; Bloch et al., 2017). In this case, Eu^{2+} can disperse from diogenite pyroxenes leaving REE^{3+} behind (Mittlefehldt et al., 2012). This process possibly produced the variation of Eu anomalies in diogenites, while there are no direct evidences for that at present.

4.3.4. Differentiation process of diogenites

4.3.4.1. Source material of diogenites

As mentioned in 4.3.2.1. ^{176}Lu–^{176}Hf age and initial ^{176}Hf/^{177}Hf ratio of diogenites, the substantial discrepancy in the initial ^{176}Hf/^{177}Hf ratios between eucrites and diogenites indicates their differentiation form individually distinct source materials. Here, geochemical properties of source materials of diogenites are discussed in detail.

Figure 28 shows the temporal evolution of the Hf isotope composition by the decay of ^{176}Lu to ^{176}Hf. The vertical axis of εHf represents the fractional deviation of ^{176}Hf/^{177}Hf ratio from chondritic uniform reservoir (CHUR) value (Bouvier et al., 2008) at certain time *T*,

$$\varepsilon\mathrm{Hf} = \left[\frac{(^{176}\mathrm{Hf}/^{177}\mathrm{Hf})^{T}_{\mathrm{sample}}}{(^{176}\mathrm{Hf}/^{177}\mathrm{Hf})^{T}_{\mathrm{CHUR}}} - 1\right] \times 10^{4}, \quad (4)$$

where $(^{176}\mathrm{Hf}/^{177}\mathrm{Hf})^{T}_{\mathrm{sample}}$ and $(^{176}\mathrm{Hf}/^{177}\mathrm{Hf})^{T}_{\mathrm{CHUR}}$ are the ^{176}Hf/^{177}Hf ratio of a sample and CHUR at a time *T*, respectively. A black diamond in Figure 28 represents the ^{176}Lu–^{176}Hf age and the initial ^{176}Lu–^{176}Hf age of diogenites given in this study (Figure 24b). Dashed lines display the evolutions of Hf isotope compositions of model reservoirs,

which differentiated from CHUR at 4.6 Ga with individually different $(Lu/Hf)_n$ ratios. The gray line shows CHUR compositions (i.e., Hf isotope evolution with $(Lu/Hf)_n = 1$). As shown in Figure 28, the ^{176}Lu–^{176}Hf age and the initial $^{176}Hf/^{177}Hf$ ratio of the diogenites are consistent with the evolution of model reservoir characterized by high $(Lu/Hf)_n$ ratio of >8, while those of eucrites (Bouvier et al., 2015) are consistent with the chondritic εHf evolution (Figure 28). This strongly indicates the presence of the highly fractionated geochemical reservoir showing superchondritic $(Lu/Hf)_n$ ratio at the early stage of Vesta. Note that the Hf evolution diagram (Figure 28) is robust if other ^{176}Lu–^{176}Hf CHUR compositions are employed. Three published CHUR compositions (Blichert-Toft and Albarède, 1997; Patchett et al., 2004; Iizuka et al., 2015b) were tested as $(^{176}Hf/^{177}Hf)^{T}_{CHUR}$ in Equation (4) and no recognizable differences were observed in the evolution diagram; being absolutely the same as Figure 28, the diagrams for these three CHUR compositions are not shown here.

To meet these chronological and geochemical requirements, the most possible source material of diogenites is the Vestan mantle. Assuming the formation of planetary-scale magma ocean on Vesta (e.g., Greenwood et al., 2014), an olivine-rich mantle is the first crystallizing phase from the magma ocean (e.g., Righter and Drake, 1997; Mandler and Elkins-Tanton, 2013). Furthermore, the magma ocean with a chondritic $(Lu/Hf)_n$ ratio produce an olivine-rich mantle characterized by a superchondritic $(Lu/Hf)_n$ ratio on the basis of the experimentally obtained olivine/melt partitioning coefficients of Lu and Hf (D_{Lu}/D_{Hf} = 4.35–35.5; Kennedy et al., 1993; Zanetti et al., 2004). Although mantle-like materials apparently derived from Vesta has not yet been discovered among the present-day meteorite collections, the subchondritic $(Lu/Hf)_n$ ratios of eucrites (~0.85 as an average of sixteen basaltic eucrites; Blichert-Toft et al., 2002) also supports the probability of the high $(Lu/Hf)_n$ ratio of the Vestan mantle.

4.3.4.2. Trace element diversity of diogenites and partial melting of the Vestan mantle

The orthopyroxenitic mineral compositions of diogenites are highly favorable for modeling their differentiation processes, allowing us to assume that orthopyroxene is the only crystallizing solid from melts during the formation of diogenites. In this case, evolutions of trace element contents in the melts following diogenite crystallizations can be simply calculated using orthopyroxene/melt partitioning coefficients and appropriate

differentiation models. As discussed in subsection 4.3.1.1. Characteristics of REE abundances of diogenites and effects of HCl-leaching, $(Dy/Lu)_n$ ratios of the residue fractions of the diogenites are likely to reflect REE compositions of pure pyroxenes. Here, these modelling approach are applied to the $(Dy/Lu)_n$ data of the residue fractions of the nine diogenites for investigating differentiation processes of diogenites.

To test the validity of conventional magma ocean crystallization models for diogenite differentiation (e.g., Takeda, 1979; Righter and Drake,1997; Ruzicka et al., 1997), $(Dy/Lu)_n$ variations of pyroxenes produced by a fractional crystallization of a single melt are investigated. In this model, the concentration of element *i* in the melt c_l^i can be written as

$$c_l^i = c_{l,0}^i f^{D_i - 1}, \quad (5)$$

where $c_{l,0}^i$ is the initial concentration of element *i* in melt, *f* is the weight fraction of residual melt, and D_i is the partitioning coefficient of element *i* between the crystallizing minerals and melt (Allègre and Minster, 1978). Adopting orthopyroxene/melt partitioning coefficients of Dy and Lu (Schwandt and McKay, 1998; $D_{Dy} = 0.050$, $D_{Lu} = 0.104$; mean values for five measurements) to D_i and parental melt composition of Tatahouine that is back calculated using the partitioning coefficients to $c_{l,0}^i$, c_l^i values are determined as a function of *f* (Figure 29). The white circles in Figure 29 display the calculated $(Dy/Lu)_n$ ratios of orthopyroxenes produced by the fractional crystallization of the parental melt of the Tatahouine. As shown in Figure 29, the fractional crystallization of a single melt results in an extremely small variation of $(Dy/Lu)_n$ ratios (white circles) relative to that of the residues of the nine diogenites (black circles). This strongly indicates the crystallization of diogenites from not a global magma ocean but compositionally diverse multiple melts. It should be noted that although REE partitioning behavior depends on *P*–*T*–*X* conditions (e.g., Yao et al., 2012; Sun and Liang, 2013), this dependence is negligible when considering D_{Dy}/D_{Lu} ratio.

A partial melting can account for both the Vestan mantle origin of diogenites (Figure 28) and the compositional variation of diogenites (Figure 29). To test the validity of the partial melting as the differentiation process of diogenites, possible compositional variations of the partial melts of the Tatahouine and NWA 5480 diogenites are estimated. These two diogenites shows the highest Dy/Lu and Lu/Hf ratios among the nine diogenites (Table 12). On the basis of the incompatible element-depleted or relatively

mantle-like compositions of these two diogenites, they were chosen as starting materials of the partial melting calculation. The variations of $(Dy/Lu)_n$ and $(Lu/Hf)_n$ ratios of partial melts of the Tatahouine and NWA 5480 are calculated using the numerical model of batch partial melting (Allègre and Minster, 1978):

$$c_l^i = \frac{c_{s,0}^i}{D_i + f(1-D_i)}, \quad (6)$$

where c_l^i is the concentration of element *i* in the partial melt, $c_{s,0}^i$ is the initial concentration of element *i* in solid phase, *f* is the weight fraction of the partial melt, and D_i is the partitioning coefficient of element *i* between solid phase and melt. The olivine/melt partitioning coefficients of Dy, Lu, and Hf (Zanetti et al., 2004; $D_{Dy} = 0.0025$, $D_{Lu} = 0.063$, $D_{Hf} = 0.0037$; D_{Lu} was calculated from the lattice strain parameters shown in Table 3 of Zanetti et al., 2004) are substituted to D_i in Equation (6), while the concentrations of Dy, Lu, and Hf of the residues of Tatahouine and NWA 5480 are substituted to $c_{s,0}^i$. As shown in Figure 30, the partial melts of the Tatahouine and NWA 5480 display broad ranges of $(Dy/Lu)_n$ and $(Lu/Hf)_n$ ratios (black crosses), which are comparable to those of the residues of the nine diogenites (black diamonds) and reference diogenite data (white diamonds; Barrat et al., 2010). In this case, the variation of trace element compositions of diogenites can be explained by the variation of degree of partial melting.

Wilson and Keil (1996) demonstrated that later-formed partial melts are more likely to be trapped at deeper part of the Vestan crust as dikes or sills and not to erupt at surface as a consequence of successive decrease of the density of the crust due to impact events. This supports the crystallization of diogenites as cumulates from later-formed partial melts of the Vestan mantle. Furthermore, the presence of chemically equilibrated and unequilibrated diogenites reported by Yamaguchi et al. (2011), suggesting the presence of diogenites that crystallized at shallower depth in the Vestan crust than expected by conventional magma ocean model, is consistent with the formation of diogenites as intrusions.

Although Barrat et al. (2010) proposed the mixing of the partial melt fractions between the mantle and eucritic crust as the origin of the compositional diversity of the diogenite parental melts, the discrepancy in the initial $^{176}Hf/^{177}Hf$ ratios between eucrites and diogenites (Figure 28) rules out such a significant involvement of the eucritic melts

in the crystallization of diogenites. If the compositional diversity of diogenites resulted from the mixing between the partial melts of the Vestan mantle and those of the eucritic crust, the initial $^{176}Hf/^{177}Hf$ ratio of diogenites would be similar to that of eucrites. Therefore, diogenites should be crystallized from partial melts of the Vestan mantle that is not directly related to the eucritic melts. Note that, in this case, the variation of Eu anomalies in diogenites should be explained by subsolidus reequilibration proposed by Mittlefehldt et al. (2012), which is consistent with the disturbances of the ^{87}Rb–^{87}Sr systematics of the nine diogenites (see 4.3.2.1. ^{176}Lu–^{176}Hf age and initial $^{176}Hf/^{177}Hf$ ratio of diogenites). The complicated relationship between $(Dy/Lu)_n$ and Eu/Eu* of diogenites shown in Figure 31 also suggests that the origin of the variation of Eu anomalies in diogenites is not a simple mixing between mantle partial melts and crustal partial melts.

The partial melting model of this study described above indicates spatially separated origins of eucrites and diogenites. However, the broadly howarditic composition of the Vestan surface revealed by the Dawn spacecraft (e.g., Ammannito et al., 2013a; Beck et al., 2017) apparently conflicts with the spatial separation between eucrites and diogenites. One of the most plausible solutions for this problem is the hit-and-run collusion model proposed by Haba et al. (2019). Based on the presence of two distinctive populations of zircon ^{207}Pb–^{208}Pb ages of mesosiderites, they newly constructed the mesosiderite formation model comprising a large-scale disruption by a catastrophic collision and a subsequent accretion of collisional debris. In their model, the Vestan surface is covered with the accreted collisional debris that are mixture of the Vestan crust, mantle, and core materials, which is certainly consistent with the howarditic composition of the Vestan surface regardless of the original structure of the Vestan crust. Therefore, diogenites are likely to be crystallized from the partial melts of the Vestan mantle and, subsequently, be excavated by the hit-and-run collision to accrete on the Vestan surface again as mixtures with eucritic materials.

An alternative model that possibly explains the diogenite data given in this study is a shallow magma ocean model described by Neumann et al. (2014). They constructed a numerical model of the thermal evolution of Vesta considering partitioning and transport of ^{26}Al associated with migrations of silicate melts. In their model, a shallow magma ocean with a thickness of up to few tens of km is formed in subsurface layer of Vesta and a planetary-scale magma ocean assumed in many other models (e.g., Righter and Drake

1997; Barrat et al. 2008, 2010; Mandler and Elkins-Tanton 2013) is not formed due to efficient heat transport by the partitioning of ^{26}Al into silicate melts. Their model shows that though the lifetime of the shallow magma ocean is ~10^4–10^6 years, the magmatism in deeper part of the Vestan mantle proceeds for up to 150 Ma. Upward migrations of incompatible element-rich silicate melts from the deeper mantle possibly causes a depletion of incompatible elements (i.e., increase Lu/Hf ratio) there. Thus, this deeper mantle has a potential to be a source material of diogenites, while Neumann et al. (2014) regarded diogenites as crystallization products of the shallow magma ocean. However, homogeneous oxygen isotope compositions (e.g., Greenwood et al. 2014) and siderophile element depletions (e.g., Steenstra et al. 2016) in HED meteorites strongly suggest formation of a global magma ocean on Vesta. Furthermore, because of the uncertainty of the composition of the depleted deeper mantle formed in the shallow magma ocean model, the relationship between this model and the high ^{176}Hf/^{177}Hf ratio of the diogenites observed in this study is difficult to assess. Therefore, below, the discussion focuses on the partial melting of the Vestan mantle that crystallized from the planetary-scale magma ocean.

4.3.4.3. Timescale of mantle remelting and implications for its heat source

A heat source in the Vestan mantle is the unsolved issue of the mantle remelting scenario to produce diogenites by early differentiation of Vesta. To remelt the mantle, an additional heat source after the magma ocean solidification is necessary. A mantle overturn is one of possible processes to induce the remelting (e.g., Hublet et al., 2017). Below, the validity of a mantle overturn for the heat source of the remelting is investigated focusing on the timescale of the remelting.

It should be noted that the timescale between the crystallization and the remelting of the Vestan mantle can be estimated from the initial ^{176}Hf/^{177}Hf ratio of the diogenites presented in this study and the ^{176}Lu–^{176}Hf composition of CHUR (Bouvier et al., 2008). Focusing on the timescale of the mantle remelting, a general form of the radioactive decay of ^{176}Lu to ^{176}Hf can be written as:

$$\left(\frac{^{176}\mathrm{Hf}}{^{177}\mathrm{Hf}}\right)^{\mathrm{diogenite}}_{\mathrm{initial}} = \left(\frac{^{176}\mathrm{Hf}}{^{177}\mathrm{Hf}}\right)^{\mathrm{mantle}}_{\mathrm{initial}} + \left(\frac{^{176}\mathrm{Lu}}{^{177}\mathrm{Hf}}\right)^{\mathrm{mantle}} \left(e^{\lambda t} - 1\right). \quad (7)$$

The term "*t*" represents the timescale of the mantle remelting. $(^{176}Hf/^{177}Hf)^{diogenite}_{initial}$ and $(^{176}Hf/^{177}Hf)^{mantle}_{initial}$ are the initial $^{176}Hf/^{177}Hf$ ratios at the crystallization of diogenites and the Vestan mantle, respectively. $(^{176}Lu/^{177}Hf)^{mantle}$ represents the $^{176}Lu/^{177}Hf$ ratio of the Vestan mantle. Assuming that the initial $^{176}Hf/^{177}Hf$ ratio of the Vestan mantle is equal to the CHUR value at 4.6 Ga (Bouvier et al., 2008), the timescale "*t*" can be written as a function of $(^{176}Lu/^{177}Hf)^{mantle}$ by rearranging equation (7):

$$t = \frac{1}{\lambda}\ln\left[1 + \frac{(^{176}Hf/^{177}Hf)^{diogenite}_{initial} - (^{176}Hf/^{177}Hf)^{mantle}_{initial}}{(^{176}Lu/^{177}Hf)^{mantle}}\right]. \quad (8)$$

A black solid line in Figure 32 represents this Equation (8). The gray shaded zone shows the range of the experimentally obtained olivine/melt partitioning coefficients of Lu and Hf, which provide the reasonable estimation of the $(Lu/Hf)_n$ ratio of the Vestan mantle. Assuming that the $(Lu/Hf)_n$ ratio of the Vestan mantle reflects the olivine/melt partitioning coefficients of these elements (D_{Lu}/D_{Hf} = 4.35–35.5; Kennedy et al., 1993; Zanetti et al., 2004), the timescale between the crystallization and the remelting is estimated to be ~100–1000 Ma (corresponding to the interceptions of the black solid line with the end of the gray shaded zone in Figure 32). Considering the ^{176}Lu–^{176}Hf age of the diogenites given in this study (4.40 ± 0.38 Ga; Figure 24b) and the assumption of the Vestan mantle formation at 4.6 Ga, the timescale estimation should be revised to ~100–600 Ma.

This large timescale of remelting indicates later formation of diogenites, compared with the early formation of eucrites within up to ~10 Ma after CAI formation inferred from several short-lived chronometers (e.g., ^{26}Al–^{26}Mg, Hublet et al., 2017; ^{53}Mn–^{53}Cr, Trinquier et al., 2008; ^{60}Fe–^{60}Ni, Tang and Dauphas, 2012; ^{182}Hf–^{182}W, Touboul et al., 2015). The later formation of diogenites is consistent with the younger ^{87}Rb–^{87}Sr ages for two diogenites relative to those of eucrites reported by Takahashi and Masuda (1990) and the absence of resolvable decay products of a short-lived nuclide ^{26}Al in three diogenites reported by Hublet et al. (2017). However, in contrast to these observations, Trinquier et al. (2008) and Tang and Dauphas (2012) found that the ^{53}Mn–^{53}Cr and ^{60}Fe–^{60}Ni data of three diogenites define regression lines on isochron diagrams together with the eucrite data, suggesting simultaneous formation of these two meteorite classes. Furthermore, Schiller et al. (2011) observed a significant variation of ^{26}Mg abundances in diogenites and proposed the early crystallization of diogenites within ~4 Ma after CAI formation. Although, at present, the discrepancies among these diogenite ages are difficult to explain,

we consider that the fact that the number of diogenite samples used in this study is more than any other previous studies mentioned above (except for Schiller et al., 2011) ensures the reliability of this study. Anyway, further investigation of this problem is strongly required.

Considering the timescale of remelting (~100–600 Ma), the diogenites could not present at the timing of the hit-and-run collision (4525.39 ± 0.42/0.85 Ma; Haba et al., 2019), which formed mesosiderites. This is absolutely inconsistent with the formation of the howarditic Vestan surface by the hit-and-run collision (see 4.3.4.2. Trace element diversity of diogenites and partial melting of the Vestan mantle). This indicates either the formation of the howarditic Vestan surface by later impact events (i.e., not by hit-and-collision) or extreme incompatible element-depletion in the Vestan mantle. As described above, the timescale of remelting was calculated assuming that the Vestan mantle $(Lu/Hf)_n$ ratio is equal to the experimentally obtained olivine/melt D_{Lu}/D_{Hf} ratio. Therefore, if the Vestan mantle $(Lu/Hf)_n$ ratio is higher than the D_{Lu}/D_{Hf} ratio, the timescale can be smaller than the current estimation of ~100–600 Ma. Since there are no reliable estimations for the Vestan mantle $(Lu/Hf)_n$ ratios, further consideration about this problem is difficult at present.

The timescale of remelting (~100–600 Ma) is apparently inconsistent with the geophysical estimation of the timescale of the Vestan mantle overturn of ~1 Ma by Elkins-Tanton et al. (2008). The discrepancy in the timescales estimated from the two different models suggests that overturn is an unrealistic heat source for the Vestan mantle remelting. However, their approach of the estimation is based on the Rayleigh–Taylor instability, which requires viscosity, compositional density gradient, gravitational acceleration, and thickness of the solid state Vestan mantle. Because of the difficulty of the accurate determination of these physical quantities, their estimation involves significant uncertainty. Hence, the chronologically estimated timescale of the remelting does not necessarily conflict with a mantle overturn. For the detailed investigation of the validity of a mantle overturn for the heat source of the remelting, further understanding of the physical property of the Vestan mantle is required.

An intense impact is another possibility of the heat source of the Vestan mantle remelting. Some recent studies (e.g., Davison et al., 2010) propose that impact-heating may induced large-scale melting on asteroids. The occurrence of an early bombardment

on Vesta is well confirmed by the pioneering work of Bogard and Garrison (2003), who investigated ^{40}Ar–^{39}Ar ages of several types of HED samples and found a cluster of impact-reset ages within ~3.5–4.1 Ga, which is probably related to the lunar cataclysm. The observation of Bogard and Garrison (2003) is supported by numerous following studies (e.g., Marchi et al., 2013) and the impact-reset ages are recorded not only in whole-rock HED samples but also in various types of HED components like glass veins in an unequilibrated eucrites (Buchanan et al., 2005). Consistently, as discussed above, the disturbance of the ^{87}Rb–^{87}Sr systematics of the nine diogenites (Figure 26) is probably the record of frequent intense impacts on Vesta. Moreover, the presence of the giant impact basin Rheasilvia (~500 km diameter; Schenk et al., 2012) at the Vestan south pole is substantial evidence of the occurrence of intense impacts on Vesta. Considering the recent formation of the Rheasilvia (~1 Ga provided by a crater-counting approach; Schenk et al., 2012), an impact which formed the Rheasilvia itself is incapable to account for the heat source of the mantle remelting. However, the timing of intense impacts on Vesta (~3.5–4.1; Bogard and Garrison, 2003) slightly overlaps with the ^{176}Lu–^{176}Hf age of the diogenites given in this study (4.40 ± 0.38 Ga; Figure 24b). This slight overlap does not exclude the possibility of the formation of diogenites by impact-induced magmatism in the Vestan mantle.

Table 12. Trace element abundances (ppb) of nine diogenites determined by ICP-MS.

Sample	Bilanga			Johnstown			Tatahouine		
	WR	Residue	Leachate	WR	Residue	Leachate	WR	Residue	Leachate
Mass (g)[a]	0.1230	1.2397		0.7597	1.3085		0.4366	1.0306	
Rb	39.7 (2)	6.3 (2)	22.7 (11)	50.1 (6)	15.5 (5)	26.4 (6)	75 (2)	21.4 (7)	21.7 (6)
Sr	1105 (4)	153.5 (7)	130.1 (12)	1510 (10)	217 (2)	1970 (20)	218.6 (13)	52.3 (5)	177.7 (12)
La	41.0 (3)	306 (4)	1440 (10)	119 (2)	35.2 (12)	89 (2)	34.8 (6)	10.82 (10)	8.4 (4)
Ce	106.3 (10)	690 (30)	3480 (30)	290.4 (14)	162.3 (13)	171 (2)	82.4 (7)	21.50 (10)	22.1 (4)
Pr	16.1 (2)	86.6 (10)	498 (5)	41.2 (8)	31.6 (5)	22.2 (5)	8.5 (2)	2.31 (8)	2.3 (2)
Nd	88.5 (7)	359 (3)	2187 (9)	200.7 (8)	194 (2)	87 (2)	32.9 (8)	8.3 (5)	9.68 (14)
Sm	39.6 (4)	80.9 (9)	435 (3)	67.8 (4)	87.1 (15)	18.0 (2)	6.8 (3)	3.6 (2)	2.05 (6)
Eu	14.4 (5)	3.36 (8)	4.29 (4)	19.4 (2)	6.1 (4)	19.28 (6)	1.56 (8)	0.66 (4)	0.66 (5)
Gd	68.5 (7)	98.7 (6)	367 (2)	103.9 (8)	148 (2)	21.1 (3)	11.0 (3)	9.8 (6)	2.08 (9)
Tb	14.5 (4)	16.9 (5)	41.2 (3)	20.4 (2)	30.4 (2)	3.2 (2)	2.53 (10)	3.1 (5)	0.32 (2)
Dy	111.2 (14)	122.1 (14)	182.0 (13)	159.6 (7)	236 (2)	22.0 (5)	25.1 (3)	35.0 (8)	2.05 (2)
Ho	27.4 (5)	28.4 (6)	27.0 (3)	40.2 (10)	57.2 (4)	5.1 (2)	7.6 (3)	11.1 (6)	0.48 (3)
Er	94.2 (3)	93.2 (5)	56.2 (3)	135.3 (7)	195 (2)	15.6 (2)	31.9 (5)	49.2 (6)	1.73 (9)
Tm	15.1 (4)	15.2 (5)	5.8 (3)	22.7 (8)	31.2 (5)	2.53 (10)	6.5 (3)	10.3 (2)	0.30 (8)
Yb	114.4 (7)	108.9 (7)	27.9 (2)	170.0 (3)	237 (2)	17.3 (3)	57.5 (7)	93.5 (7)	2.34 (6)
Lu	18.49 (11)	16.0 (4)	3.7 (2)	26.0 (3)	35.3 (4)	2.7 (2)	10.2 (3)	16.6 (8)	0.380 (8)
Hf	53.8 (2)	34.2 (9)	1.12 (5)	45.7 (5)	80.3 (10)	0.660 (11)	6.6 (3)	11.89 (7)	0.134 (14)
$(La/Lu)_n$[b]	0.230 (2)	1.98 (4)	40.8 (4)	0.476 (10)	0.103 (4)	3.48 (9)	0.354 (7)	0.0674 (6)	2.28 (11)
$(La/Sm)_n$[b]	0.649 (8)	2.37 (4)	2.08 (2)	1.10 (2)	0.253 (10)	3.10 (9)	3.2 (2)	1.89 (9)	2.56 (14)
$(Dy/Lu)_n$[b]	0.602 (8)	0.76 (2)	5.0 (3)	0.615 (7)	0.671 (10)	0.83 (5)	0.247 (8)	0.211 (11)	0.541 (13)
$(Lu/Hf)_n$[b]	1.472 (10)	2.01 (7)	14.0 (10)	2.43 (3)	1.88 (3)	17.2 (11)	6.6 (4)	6.0 (3)	12.2 (13)
Ce/Ce*[c]	0.991 (12)	1.01 (5)	0.983 (10)	0.99 (2)	1.17 (2)	0.92 (2)	1.15 (2)	1.03 (5)	1.21 (6)
Eu/Eu*[c]	0.84 (3)	0.114 (3)	0.0326 (4)	0.702 (8)	0.162 (10)	3.00 (3)	0.55 (3)	0.34 (3)	0.97 (8)

Notes. Figures in parentheses show standard errors in 2σ. For residue and leachate, figures represent the weight proportions of elements in each fraction to the sample powder used for the acid-leaching experiment.

[a]Mass of sample powder used for the experiment.

[b]These elemental ratios are normalized by CI chondrite composition (Anders and Grevesse, 1989).

[c]$Ce/Ce^* = Ce_n/(La_n \times Pr_n)^{1/2}$ and $Eu/Eu^* = Eu_n/(Sm_n \times Gd_n)^{1/2}$ where La_n, Ce_n, Pr_n, Sm_n, Eu_n, and Gd_n are concentrations of these elements normalized by CI chondrite composition (Anders and Grevesse, 1989).

(continued)

Sample	Hamara			LMT 042			NWA 5480		
	WR	Residue	Leachate	WR	Residue	Leachate	WR	Residue	Leachate
Mass (g)[a]	0.5529	1.1171		0.2309	0.9652		0.1639	1.2595	
Rb	135 (7)	76 (3)	63.1 (6)	1045 (13)	375 (9)	379 (4)	8.6 (4)	5.4 (4)	4.7 (3)
Sr	2621.2 (9)	420 (10)	3530 (10)	23400 (500)	1480 (30)	19830 (110)	308 (3)	83 (2)	340.2 (13)
La	44.3 (6)	30.4 (6)	42.2 (7)	549 (2)	232.0 (14)	371 (2)	5.3 (2)	4.5 (2)	3.3 (2)
Ce	93.3 (9)	67.1 (15)	102.6 (7)	1292 (6)	695.6 (10)	844 (5)	14.95 (11)	11.24 (3)	7.6 (4)
Pr	12.4 (5)	8.0 (2)	12.8 (3)	188 (2)	118.3 (2)	129.9 (12)	1.84 (4)	1.47 (3)	1.02 (3)
Nd	58.6 (8)	33.7 (12)	57.8 (13)	945.0 (6)	662.0 (7)	577 (2)	7.9 (8)	7.2 (3)	4.4 (3)
Sm	17.3 (3)	11.0 (2)	17.5 (3)	330 (3)	278.2 (12)	152.1 (11)	3.94 (8)	3.3 (2)	1.32 (5)
Eu	4.6 (2)	2.74 (11)	7.75 (13)	106.6 (4)	28.28 (14)	153.0 (6)	0.68 (7)	0.67 (9)	0.61 (5)
Gd	26.0 (9)	19.3 (5)	16.8 (3)	408.9 (10)	449 (5)	173.3 (10)	9.9 (4)	11.50 (11)	1.1 (2)
Tb	4.63 (10)	4.5 (2)	2.40 (13)	73.5 (9)	87.8 (13)	26.0 (3)	3.12 (11)	3.8 (2)	0.19 (2)
Dy	37.6 (6)	40.7 (6)	13.9 (3)	512 (2)	638 (2)	168.0 (14)	33.7 (4)	40.6 (7)	1.20 (4)
Ho	9.7 (3)	11.4 (2)	2.73 (8)	118 (2)	148 (2)	35.3 (3)	10.8 (4)	11.9 (4)	0.28 (5)
Er	33.8 (8)	42.9 (8)	7.4 (4)	367 (3)	472 (2)	105.8 (8)	44.7 (6)	51.2 (8)	1.08 (3)
Tm	5.73 (9)	7.8 (2)	0.93 (9)	56.0 (7)	73 (2)	15.37 (9)	8.71 (11)	9.9 (3)	0.22 (7)
Yb	45.2 (4)	66.3 (2)	6.4 (2)	389 (2)	518.6 (13)	98.5 (9)	75.0 (3)	84.9 (4)	1.69 (7)
Lu	7.3 (2)	10.19 (11)	0.93 (8)	57.6 (5)	69.2 (15)	14.6 (5)	13.15 (12)	13.9 (2)	0.32 (6)
Hf	8.4 (4)	13.9 (2)	0.17 (7)	148 (3)	317 (2)	2.24 (10)	6.8 (3)	4.2 (2)	0.076 (14)
$(La/Lu)_n$[b]	0.630 (12)	0.309 (6)	4.71 (11)	0.986 (11)	0.347 (3)	2.63 (2)	0.042 (2)	0.0337 (14)	1.08 (6)
$(La/Sm)_n$[b]	1.61 (4)	1.74 (4)	1.51 (3)	1.043 (10)	0.523 (4)	1.529 (15)	0.85 (4)	0.85 (5)	1.58 (10)
$(Dy/Lu)_n$[b]	0.52 (2)	0.400 (8)	1.50 (14)	0.890 (9)	0.92 (2)	1.15 (4)	0.257 (4)	0.293 (7)	0.38 (7)
$(Lu/Hf)_n$[b]	3.7 (2)	3.15 (5)	23 (9)	1.67 (3)	0.93 (2)	27.9 (15)	8.3 (3)	14.2 (6)	18 (5)
Ce/Ce*[c]	0.96 (2)	1.03 (3)	1.06 (2)	0.965 (6)	1.007 (3)	0.922 (7)	1.14 (3)	1.05 (3)	1.00 (6)
Eu/Eu*[c]	0.66 (3)	0.57 (3)	1.37 (3)	0.882 (5)	0.243 (2)	2.86 (2)	0.33 (4)	0.33 (5)	1.6 (2)

(continued)

Sample	Y 74013			Y 74097			Y 002875		
	WR	Residue	Leachate	WR	Residue	Leachate	WR	Residue	Leachate
Mass (g)[a]	0.3494	1.0125		0.4551	1.0612		0.3380	1.0190	
Rb	4.04 (3)	1.3 (3)	0.325 (12)	1.71 (15)	1.16 (11)	0.35 (12)	11.0 (5)	7.2 (5)	4.7 (5)
Sr	209 (2)	135 (2)	361 (5)	322 (2)	101.3 (12)	32.4 (7)	163 (2)	133 (3)	40.5 (10)
La	8.2 (3)	6.0 (5)	3.0 (2)	8.1 (5)	6.9 (2)	1.56 (11)	12.8 (5)	8.1 (3)	3.97 (12)
Ce	29.0 (3)	22.4 (5)	5.8 (5)	25.2 (8)	21.6 (5)	3.18 (2)	38.4 (10)	26.3 (6)	10.19 (8)
Pr	4.6 (2)	4.19 (8)	0.64 (10)	3.8 (3)	4.0 (3)	0.38 (8)	6.3 (4)	5.03 (5)	0.96 (13)
Nd	26.1 (8)	26.2 (2)	2.8 (2)	22.7 (6)	23.2 (7)	1.5 (2)	40.1 (8)	36.1 (7)	4.6 (3)
Sm	11.3 (2)	13.3 (3)	0.55 (3)	11.6 (2)	10.7 (3)	0.33 (7)	23.5 (9)	22.2 (2)	1.5 (2)
Eu	3.38 (2)	3.2 (3)	2.98 (7)	4.58 (4)	2.9 (2)	0.39 (4)	4.0 (2)	3.79 (11)	0.34 (6)
Gd	21.4 (6)	25.5 (6)	0.71 (9)	22.1 (3)	21.2 (9)	0.62 (7)	57.3 (8)	50.6 (10)	2.59 (8)
Tb	4.88 (13)	6.08 (13)	0.12 (3)	4.91 (12)	4.8 (2)	0.15 (4)	13.8 (6)	12.8 (4)	0.55 (6)
Dy	43.9 (7)	52.2 (6)	1.21 (4)	47.2 (10)	48.1 (7)	1.06 (5)	120.3 (13)	112.1 (11)	4.2 (2)
Ho	12.0 (3)	14.8 (2)	0.35 (2)	13.3 (3)	14.0 (3)	0.32 (8)	34 (2)	31.4 (10)	1.08 (9)
Er	47.9 (7)	58.2 (4)	1.00 (4)	52.0 (5)	56.3 (10)	1.00 (5)	126.7 (14)	116.9 (3)	3.46 (9)
Tm	8.9 (5)	10.9 (4)	0.19 (5)	9.9 (5)	10.7 (2)	0.17 (7)	23.0 (4)	21.1 (6)	0.54 (2)
Yb	74.9 (12)	91.4 (7)	1.63 (9)	82.2 (6)	93.6 (13)	1.49 (5)	187 (2)	173.7 (10)	4.33 (11)
Lu	12.5 (3)	15.4 (2)	0.28 (4)	13.7 (5)	15.2 (4)	0.22 (4)	27.9 (9)	27.0 (5)	0.70 (9)
Hf	11.3 (4)	23.08 (11)	0.32 (5)	11.7 (2)	12.9 (3)	0.04 (4)	30.0 (3)	30.1 (4)	0.04 (4)
$(La/Lu)_n$[b]	0.068 (2)	0.041 (3)	1.08 (8)	0.061 (4)	0.0473 (12)	0.73 (6)	0.048 (2)	0.0309 (10)	0.59 (2)
$(La/Sm)_n$[b]	0.46 (2)	0.28 (2)	3.4 (3)	0.44 (3)	0.40 (2)	3.0 (6)	0.34 (2)	0.227 (8)	1.6 (2)
$(Dy/Lu)_n$[b]	0.351 (11)	0.340 (6)	0.43 (6)	0.344 (14)	0.318 (11)	0.48 (9)	0.432 (15)	0.416 (9)	0.60 (8)
$(Lu/Hf)_n$[b]	4.8 (2)	2.85 (4)	3.8 (8)	5.0 (2)	5.0 (2)	20 (20)	3.98 (14)	3.84 (9)	70 (60)
Ce/Ce*[c]	1.13 (3)	1.07 (5)	1.01 (12)	1.09 (7)	0.98 (5)	0.99 (11)	1.03 (5)	0.99 (3)	1.26 (9)
Eu/Eu*[c]	0.66 (2)	0.53 (5)	14.4 (13)	0.869 (13)	0.59 (5)	2.6 (4)	0.33 (2)	0.344 (12)	0.52 (9)

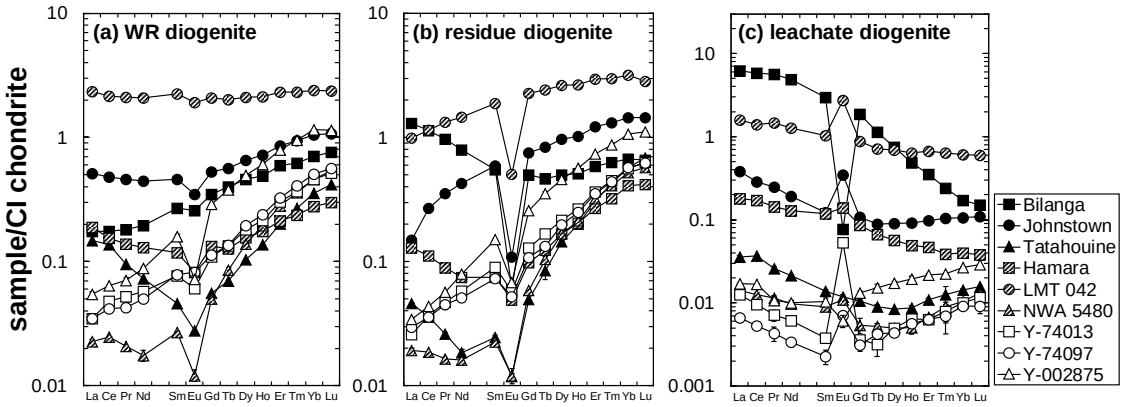

Figure 20. REE patterns of (a) WR, (b) residue, and (c) leachate fractions of nine diogenites. The CI chondrite compositions for the normalization are from Anders and Grevesse (1989). For the leachates and residues, the vertical axis shows the proportion of weight of elements in each fraction to the bulk weight of sample powder used for the HCl-leaching experiment. The error bars display standard errors of individual experiments in 2σ.

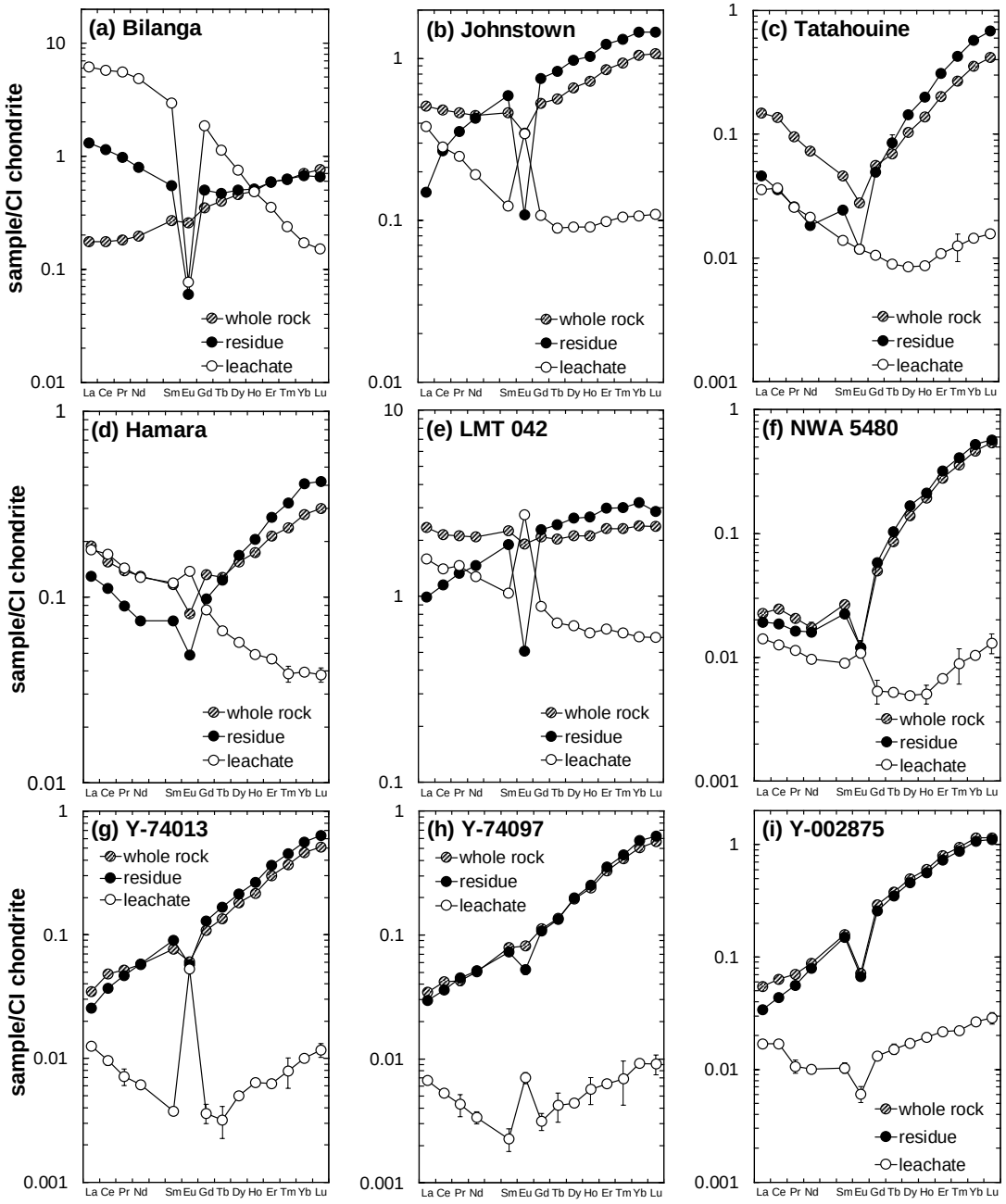

Figure 21. Comparison of REE patterns between WR, residue, and leachate fractions of nine diogenites. The CI chondrite compositions for the normalization are from Anders and Grevesse (1989). For the leachates and residues, the vertical axis shows the proportion of weight of elements in each fraction to the bulk weight of sample powder used for the HCl-leaching experiment. The error bars display standard errors of individual experiments in 2σ.

Table 13. Trace element abundances (ppm) of leachate fractions of nine diogenites relative to its dry weight.

Sample	Bilanga	Johnstown	Tatahouine	Hamara	LMT 042	NWA 5480	Y 74013	Y 74097	Y 002875
Rb	0.55 (3)	0.619 (14)	0.442 (12)	1.440 (14)	2.83 (3)	0.028 (2)	0.0059 (2)	0.008 (3)	0.15 (2)
Sr	3.16 (3)	46.1 (4)	3.63 (2)	80.4 (3)	148.1 (8)	2.035 (8)	6.58 (8)	0.72 (2)	1.30 (3)
La	35.0 (3)	2.09 (5)	0.171 (8)	0.96 (2)	2.77 (2)	0.0199 (10)	0.054 (4)	0.035 (2)	0.128 (4)
Ce	84.3 (7)	4.01 (4)	0.451 (7)	2.34 (2)	6.31 (4)	0.046 (2)	0.106 (9)	0.0708 (5)	0.328 (3)
Pr	12.07 (11)	0.520 (12)	0.047 (4)	0.293 (7)	0.971 (9)	0.0061 (2)	0.012 (2)	0.009 (2)	0.031 (4)
Nd	53.1 (2)	2.03 (5)	0.198 (3)	1.32 (3)	4.312 (13)	0.026 (2)	0.051 (4)	0.034 (4)	0.146 (10)
Sm	10.55 (6)	0.422 (5)	0.0418 (13)	0.399 (6)	1.137 (8)	0.0079 (3)	0.0101 (5)	0.007 (2)	0.049 (5)
Eu	0.1040 (11)	0.4513 (13)	0.0134 (10)	0.177 (3)	1.143 (4)	0.0036 (3)	0.0544 (14)	0.0087 (9)	0.011 (2)
Gd	8.90 (5)	0.494 (7)	0.042 (2)	0.383 (10)	1.295 (8)	0.0063 (13)	0.013 (2)	0.014 (2)	0.083 (3)
Tb	1.001 (7)	0.076 (5)	0.0066 (4)	0.055 (3)	0.194 (2)	0.00114 (9)	0.0021 (6)	0.0034 (9)	0.018 (2)
Dy	4.42 (3)	0.515 (12)	0.0419 (5)	0.316 (6)	1.255 (11)	0.0072 (3)	0.0221 (7)	0.0236 (11)	0.135 (7)
Ho	0.655 (8)	0.119 (4)	0.0098 (6)	0.062 (2)	0.264 (3)	0.0017 (3)	0.0065 (4)	0.007 (2)	0.035 (3)
Er	1.364 (7)	0.365 (5)	0.035 (2)	0.169 (9)	0.790 (6)	0.0064 (2)	0.0183 (6)	0.0222 (11)	0.111 (3)
Tm	0.140 (8)	0.053 (2)	0.006 (2)	0.021 (2)	0.1148 (7)	0.0013 (4)	0.0035 (10)	0.0037 (14)	0.0173 (6)
Yb	0.677 (4)	0.404 (7)	0.0477 (13)	0.147 (4)	0.736 (7)	0.0101 (4)	0.030 (2)	0.0331 (12)	0.139 (4)
Lu	0.089 (5)	0.062 (4)	0.0078 (2)	0.021 (2)	0.109 (4)	0.0019 (3)	0.0052 (6)	0.0049 (9)	0.022 (3)
Hf	0.0273 (12)	0.0154 (3)	0.0027 (3)	0.004 (2)	0.0167 (7)	0.00046 (8)	0.0059 (10)	0.0009 (8)	0.0014 (12)

Notes. Figures represent the weight proportions of elements in leachate fraction to its dry weight. Figures in parentheses show standard errors in 2σ.

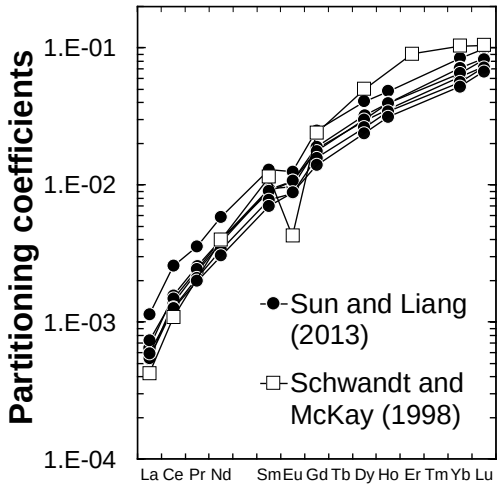

Figure 22. Experimentally obtained orthopyroxene/melt partitioning coefficients of REE. Data are from Schwandt and McKay (1998) and Sun and Liang (2013).

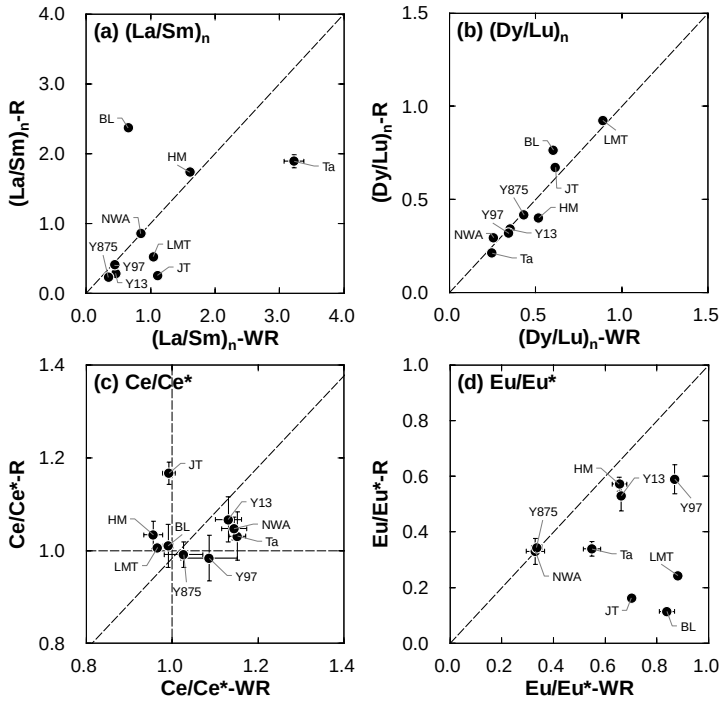

Figure 23. Comparison of (a) $(La/Sm)_n$, (b) $(Dy/Lu)_n$, (c) Ce/Ce*, and (d) Eu/Eu* ratios between WR and leachate fractions of nine diogenites. The horizontal axis shows elemental ratios of WR fractions, while the vertical axis shows those of residues. Abbreviations of meteorite names are listed in Table 7. The error bars display standard errors of individual experiments in 2σ.

Table 14. ^{87}Rb–^{87}Sr and ^{176}Lu–^{176}Hf isotopic compositions of nine diogenites.

Sample	$^{87}Rb/^{86}Sr$[a]	$^{87}Sr/^{86}Sr$[b]	$^{176}Lu/^{177}Hf$[a]	$^{176}Hf/^{177}Hf$[c]
WR				
Bilanga	0.104 (5)	0.70262 (2)	0.0491(3)	0.2856 (7)
Johnstown	0.0959 (12)	0.701941 (8)	0.0810 (12)	0.28701 (10)
Tatahouine	1.00 (3)	0.712611 (9)	0.220 (12)	0.296 (2)
Hamara	0.149 (8)	0.709066 (9)	0.123 (7)	0.2935 (9)
LMT 042	0.129 (3)	0.708465 (7)	0.0556 (11)	0.28438 (7)
NWA 5480	0.081 (4)	0.7227 (14)	0.277 (11)	0.2965 (12)
Y 74013	0.0560 (7)	0.70178 (6)	0.159 (7)	0.2961 (9)
Y 74097	0.0154 (13)	0.70022 (3)	0.167 (6)	0.2960 (6)
Y 002875	0.195 (9)	0.707533 (10)	0.133 (5)	0.2931 (3)
Residue				
Bilanga	0.119 (4)	0.703850 (8)	0.067 (2)	0.28773 (12)
Johnstown	0.207 (6)	0.704674 (7)	0.0627 (10)	0.28631 (2)
Tatahouine	1.19 (4)	0.724216 (9)	0.200 (9)	0.3009 (2)
Hamara	0.53 (2)	0.709906 (7)	0.105 (2)	0.2911 (4)
LMT 042	0.73 (2)	0.704776 (8)	0.0311 (7)	0.283591 (11)
NWA 5480	0.19 (2)	0.711946 (9)	0.47 (2)	0.3211 (4)
Y 74013	0.028 (7)	0.701050 (10)	0.0950 (14)	0.29066 (8)
Y 74097	0.033 (3)	0.701241 (10)	0.167 (6)	0.2964 (2)
Y 002875	0.158 (11)	0.706611 (8)	0.128 (3)	0.29327 (10)
Leachate				
Bilanga	0.50 (2)	0.720114 (9)	0.47 (3)	0.287 (4)
Johnstown	0.0388 (9)	0.700765 (8)	0.57 (4)	0.288 (2)
Tatahouine	0.353 (10)	0.709674 (7)	0.41 (4)	0.292 (4)
Hamara	0.0517 (5)	0.709350 (7)	0.8 (3)	0.2824 (4)
LMT 042	0.0553 (7)	0.705597 (7)	0.93 (5)	0.2845 (10)
NWA 5480	0.040 (2)	0.712090 (9)	0.60 (15)	0.285 (4)
Y 74013	0.00261 (10)	0.699208 (7)	0.13 (3)	0.28 (2)
Y 74097	0.031 (11)	0.700440 (11)	0.8 (7)	0.283 (14)
Y 002875	0.33 (4)	0.711106 (13)	2 (2)	0.28 (3)
Standard				
NIST SRM 987	—	0.710248 (2)[d]	—	—
JMC 475	—	—	—	0.281876 (7)

Notes. Figures in parenthesis show standard errors in 2σ.
[a]Elemental ratios are determined using ICP-MS.
[b]Isotopic ratios of $^{87}Sr/^{86}Sr$ are determined using TIMS.
[c]Isotopic ratios of $^{176}Hf/^{177}Hf$ are determined using MC-ICP-MS.
[d]An average and standard deviation (2σ) of repeat analyses (11 times) are shown.

Table 15. Model ^{87}Rb–^{87}Sr impact ages of six recent-fall and Antarctic-find diogenites.

Sample	Age (Ma)[a]	Initial $^{87}Sr/^{86}Sr$[a]	MSWD
Bilanga	2970 ± 1600[b]	0.6984 ± 0.0052[b]	16
Johnstown	1626 ± 950[b]	0.6998 ± 0.0017[b]	29
Tatahouine	991 ± 9200[b]	0.70 ± 0.12[b]	1074
Y 74013 and Y 74097	3305 ± 1500[b]	0.69933 ± 0.00073[b]	40
Y 002875	1757 ± 360[c]	0.70261 ± 0.00099[c]	0.047

Notes. [a]Standard errors (2σ) are shown.
[b]Model-3 solution (McIntyre et al., 1966) by Isoplot program (Ludwing, 2012).
[c]Model-1 solution (McIntyre et al., 1966) by Isoplot program (Ludwing, 2012).

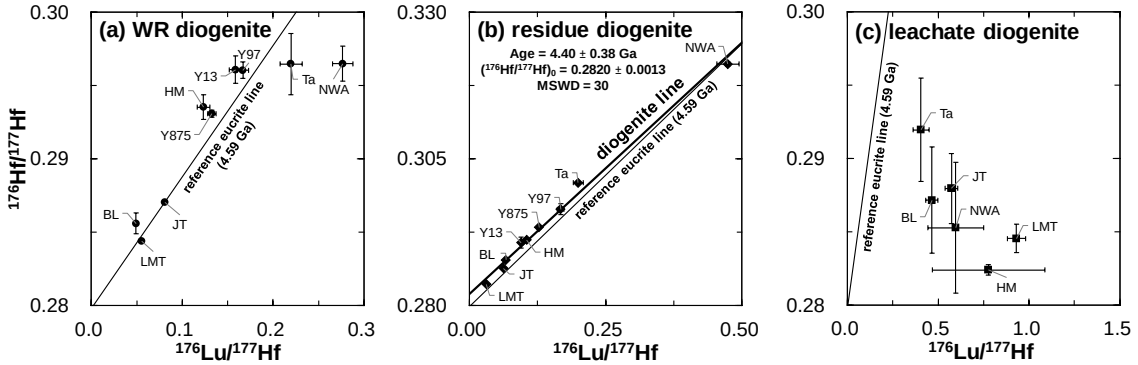

Figure 24. External ^{176}Lu–^{176}Hf isochron diagrams for (a) WR, (b) residue, and (c) leachate fractions of nine diogenites. Abbreviations of meteorite names are listed in Table 7. The error bars display standard errors of individual experiments in 2σ. The reference eucrite line (dashed line) is from Bouvier et al. (2015). The isotope data of the leachate fractions of the three Antarctic diogenites (Y 74013, Y 74097, and Y 002875) are not shown in the diagram due to large analytical error. The ^{176}Lu–^{176}Hf data set of the residue fractions define the ^{176}Lu–^{176}Hf age of 4.40 ± 0.38 Ga (2σ) and the initial ratio of 0.2820 ± 0.0013 (2σ) for the nine diogenites. The WRs and leachates do not define any regression meaningful regression lines on the isochron diagrams.

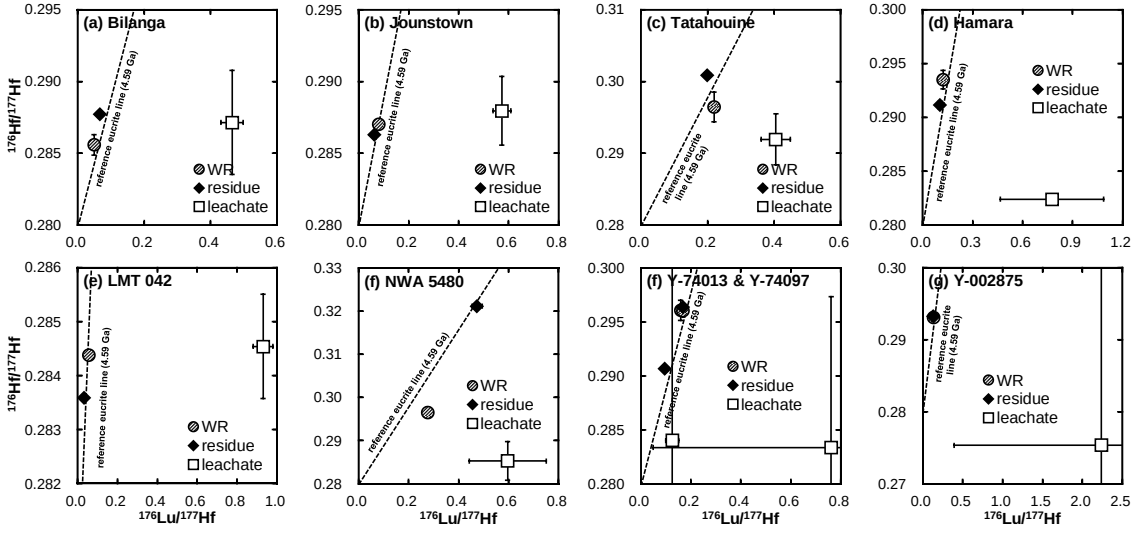

Figure 25. Internal ^{176}Lu–^{176}Hf isochron diagrams for nine diogenites. The error bars display standard errors of individual experiments in 2σ. The reference eucrite line (dashed line) is from Bouvier et al. (2015). Isotope data of two paired diogenites of Y 74013 and Y 74097 are plotted together in single isochron diagram (f).

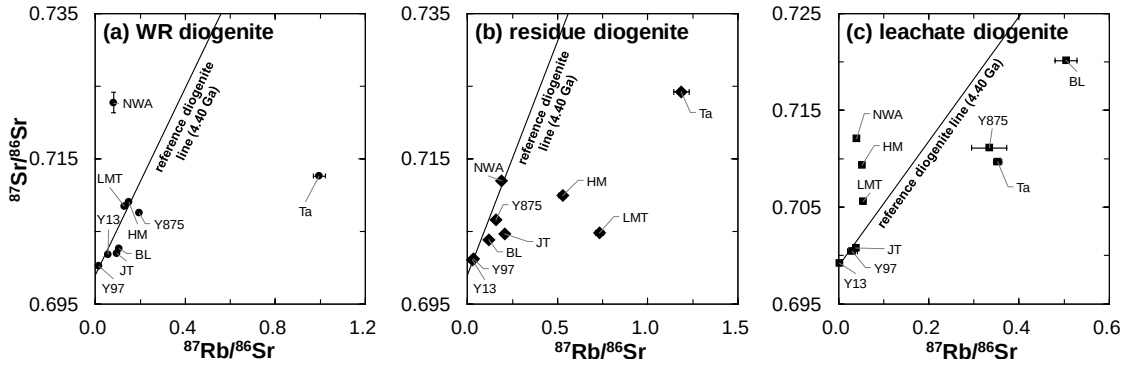

Figure 26. External ^{87}Rb–^{87}Sr isochron diagrams for (a) WR, (b) residue, and (c) leachate fractions of nine diogenites. Abbreviations of meteorite names are listed in Table 7. The error bars display standard errors of individual experiments in 2σ. The reference diogenite line (dashed line) is from Takahashi and Masuda (1990). None of the three fractions of the nine diogenites define any regression lines on the isochron diagrams.

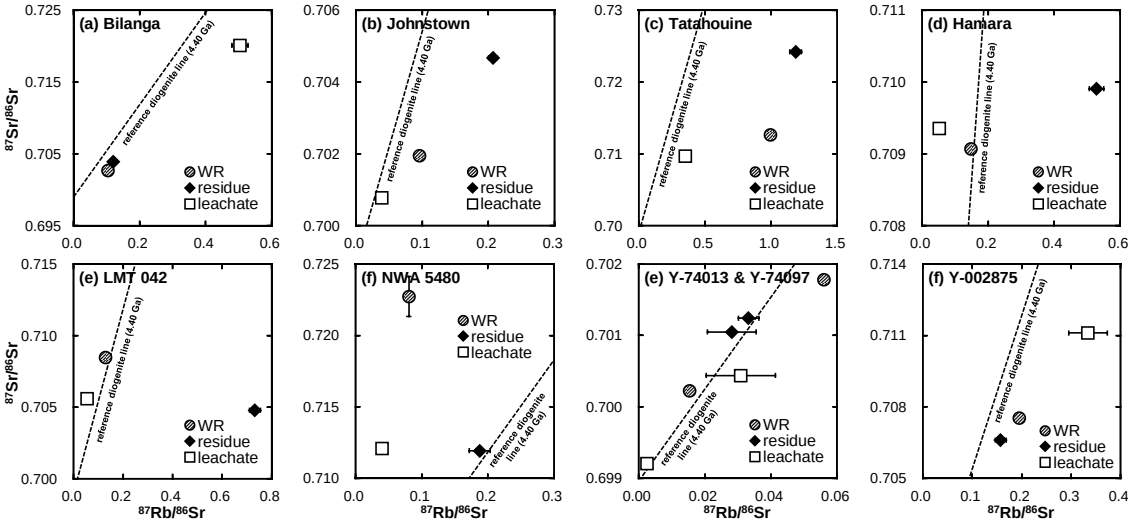

Figure 27. Internal ^{87}Rb–^{87}Sr isochron diagrams for nine diogenites. The error bars display standard errors of individual experiments in 2σ. The reference diogenite line (dashed line) is from Takahashi and Masuda (1990). Isotope data of two paired diogenites of Y 74013 and Y 74097 are plotted together in single isochron diagram (f).

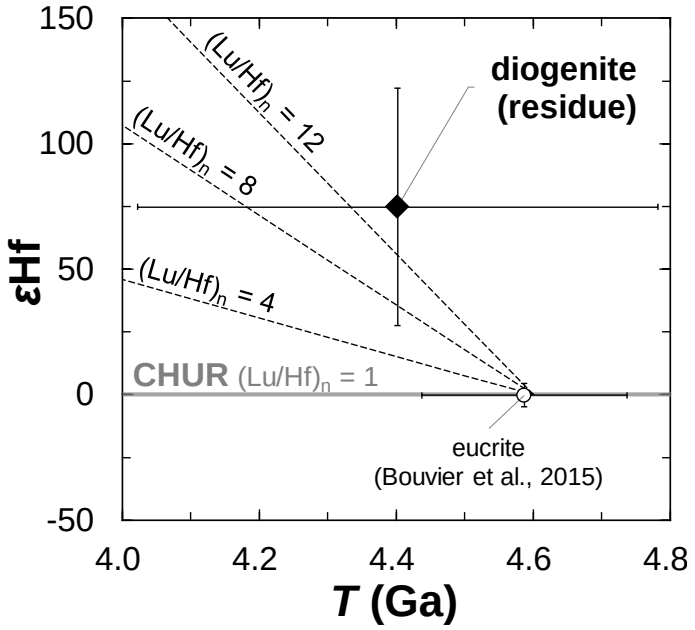

Figure 28. Hf isotope evolution diagram for eucrites and diogenites. The horizontal axis represents ^{176}Lu–^{176}Hf ages and the vertical axis shows fractional deviations of ^{176}Hf/^{177}Hf ratios from CHUR (Bouvier et al., 2008). The definition of εHf is described in Equation (4). The gray line shows the εHf value of CHUR (=0). The black diamond and white circle represent the ^{176}Lu–^{176}Hf ages and initial ^{176}Hf/^{177}Hf ratios of the nine diogenites (this study) and eucrites (Bouvier et al., 2015), respectively. The error bars show 2σ errs. The dashed lines display the εHf evolutions of model reservoirs that differentiated from CHUR at 4.6 Ga with individually different $(Lu/Hf)_n$ ratios.

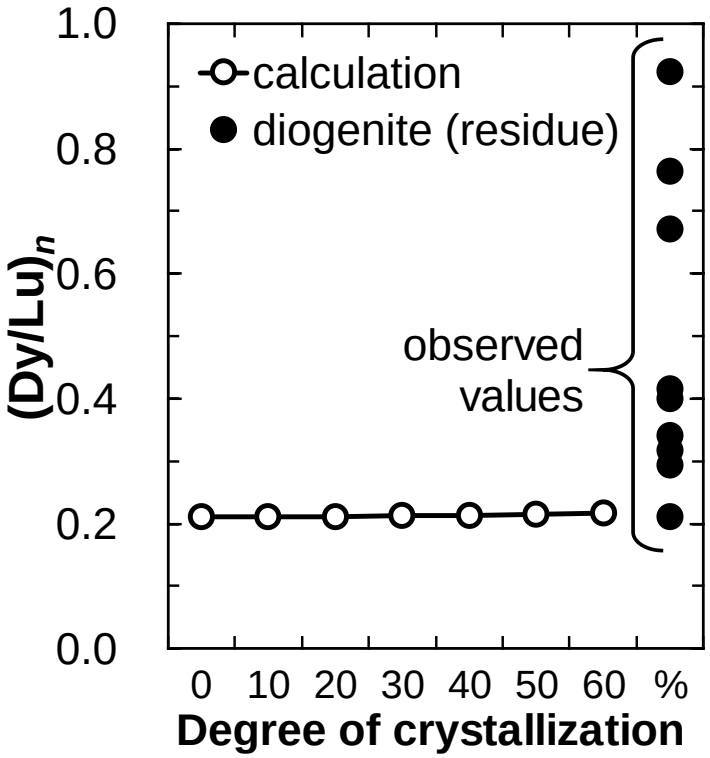

Figure 29. $(Dy/Lu)_n$ variation of orthopyroxene produced by fractional crystallization of single melt. The horizontal axis represents a weight fraction of pyroxene that crystallize from the melt (i.e., value of *f* in Equation (5)). The white circles show the $(Dy/Lu)_n$ ratios of crystallizing pyroxenes calculated by Equation (5) and the black ones show the $(Dy/Lu)_n$ ratios of the residues of the nine diogenites measured in this study.

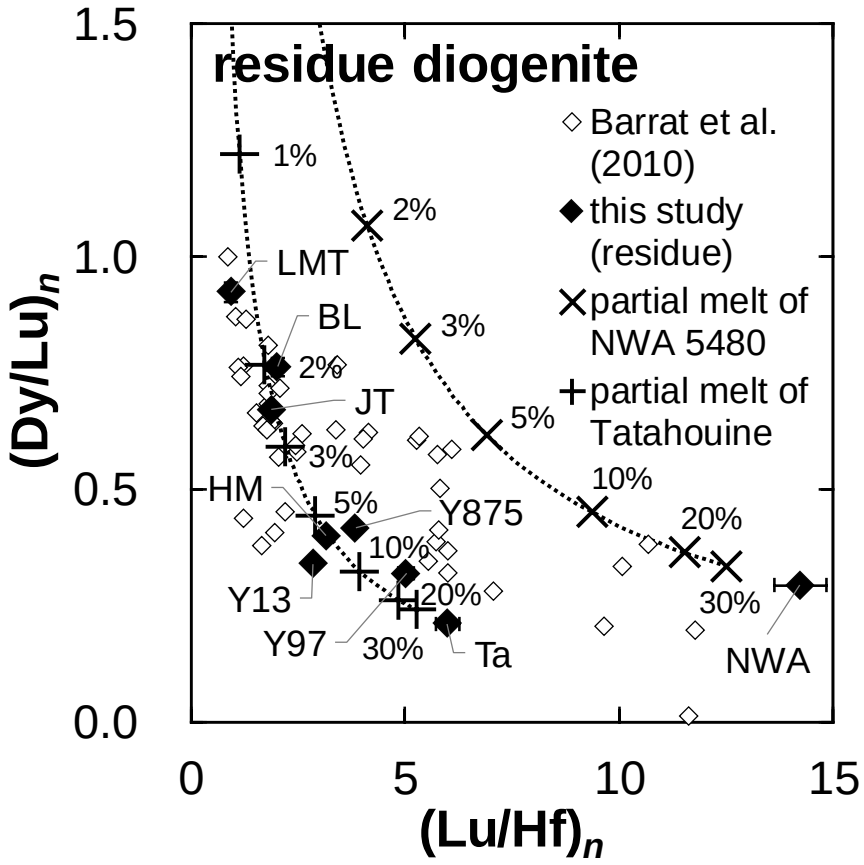

Figure 30. Compositional variation of partial melt of Tatahouine and NWA 5480 diogenites. The black diamonds display the compositions of the residues of the nine diogenites measured in this study, and the white ones display reference acid-washed diogenite data (Barrat et al., 2010). The types of black crosses show the compositional variations of equilibrated partial melts of the Tatahouine and NWA 5480 diogenites calculated by Equation (6) (a left trend is for Tatahouine and a right one is for NWA 5480). The percentages found nearby the black crosses represent the values of *f* in Equation (6) (i.e., degrees of partial melting). Abbreviations of meteorite names are listed in Table 7.

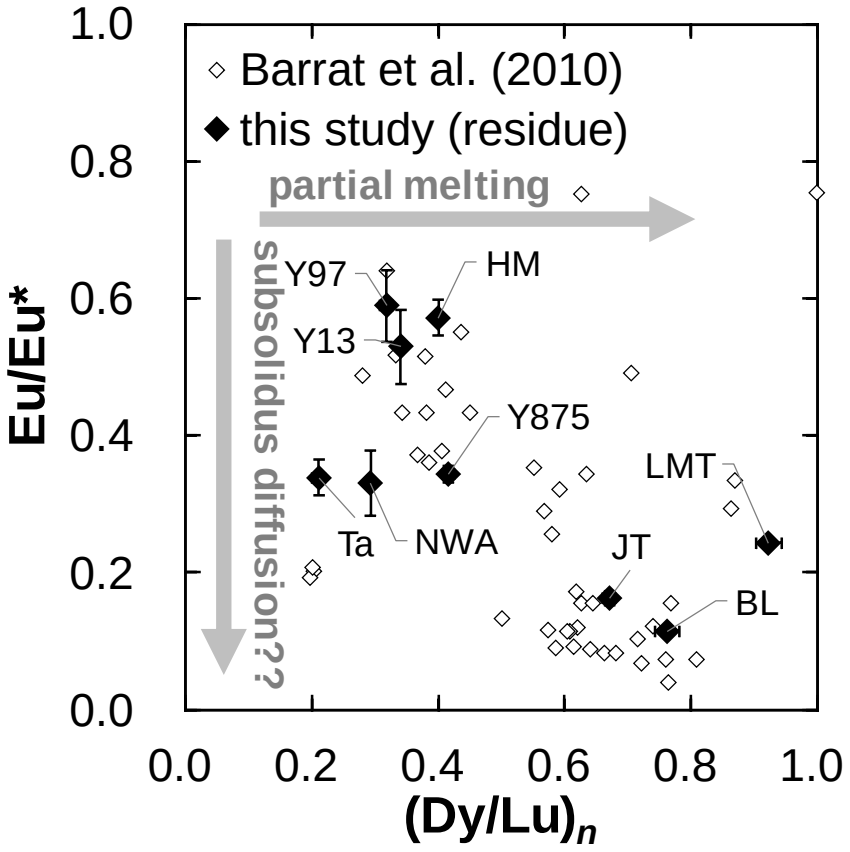

Figure 31. Correlation diagram for $(Dy/Lu)_n$ and Eu/Eu* of diogenites. Abbreviations of meteorite names are listed in Table 7. The black diamonds display the compositions of the residue fractions of the nine diogenites measured in this study, while the white ones show those of acid-washed diogenite samples of Barrat et al. (2010). The error bars represent standard errors (2σ).

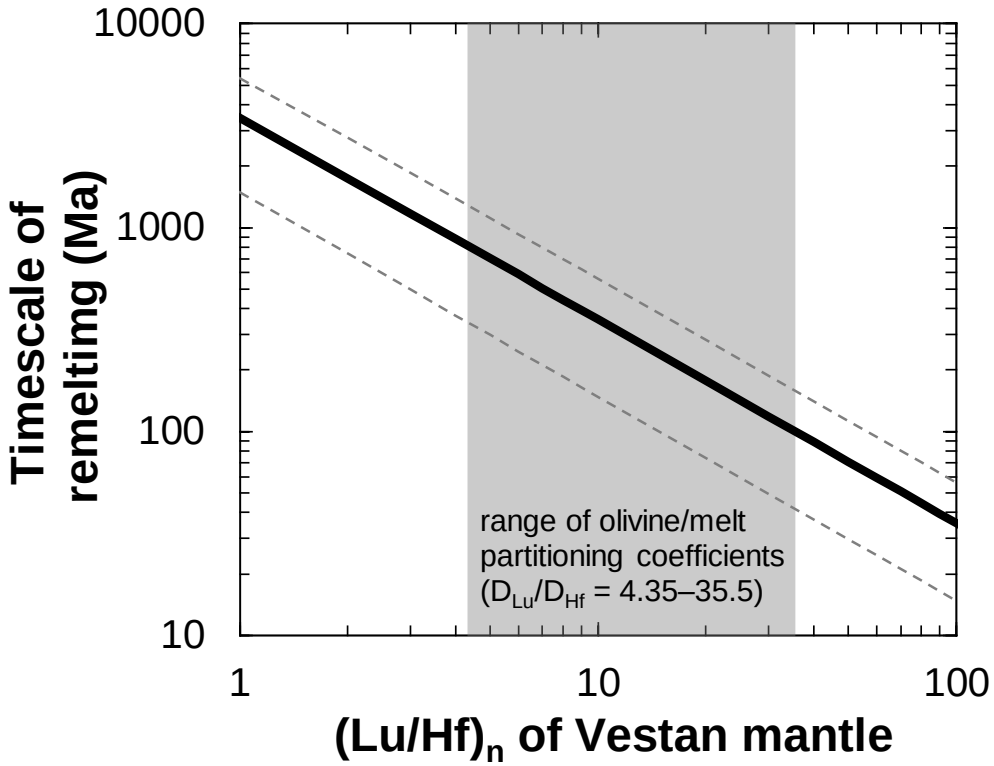

Figure 32. Relationship between $(Lu/Hf)_n$ ratio of Vestan mantle and timescale of its remelting. The horizontal axis shows $(Lu/Hf)_n$ ratios of the Vestan mantle. The vertical axis shows the timescale between the crystallization and remelting of the Vestan mantle. The black line represents the relationship between the $(Lu/Hf)_n$ ratio and timescale calculated by Equation (8). The dashed gray lines display 95% confidence interval of the calculated values, corresponding to the standard error (2σ) of the initial $^{176}Hf/^{177}Hf$ ratio of the nine diogenites given in this study. The gray dashed zone represents the rang of the published olivine/melt partitioning coefficients of Lu and Hf (Kennedy et al., 1993; Zanetti et al., 2004).

4.4. Summary

The isotopic data set of the ^{176}Lu–^{176}Hf decay system from the residues of the nine diogenites defines a meaningful regression line on the isochron diagram (Figure 24b). The ^{176}Lu–^{176}Hf age of 4.40 ± 0.38 Ga and the initial $^{176}Hf/^{177}Hf$ ratio of 0.2820 ± 0.0013 obtained from the regression line indicate that the source material of diogenites differentiated at the early stage of Vesta and shows a high $(Lu/Hf)_n$ ratio (>8). The Vestan mantle is consistent with these characteristics. The significant disturbance of the ^{87}Rb–^{87}Sr systematics of the nine diogenites suggests the occurrence of multiple intense impacts on Vesta. The variation of trace element abundances of the nine diogenites suggests their differentiation from compositionally diverse multiple parental melts. Based on these observations, we propose the crystallization of diogenites from the partial melts of the Vestan mantle in the following history.

1. Vesta was formed by the accretion of planetesimals at an early stage of the solar system. The radioactive decay heat by short-lived nuclides (^{26}Al and probably ^{60}Fe) induced the formation of a planetary-scale magma ocean and the segregation of a metallic core on Vesta.
2. Following the cooling of the magma ocean, an olivine-rich mantle characterized by superchondritic Lu/Hf ratio was firstly crystallized. Subsequently to the crystallization of olivine and orthopyroxene, eucrites were formed as basaltic upper crust.
3. After ~100–600 Ma from the solidification of the mantle, an additional heat source (overturn, impact, or other processes) induced partial melting of the Vestan mantle. The partial melts show the variation of REE compositions depending on the degree of melting. Diogenites crystallized from these melts with the superchondritic initial $^{176}Hf/^{177}Hf$ ratio of 0.2820 ± 0.0013 due to the high Lu/Hf ratio of the Vestan mantle.
4. After the crystallization, the diogenites suffered multiple intense impacts on Vesta, and their ^{87}Rb–^{87}Sr systematics were disturbed significantly. Some of the impacts ejected diogenitic clasts from the surface of Vesta and delivered them to near-Earth orbit.

5. Neutron capture effects in eucrites

5.1. Introduction

Cosmic-ray exposure (CRE) ages determined by abundances of cosmogenic nuclides are unique aspects of histories of meteorites that cannot be investigated by other geochemical approaches. During the transitions of meteoroids from parent bodies to the Earth, spallation reactions induced by galactic cosmic-ray irradiations produce cosmogenic nuclides having half-life of 10^5–10^6 years (e.g., ^{10}Be, ^{26}Al, ^{37}Cl, and ^{53}Mn), which never present in non-irradiated environment. Thus, for recent-fall meteorites, the length of the transition time of meteoroids (i.e., CRE ages) can be estimated from the abundances of these nuclides. Eugster and Michel (1994) investigated cosmogenic nuclides of noble gases in HED meteorites and revealed the presence of two major of their CRE ages at 21 and 38 Ma and other three break-up events at 6, 12, and 73 Ma. Then, eucrite samples that belongs to the same CRE age cluster can be presumed to have been located in close or the same regions in their parent body. The presence of the multiple CRE age clusters guarantees that HED meteorites in our collection represent multiple regions of their parent body.

Another approach to investigate CRE histories of meteorites is based on neutron capture reactions of stable isotopes. The interaction of cosmic rays with planetary material produces neutrons, which are captured by the nuclei of surrounding elements in the material. As a consequence of this reaction, nuclei having especially large thermal neutron-capture cross sections (e.g., ^{149}Sm and $^{155, 157}$Gd) show significant variations in isotopic composition even in natural environments. Thus, the CRE history of planetary materials can be investigated from the isotopic compositions of some specific elements like Sm and Gd. For deriving the CRE history of planetary materials, neutron-capture reactions of the (n,γ)-type, whose daughter nuclides show low radioactivities and small neutron-capture cross sections, are useful because the records of neutron-capture reactions can be derived quantitively from the isotopic variations between the deficit of parent and excess of daughter nuclides. As typical examples of the (n,γ)-type neutron-capture reactions, it is well known that significant isotopic shifts of ^{149}Sm–^{150}Sm and ^{157}Gd–^{158}Gd have often been found in extraterrestrial materials like meteorites and lunar

surface soils (e.g., Lugmair et al., 1971; Hidaka et al., 1999; 2007; 2017) because ^{149}Sm and ^{157}Gd have very large thermal neutron-capture cross sections. Because the two nuclides have slightly different resonance energies for thermal neutron capture, 0.0973 eV for ^{149}Sm and 0.0314 eV for ^{157}Gd, a combination of the isotopic shifts between ^{149}Sm–^{150}Sm and ^{157}Gd–^{158}Gd provides information on the energy distribution of thermalized neutrons. The first attempts at this approach were successfully applied to lunar regolith samples recovered in the Apollo mission (Lugmair et al., 1971; Burnett et al., 1972; Russ, 1972; Russ et al., 1973). These studies demonstrated that the lunar regolith shows large isotopic shifts of Sm and Gd because of long-time irradiation on the lunar surface (this type of irradiation is called 2π-irradiation). Furthermore, recent studies (e.g., Nishiizumi et al., 1996; Hidaka et al., 2017; 2022) showed that most lunar meteorites also experienced long-time 2π-irradiation on the lunar surface, whereas the contributions of cosmic-ray irradiation in space (this type of irradiation is called 4π-irradiation) are limited due to their short transition from the Moon to the Earth (<1 Ma). Other than lunar samples, Sm and Gd isotopic shifts of aubrite meteorites were also investigated (Hidaka et al., 1999; 2012). Because aubrites are characterized by a long transition period from the parent body to the Earth (>10 Ma; Lorenzetti et al., 2003; Miura et al., 2007), they might experience significantly long exposure times to 4π-irradiation in space.

Contrary to cosmogenic nuclides, which provide precise CRE records of recent <100 Ma, (n,γ) shifts of stable isotopes preserve whole CRE records of planetary materials owing to their stabilities. Although 4π-irradiation records of eucrites in space is well established by previous studies (e.g., Eugster & Mitchel, 1994; Miura et al., 1998), 2π-irradiation on their parent body could not discussed due to the lack of the data of (n,γ) shifts of stable isotopes. In this study, (n,γ) isotopic shifts of Sm and Gd of eucrites are measured to investigate their CRE record in detail, especially focusing to the possibility of 2π-irradiation of eucrites.

5.2. Experiments

5.2.1. Samples

Eight basaltic eucrites, Dar al Gani (DaG) 380, DaG 391, DaG 411, DaG 443, DaG 480, Juvinas, Millibillillie, and Stannern, were used in this study. The DaG series meteorites were found in the Libyan Desert, and were weakly shocked: DaG 380 is a monomict, whereas DaG 391, DaG 411, and DaG 443 are polymict (Grossman, 1999; Grossman and Zipfel, 2001). The other three eucrites, Juvinas, Millibillillie, and Stannern, are well known as basaltic eucrites and have often been used in chronological and geochemical studies to further understanding of the early evolution processes of the solar planetary materials (e.g., Bouvier et al., 2015; Bermingham et al., 2016; Brennecka and Kleine, 2017).

As standard reference materials without cosmic-ray irradiation, chemical reagents of Sm and Gd (1000 mg L^{-1} of single-element standard solutions for the inductively coupled plasma mass spectrometer (ICP–MS) and ICP atomic emission spectroscopy analyses commercially obtained from SPEX CertiPrep) were used for the determination of their isotopic ratios.

5.2.2. Chemical treatment

Each sample, weighing 0.3 to 0.4 g, was powdered and then decomposed completely by HF–$HClO_4$ with heating. After evaporation to dryness, the residue was redissolved in 5 mL of 2 M HCl. This sample solution was divided into two portions: the main portion, over 90% of the total solution, was for isotopic measurements of Sm and Gd using a TIMS, and the minor portion was for the determination of elemental abundances of rare earth elements (REEs) using ICP–MS.

For the isotopic study, the major portion of each sample solution was loaded onto a cation exchange resin-packed column (Bio-Rad AG50WX8, 200–400 mesh, H^+ form, 50 mm length × 4.0 mm diameter). The column was washed with 1.7 M HCl for the elution of major elements and then washed with 6 M HCl for REE elution. The REE fraction was evaporated to dryness, redissolved in a drop of 0.25 M HCl, and loaded onto a column packed with LN-resin (Eichrom, LN-resin, particle size of 20–50 μm, 100 mm length × 2.5 mm diameter). The column was washed with 0.25 M HCl. Then, Sm and Gd were

eluted with 0.35 M and 0.5 M HCl, respectively. The details of the chemical procedures for the REE mutual separation are given in Mizutani et al. (2020).

The minor portion of each sample solution was evaporated to dryness and redissolved using 5 mL of 2% HNO_3. A 0.01 g quantity of a 1 ppb mixture solution of indium and bismuth was added to the sample solution as an internal standard to optimize the analytical conditions for the determination of the elemental abundances of the REEs. An Agilent 7500cx ICP–MS instrument was used for the analyses.

5.2.3. Mass spectrometry

Isotopic analyses of Sm and Gd for individual samples were performed using a TIMS (Triton Plus) at the National Museum of Nature and Science in Tsukuba, Japan. Sm and Gd were measured on double Re filaments without any activators. $^{147}Sm/^{152}Sm = 0.56031$ and $(^{155}Gd + {}^{156}Gd)/^{160}Gd = 1.61290$ were used as the normalization factors for the correction of instrumental mass fractionation of Sm and Gd isotopic ratios, respectively (Hidaka et al., 1995; Hidaka and Yoneda, 2007; 2014). All analyses were performed in static mode with the amplifier rotation system. The detailed analytical protocols for the Sm and Gd isotopic measurements were described in previous studies (e.g., Hidaka and Yoneda, 2014).

5.3. Results and Discussion

5.3.1. REE abundances

Figure 33 shows CI chondrite-normalized REE abundance patterns of eucrite samples measured in this study. All eight eucrites exhibit REE abundances similar to Stannern-trend eucrites. Judging from the pronounced negative Eu anomalies and heavy REE depletions (i.e., $(Dy/Lu)_n < 1$) of DaG 391 and Stannern, these two can be classified as Stannern-trend eucrites, whereas the other six can be classified as MG–NL-trend eucrites. High incompatible element abundances of Stannern-trend eucrites are interpreted as a consequence of contamination of Main Group eucritic magmas by melts derived by partial melting of the asteroid's crust. Millibillillie has a positive Eu anomaly (Eu/Eu* = 1.2), whereas other eucrites show negative Eu anomalies (Eu/Eu* = 0.7–0.9). These data are almost the same as those in typical basaltic eucrites shown by previous studies (Consolmagno and Drake, 1977; Makishima and Masuda, 1993; Barrat et al., 2000; Yamaguchi et al., 2009).

It is reported that terrestrial weathering also causes significant REE mobilization of meteorites. The REE patterns of some Antarctic eucrites show positive or negative Ce anomalies (Floss and Crozaz, 1991; Mittlefehldt and Lindstrom, 1991). These REE abundance variations are interpreted as being caused by the dissolution of phosphates, which are important REE carriers in water equilibrated with the atmosphere (Mittlefehldt and Lindstrom, 1991), and the fractionation of Ce from the other +3 charged REE due to oxidization of Ce to the +4 state. Cold desert weathering can also cause similar REE disturbance in meteorites (Shimizu et al., 1984; Floss and Crozaz, 1991; Mittlefehldt and Lindstrom, 1991), but the state in the hot desert is more complex than the situation of Antarctic weathering. Many secondary minerals filling cracks, such as carbonates and sulfates, were found in hot desert samples (Barrat et al., 2003; Lee and Bland, 2004). However, among those meteorites, light-REE-poor samples have light-REE enrichment patterns, and significant REE mobilization has not been detected in Saharan eucrites, which are rich in REE abundances, except for one eucrite (NWA 047) showing obvious light-REE enrichment (Barrat et al., 2003). As shown in Figure 33, the samples used in this study also display no REE mobilization, suggesting no clear traces of cold or hot desert weathering on REE abundances.

5.3.2. Sm and Gd isotopic shifts

The Sm and Gd isotope ratios of the eight eucrites measured using TIMS are listed in Table 16. The data show clear isotopic deficits in ^{149}Sm and ^{157}Gd and excesses in ^{150}Sm and ^{158}Gd for seven of the eight eucrites, excepting DaG 443. Because the neutron-capture reaction of ^{149}Sm(n,γ)^{150}Sm produces ^{150}Sm from the equivalent number of ^{149}Sm, the isotopic decrement of ^{149}Sm quantitatively corresponds to the isotopic increment of ^{150}Sm. Thus, if Sm isotope composition is affected predominantly by this reaction, Sm isotope data points yield a linear trend with slope –1 in the ^{150}Sm/^{152}Sm–^{149}Sm/^{152}Sm three-isotope diagram. Similarly, if a Gd isotope is affected by a neutron-capture reaction of ^{157}Gd(n,γ)^{158}Gd, Gd isotope data yield the same trend on the ^{157}Gd/^{160}Sm–^{158}Gd/^{160}Gd three-isotope diagram. The correlation diagrams between ^{149}Sm/^{152}Sm and ^{150}Sm/^{152}Sm and between ^{157}Gd/^{160}Gd and ^{158}Gd/^{160}Gd for the occurrence of neutron-capture reactions are shown in Figure 34, respectively. Except for DaG 443, all seven eucrites measured in this study show significant isotopic shifts of Sm and Gd from those of terrestrial standard materials (STD). As shown in Figure 34, the Sm and Gd isotope data of these eucrites are consistent with the straight lines with slope –1 drawn from STD compositions, which represent isotopic shifts caused by the neutron-capture reactions. These trends strongly suggest that the Sm and Gd isotope shifts of these eucrites are caused by neutron-capture effects associated with exposure to cosmic rays. The fluence of neutrons generated by cosmic-ray irradiation can be quantified by the following equation based on previous studies (e.g., Hidaka et al., 1995; 2012),

$$\Psi_{\mathrm{sample}} = \frac{\left(^{150}\mathrm{Sm}/^{149}\mathrm{Sm}\right)_{\mathrm{sample}} - \left(^{150}\mathrm{Sm}/^{149}\mathrm{Sm}\right)_{\mathrm{STD}}}{\left(^{150}\mathrm{Sm}/^{149}\mathrm{Sm}\right)_{\mathrm{STD2}} - \left(^{150}\mathrm{Sm}/^{149}\mathrm{Sm}\right)_{\mathrm{STD}}} \times \frac{\Sigma_{\mathrm{sample}}}{\Sigma_{\mathrm{STD2}}} \times \Psi_{\mathrm{STD2}},$$

where Ψ and Σ represent neutron fluences and effective total macroscopic neutron-capture cross sections, respectively. STD2 is a standard material that is experimentally irradiated by thermal neutrons of 5.94×10^{15} n cm^{-2} in a laboratory (Hidaka et al., 1995), and STD is a standard material that represents the natural composition of Sm isotopes without irradiation. Comparisons between Sm isotopic shifts of meteorite samples and experimentally irradiated material provide estimates of neutron fluence. According to this equation, the neutron fluences of eucrite samples measured in this study are calculated as (0.28–2.38) $\times 10^{15}$ n cm^{-2} (see Table 17), which are 10 to 10^2 times lower than those of

lunar regolith and aubrites (>10^{16} n cm^{-2}; e.g., Hidaka and Yoneda, 2007; Hidaka et al., 2010; 2012).

Figure 35 shows a comparison between neutron fluences measured in this study and CRE ages measured by Miura et al. (1998). In general, these two quantities are proportionally correlated because they are proportional to amounts of certain nuclides that are produced by cosmic-ray irradiation. However, some meteorite samples do not show such a linear correlation due to the inconsistency between the neutron fluences and the CRE ages because of complicated rather than simple CRE processes. Neutron fluences estimated from a stable nuclide like ^{150}Sm record the whole CRE history of meteorites after their formation as a part of the parent body. By contrast, the CRE ages, estimated from a short-lived nuclide like ^{81}Kr with a half-life of 0.23 Ma, record the CRE duration of recent–100 Ma (mainly after the ejection from the parent body). Hence, if meteorite samples experienced irradiation on the surface of their parent body earlier than recent–100 Ma before ejection, they show high neutron fluences relative to their CRE ages. This is often the case for lunar meteorites (e.g., Hidaka et al., 2017). As shown in Figure 35, three fall-eucrites measured in this study, Juvinas, Millibillillie, and Stannern, show a positive correlation between their neutron fluences and CRE ages, with no excesses of their neutron fluences. This suggests that neutron-capture reactions in these three eucrites occurred predominantly by 4π-irradiation during their transport from the parent body to the Earth, and that 2π-irradiation at the surface of their parent body is negligible. A slight deficit of the neutron fluence found in Juvinas is probably due to the different samples used for the estimation of neutron fluences in this study and CRE age in a previous study. Considering that the recovered mass of Juvinas was over 90 kg (*Meteoritical Bulletin Database*), many Juvinas fragments were originally located in various depths of the large meteoroidal body in space. The Juvinas sample used in this study may have been located at a deeper part of the whole Juvinas meteorite relative to that used for determining the CRE age (Miura et al., 1998**)** during 4π-irradiation. Assuming that the four desert-found eucrites (DaG 380, DaG 391, DaG 411, and DaG 480; DaG 443 was excluded because of its low neutron fluence) are exposed to the same flux of neutrons as the three fall-eucrites, their CRE ages can be estimated using linear regression of neutron fluences and CRE ages of the three fall-eucrites. The estimated CRE ages of the desert-found eucrites are also shown in Figure 35 together with those of the three fall-eucrites measured by Miura

et al. (1998). The gray bars in the figure display the CRE age clusters of eucrites reported by Miura et al. (1998). As shown in Figure 35, the estimated CRE ages of DaG 391, DaG 411, and DaG 380 can be attributed to the previously reported age clusters, whereas DaG 480 has an apparently greater CRE age than these age clusters. This indicates that DaG 480 was ejected from the parent body by an impact event that differs from other studied eucrites, or that DaG 480 experienced additional irradiation on the surface of the parent body.

5.3.3. Constraints on the cosmic-ray irradiation condition from the isotopic variations of Sm and Gd in eucrites

The energy of neutrons generated by cosmic-ray irradiation depends on the temperature, size, and composition of the irradiated target material (e.g., Spergel et al., 1986). In this study, the energy distribution of neutron fluence in the thermal region ($E <$ 0.1 eV) in eucrites is investigated from the combination of the Sm and Gd isotopic shifts. Using the difference of the neutron-capture resonance energies between ^{149}Sm and ^{157}Gd, 0.0973 eV and 0.0314 eV, respectively, a comparison of the magnitudes between ^{149}Sm–^{150}Sm and ^{157}Gd–^{158}Gd isotopic shifts provides information on the neutron energy profile in a thermal region. For the quantitative assessment of the neutron energy profile in individual eucrites, an index $\varepsilon_{Sm}/\varepsilon_{Gd}$ given by Russ et al. (1971) is defined as follows:

$$\frac{\varepsilon_{\mathrm{Sm}}}{\varepsilon_{\mathrm{Gd}}} = \frac{\dfrac{\left(^{150}\mathrm{Sm}/^{149}\mathrm{Sm}\right)_{\mathrm{sample}} - \left(^{150}\mathrm{Sm}/^{149}\mathrm{Sm}\right)_{\mathrm{STD}}}{1 + \left(^{150}\mathrm{Sm}/^{149}\mathrm{Sm}\right)_{\mathrm{sample}}}}{\dfrac{\left(^{158}\mathrm{Gd}/^{157}\mathrm{Gd}\right)_{\mathrm{sample}} - \left(^{158}\mathrm{Gd}/^{157}\mathrm{Gd}\right)_{\mathrm{STD}}}{1 + \left(^{158}\mathrm{Gd}/^{157}\mathrm{Gd}\right)_{\mathrm{sample}}}}.$$

As listed in Table 17, the seven eucrites measured in this study (DaG 443 is excluded because of its low neutron fluence) have similar $\varepsilon_{Sm}/\varepsilon_{Gd}$ values (0.61–0.81), which are identical within the 2σ error range. This indicates that these eucrites experienced almost identical irradiation conditions, predominantly 4π-irradiation in space, as discussed in Section 3.2. Hence, the $\varepsilon_{Sm}/\varepsilon_{Gd}$ ratios of the eucrites measured in this study can be interpreted to represent the neutron energy distribution generated by the 4π-irradiation. Although the $\varepsilon_{Sm}/\varepsilon_{Gd}$ values of the eucrites are identical within the 2σ error range, it should be noted that DaG 480 shows a slightly higher $\varepsilon_{Sm}/\varepsilon_{Gd}$ value (0.81) than those of

the six other eucrites (0.61–0.67). Interestingly, DaG 480 also shows the highest neutron fluences among the seven eucrites (Figure 35), suggesting that DaG 480 might have experienced another irradiation period in addition to the simple 4π-irradiation. One of the hypothetical ideas is that DaG 480 experienced 2π-irradiation on the surface of the parent body. Assuming that this idea is correct, the difference of $\varepsilon_{Sm}/\varepsilon_{Gd}$ values between DaG 480 and the six other eucrites may be interpreted as the difference in the energy distribution of neutrons generated by 2π- and 4π-irradiation, implying that 4π-irradiation produces more thermalized neutrons than does 2π-irradiation.

For a better understanding of the CRE conditions of the eucrites, their $\varepsilon_{Sm}/\varepsilon_{Gd}$ ratios are compared with those of lunar samples (Hidaka et al., 1999; 2000; Hidaka and Yoneda, 2007). The $\varepsilon_{Sm}/\varepsilon_{Gd}$ ratios of different types of meteorites cannot be compared simply because it is considered that the parameter $\varepsilon_{Sm}/\varepsilon_{Gd}$ depends on the chemical composition of the target materials. In this study, for characterizing the chemical compositions of meteorite samples from the perspective of their influence on the energy distribution of neutrons, an effective macroscopic neutron-capture cross section Σ_{eff}, which is generally used for an index of chemical composition, is defined as follows:

$$\Sigma_{\mathrm{eff}} = \sum_{i} \sigma_i \times A_i,$$

where i represents individual nuclides, and σ_i and A_i are neutron-capture cross sections and atomic abundances of the nuclide i, respectively. Figure 36 is a correlation diagram between Σ_{eff} and $\varepsilon_{Sm}/\varepsilon_{Gd}$ for the individual meteorite samples. In the figure, dashed lines are theoretical prediction lines of $\varepsilon_{Sm}/\varepsilon_{Gd}$ along with Σ_{eff} at two different temperatures, 0 and 400 K, given by Lingenfelter et al. (1972). Two data sets from eucrites and lunar samples are clearly distinguished in the figure because there is a clear difference in their individual Σ_{eff} values (0.0085–0.011 for A-12, -16, and -17 lunar-regolith samples, 0.004–0.005 for A-15 lunar-regolith samples, and 0.0065–0.007 for eucrites). The data points of eucrites measured in this study, together with those of lunar samples, are plotted between the two theoretical prediction lines in the figure. This indicates that the irradiation conditions of individual meteorites in the figure are roughly similar to each other. It is difficult to present a statistically critical discussion on the irradiation conditions of individual eucrites only from the $\varepsilon_{Sm}/\varepsilon_{Gd}$ values because of their large analytical uncertainties. However, the irradiation conditions of eucrites measured in this study seem

to show more thermalized effects than those of most lunar samples. The data points of eucrites are plotted close to the lower line showing the temperature of 400 K, whereas most of the data points of lunar samples are plotted relatively close to the upper line (0 K) in the figure. This implies that neutrons in eucrites generated by cosmic rays were well thermalized compared with those in the lunar samples. Because 2π-irradiation is dominant for the lunar samples, whereas 4π-irradiation is dominant for the eucrites, the difference in neutron energy between the eucrites and lunar samples may reflect this difference in the irradiation condition, implying that 4π-irradiation produces more thermalized neutrons than does 2π-irradiation. Interestingly, the discrepancy of $\varepsilon_{Sm}/\varepsilon_{Gd}$ ratios among the eucrites (discussed above) also implies the same interpretation. Both the comparisons of the Sm and Gd isotopic shifts among the eucrite samples and between eucrites and lunar samples consistently imply that 4π-irradiation produces thermalized neutrons. However, considering the influence of target size on neutron energy, it is well known that larger targets can produce better-thermalized neutrons than can smaller targets (e.g., Spergel et al., 1986). Then, the thermalized neutrons make the $\varepsilon_{Sm}/\varepsilon_{Gd}$ value low. In other words, the higher the contribution of 2π-irradiation, the lower the value of $\varepsilon_{Sm}/\varepsilon_{Gd}$. Our results from the isotopic shifts of Sm and Gd for eucrites are inconsistent with the common sense for the mechanism of neutron production induced by cosmic-ray irradiation. Although DaG 480 seems to show a slightly higher $\varepsilon_{Sm}/\varepsilon_{Gd}$ value than do the other eucrites, the precision of the $\varepsilon_{Sm}/\varepsilon_{Gd}$ values for eucrites is not sufficient to distinguish the difference between individual eucritic species. By contrast, the isotopic shifts of Sm and Gd for most lunar samples are tens to hundreds of times larger than those for eucrites. As a result, the precision of the isotopic variations of Sm and Gd of lunar samples is sufficient to discuss the thermalization degree from the $\varepsilon_{Sm}/\varepsilon_{d}$ value. Then, the model of Lingenfelter et al. (1972) is generally known to provide a lower trend of the $\varepsilon_{Sm}/\varepsilon_{d}$ value relative to the experimental data (e.g., Russ et al., 1971; 1972; Sands et al., 2001). However, in the case of eucrites, in the current analytical situation, it should be concluded that there is no clear evidence for the pre-irradiation record of DaG 480 before ejection from the parent body.

Table 16. Sm and Gd isotopic compositions

(a) Sm isotopic data normalized to $^{147}Sm/^{152}Sm=0.56081$

	$^{144}Sm/^{152}Sm$	$^{148}Sm/^{152}Sm$	$^{149}Sm/^{152}Sm$	$^{150}Sm/^{152}Sm$	$^{154}Sm/^{152}Sm$
Juvinas	0.114951 ± 3	0.420467 ± 2	0.516832 ± 3	0.276012 ± 2	0.850786 ± 4
Millbillillie	0.114972 ± 3	0.420437 ± 3	0.516782 ± 3	0.276060 ± 2	0.850781 ± 4
Stannern	0.114960 ± 1	0.420467 ± 1	0.516743 ± 1	0.276112 ± 1	0.850769 ± 5
DaG 380	0.114968 ± 1	0.420452 ± 1	0.516771 ± 1	0.276074 ± 1	0.850799 ± 2
DaG 391	0.114968 ± 1	0.420450 ± 1	0.516742 ± 1	0.276110 ± 1	0.850769 ± 4
DaG 411	0.114965 ± 3	0.420444 ± 3	0.516805 ± 3	0.276040 ± 2	0.850765 ± 4
DaG 443	0.114968 ± 1	0.420436 ± 2	0.516843 ± 2	0.276000 ± 1	0.850781 ± 4
DaG 480	0.114969 ± 1	0.420438 ± 1	0.516693 ± 2	0.276161 ± 2	0.850781 ± 4
STD (n=10)	0.114972 ± 2	0.420415 ± 6	0.516852 ± 7	0.275994 ± 4	0.850796 ± 15

(b) Gd isotopic data normalized to $(^{155}Gd+^{156}Gd)/^{160}Gd=1.61290$

	$^{152}Gd/^{160}Gd$	$^{154}Gd/^{160}Gd$	$^{157}Gd/^{160}Gd$	$^{158}Gd/^{160}Gd$
Juvinas	0.0092588 ± 18	0.0996951 ± 15	0.715827 ± 7	1.135882 ± 8
Millbillillie	0.0092592 ± 14	0.0996945 ± 11	0.715705 ± 12	1.135987 ± 13
Stannern	0.0092586 ± 10	0.0996947 ± 9	0.715610 ± 24	1.136071 ± 26
DaG 380	0.0092580 ± 18	0.0996948 ± 15	0.715686 ± 32	1.136025 ± 28
DaG 391	0.0092589 ± 12	0.0996947 ± 11	0.715604 ± 37	1.136079 ± 24
DaG 411	0.0092590 ± 15	0.0996950 ± 11	0.715767 ± 31	1.135942 ± 29
DaG 443	0.0092588 ± 18	0.0996951 ± 15	0.715855 ± 23	1.135857 ± 33
DaG 480	0.0092590 ± 15	0.0996950 ± 11	0.715554 ± 29	1.136119 ± 34
STD (n=10)	0.0092589 ± 9	0.0996949 ± 9	0.715867 ± 1	1.135845 ± 1

The number of analytical errors (2SE for individual samples and 2SD for STD) is given in the last digit of individual data.

Table 17. Macroscopic neutron-capture cross sections (Σ_{eff}), neutron fluences (Ψ), model CRE ages, and thermalized degrees of neutrons ($\varepsilon_{Sm}/\varepsilon_{Gd}$).

	Σ_{eff} (cm^2 g^{-1})	Ψ ($\times 10^{15}$ n cm^{-2})	CRE age* (Ma)	model CRE age (Ma)	$\varepsilon_{Sm}/\varepsilon_{Gd}$
Juvinas	0.0065	0.28 ± 0.03	10.6 ± 1.6	8.6 ± 0.8	0.67 ± 0.19
Millbillillie	0.0065	1.13 ± 0.02	20.8 ± 1.0	22.6 ± 0.5	0.61 ± 0.07
Stannern	0.0068	1.78 ± 0.01	35.1 ± 1.4	33.3 ± 0.2	0.65 ± 0.08
DaG 380	0.0066	1.32 ± 0.01	—	25.6 ± 0.2	0.62 ± 0.12
DaG 391	0.0068	0.67 ± 0.01	—	13.0 ± 0.1	0.63 ± 0.08
DaG 411	0.0066	0.72 ± 0.01	—	14.0 ± 0.5	0.65 ± 0.22
DaG 443	0.0067	<0.1	—	—	—
DaG 480	0.0066	2.38 ± 0.01	—	46.2 ± 0.2	0.76 ± 0.08

The number of analytical errors (2SEs for individual samples) is given in the last digit of individual data.
*^{81}Kr CRE age from Miura et al. (1998).

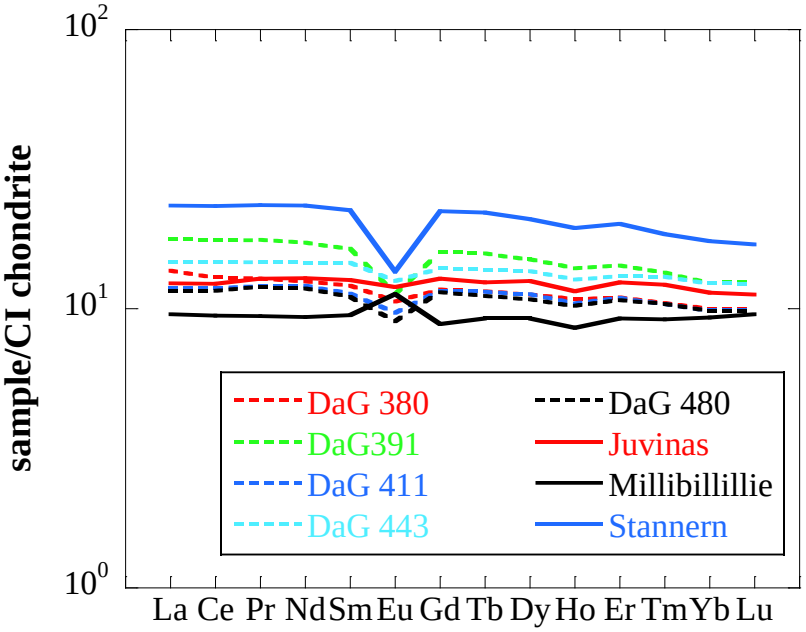

Figure 33. CI chondrite-normalized REE abundance patterns of eight eucrites used in this study. The REE data for CI chondrite are from Anders and Grevesse (1989).

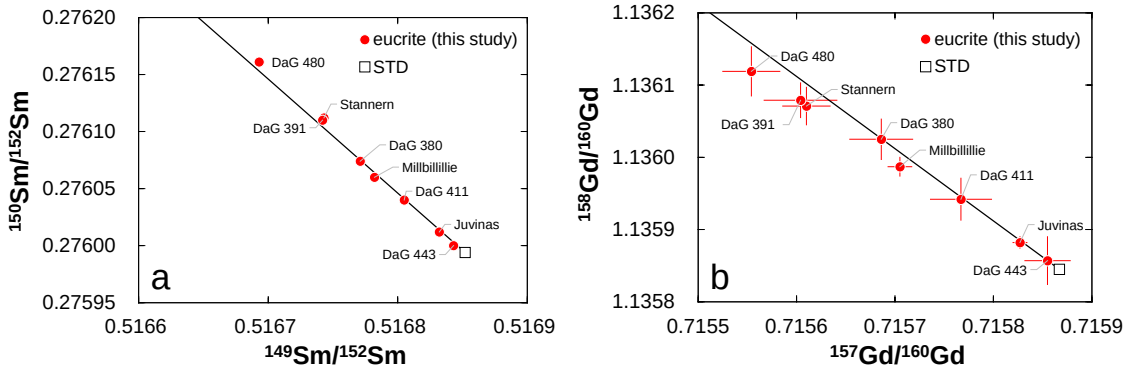

Figure 34. Correlation diagrams for (a) $^{149}Sm/^{152}Sm$ vs. $^{150}Sm/^{152}Sm$ and (b) $^{157}Gd/^{160}Gd$ vs. $^{158}Gd/^{160}Gd$. The black lines represent ideal isotopic shifts that caused by the neutron capture reactions of $^{149}Sm(n,\gamma)^{150}Sm$ and $^{157}Gd(n,\gamma)^{158}Gd$, respectively. The error bars in individual data points display 2SEs.

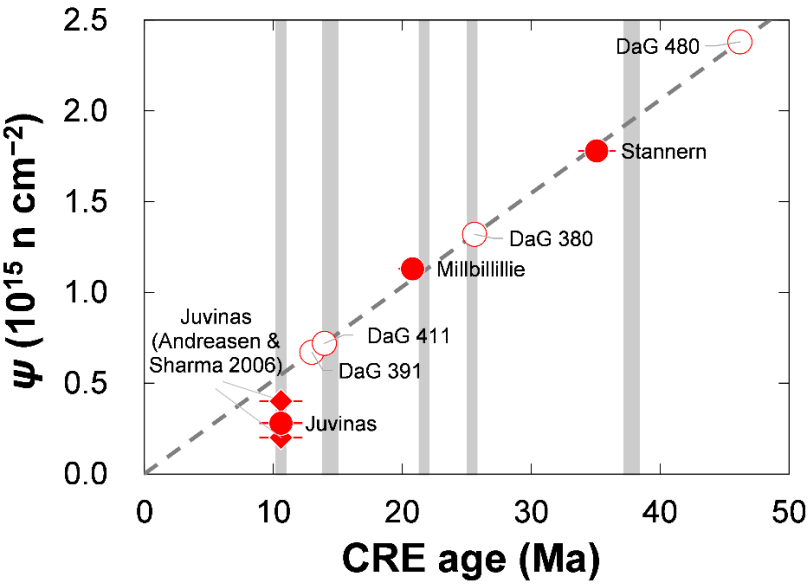

Figure 35. A correlation diagram between CRE ages (Ma) and neutron fluences (10^{15} n cm^{-2}) for eucrites. The neutron fluences of the seven eucrites are estimated from the Sm isotopic shifts in this study. The CRE ages of Juvinas, Millibillillie, and Stannern shown in red circles are from Miura et al. (1998), while those of the other four eucrites shown in white circles are given as the model ages in this study. The dashed line in the figure is a least-square regression for the red circles that passes through the origin. The gray bars represent CRE age clusters of eucrites (Miura et al., 1998).

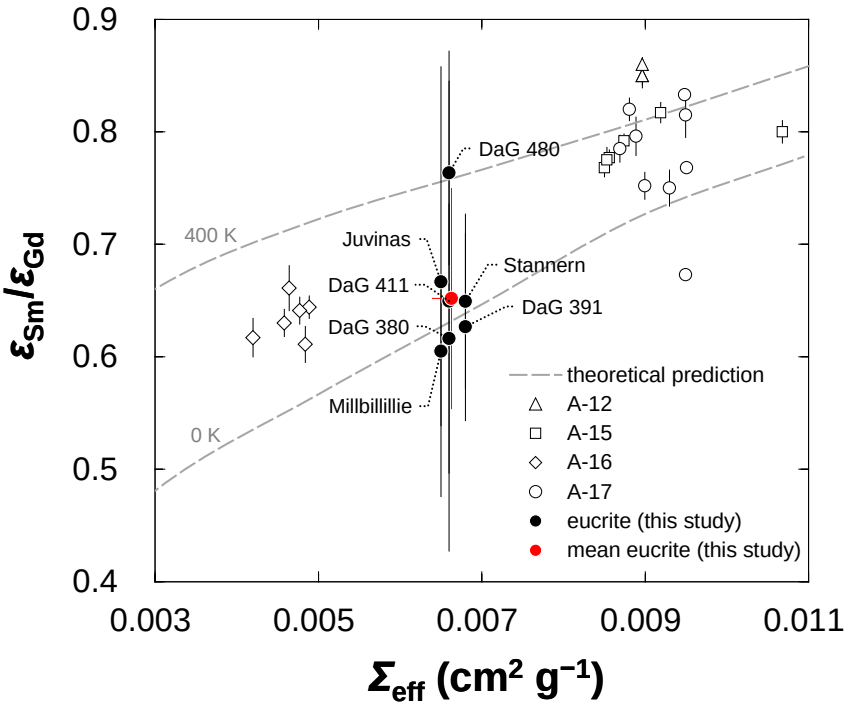

Figure 36. A correlation diagram between effective macroscopic cross section Σ_{eff} and an index for thermalized degree of neutron $\varepsilon_{Sm}/\varepsilon_{Gd}$. The data of lunar regolith samples (A-12, -15, -16, and -17) are from Hidaka et al. (1999; 2000) and Hidaka and Yoneda (2007). The error bars display 2SEs for individual samples (open symbols for lunar samples and black circles for eucrites) and 2SD for the mean eucrite (red circle). The dashed lines in the figure reveal the theoretical predictions at two different temperatures T = 0 K and 400 K given by Lingenfelter et al. (1972).

5.4. Summary

Isotopic measurements of Sm and Gd for eight eucrites were performed to understand the CRE histories of individual eucrites. As a result of the discussion on the possibility of pre-irradiation of the eight eucrites on the parent body, positive evidence was not given by the model of Lingenfelter et al. (1972) based on the combination of Sm and Gd isotopic shifts because of the large analytical uncertainties and small difference of $\varepsilon_{Sm}/\varepsilon_{Gd}$ parameters among the individual eucrites. Because the energies of the first resonance integral for neutron-capture reactions are very close between ^{149}Sm (0.0973 eV) and ^{157}Gd (0.0314 eV), the resolution of the $\varepsilon_{Sm}/\varepsilon_{Gd}$ parameters is not sufficient to distinguish the difference among the individual eucrites used in this study. Because ^{167}Er has a large resonance integral in the epithermal region ($0.5 < E < 2000$ eV), the combination of the isotopic variations between ^{149}Sm and ^{167}Er may provide a hint for the difference in CRE histories of individual meteorites. However, considering the simple comparison of the cross section for neutron capture between ^{149}Sm and ^{167}Er, a neutron fluence above 10^{16} n cm^{-2} is required to detect clearly the isotopic shift of ^{167}Er–^{168}Er. Although the combination of the isotopic shifts of Sm and Er was effectively used for lunar meteorites showing thermal neutron fluences of $(2–14) \times 10^{16}$ n cm^{-2} to determine the energy balance between thermal and epithermal neutrons (Hidaka et al., 2020), it would not be expected to find clear evidence from the same application to eucrites having thermal neutron fluences of $(0.28–2.38) \times 10^{15}$ n cm^{-2} in this study.

6. Conclusions

Although the new Hf isotope data set of the nine diogenites obtained in this study revealed isotopically distinct origins of eucrites and diogenites, three primary problems about the diogenite differentiation are still remaining; (a) quantitative relationships between crystallization ages of eucrites and diogenites, (b) genetic relationships among individual diogenites, and (c) origin of Eu anomalies in diogenites. For addressing problems (a) and (b), precise determinations of crystallization ages of diogenites based on the short-lived ^{60}Fe–^{60}Ni systematics ($t_{1/2}$ = 2.62 Ma; Rugel et al., 2009) may be useful. Because of the short half-life of ^{60}Fe, ^{60}Fe–^{60}Ni systematics provides precise chronological information for early solar system objects. Although the solar system initial abundance of ^{60}Fe is still controversial between bulk and in-situ analysis (see Elliott and Steele, 2017), this decay system will work successfully as the relative chronometer for eucrites and diogenites, whose ^{60}Fe abundances must have been once homogenized at the global magma ocean stage of Vesta.

The only existing ^{60}Fe–^{60}Ni data of diogenites have been provided by Tang and Dauphas (2012). They reported the ^{60}Fe–^{60}Ni data set of three diogenites, which is consistent with the eucrite ^{60}Fe–^{60}Ni isochron line. This suggests the simultaneous crystallization of eucrites and diogenites, which apparently conflicts with the result of this study. For revisiting the ^{60}Fe–^{60}Ni systematics of diogenites, the nine diogenites used in this study will be analyzed with the HCl-leaching treatment, while the Tang and Dauphas (2012) analyzed non-leached bulk samples. Since some diogenites contain significant amounts of metals characterized by considerably lower Fe/Ni ratios relative to those of silicates (e.g., Gooley and Moore, 1976; Floran et al., 1981; Bowman et al., 1997), the residual metal-free phases after the HCl-leaching are expected to show larger excesses of radiogenic ^{60}Ni than those of non-leached samples. This is helpful to obtain precise chronological data. The removal of terrestrial contaminants is also important effect of the HCl-leaching for the accurate isotopic dating of diogenites (see section 2.1).

Although ^{60}Fe–^{60}Ni systematics of eucrites are investigated in several previous studies (Shukolyukov and Lugmair, 1993a; 1993b; Sugiura et al., 2006; Rudraswami et al., 2010; Quitté et al., 2011; Tang and Dauphas, 2012), a systematic study using various

types of eucrite samples has not been performed yet. Furthermore, at present, there are no ^{60}Fe–^{60}Ni isotope data are for cumulate eucrites. Therefore, both cumulate and non-cumulate eucrites will be analyzed together with the diogenite samples to reveal the temporal relationships of their crystallizations in detail.

For addressing the problem (c) of the origin of Eu anomalies in diogenites shown above, a more detailed calibration of the acid-leaching method may be helpful. Since the CI-normalized concentrations of Eu in diogenites are generally lower than those of other REE, magnitudes of Eu anomalies in diogenites are easily affected by contaminations of exotic components. Hence, detailed discussions about Eu anomalies in diogenites require the almost complete removal of contaminations and accessory materials. For this purpose, the sequential acid washing procedure used in Iizuka et al. (2019), more intensive than the HCl-leaching in this study, may be effective. They applied the acid washing procedure on the pyroxene-rich fractions of several eucrites. Minor plagioclases in the fractions were effectively removed and, consequently, they obtained pure pyroxene compositions of the eucrites. An application of this acid washing procedure on the diogenite samples probably allows us more plausible discussions about Eu anomalies of diogenites than those in this study.

References

Allègre C. J. and Minster J. F. (1978) Quantitative models of trace element behavior in magma processes. *Earth Planet. Sci. Lett.* **38**: 1–25.

Ammannito E., De Sanctis M. C., Capaccioni F., Capria M. T., Carraro F., Combe J.-P., Fonte S., Frigeri A., Joy S. P., Longobardo A., Magni G., Marchi S., McCord T. B., McFadden L. A., McSween H. Y., Palomba E., Pieters C. M., Polanskey C. A., Raymond C. A., Sunshine J. M., Tosi F., Zambon F., and Russell C. T. (2013a) Vestan lithologies mapped by the visual and infrared spectrometer on Dawn. *Meteorit. Planet. Sci.* **48**: 2185–2198.

Ammannito E., De Sanctis M. C., Palomba E., Longobardo A., Mittlefehldt D. W., McSween H. Y., Marchi S., Capria M. T., Capaccioni F., Frigeri A., Pieters C. M., Ruesch O., Tosi F., Zambon F., Carraro F., Fonte S., Hiesinger H., Magni G., McFadden L. A., Raymond C. A., Russell C. T., and Sunshine J. M. (2013b) Olivine in an unexpected location on Vesta's surface. *Nature* **504**: 122–125.

Anczkiewicz R., Szczpański J., Mazur S., Storey C., Crowley Q., Villa I. M., Thirlwall M. F., and Jeffries T. E. (2007) Lu–Hf geochronology and trace element distribution in garnet: Implications for uplift and exhumation of ultra-high pressure granulites in the Sudetes, SW Poland. *Lithos* **95**: 363–380.

Albalat E., Blichert-Toft J., Telouk P., and Albarède F. (2015) The lunar neutron energy spectrum inferred from the isotope compositions of rare-earth elements and hafnium in Apollo samples. *Earth Planet. Sci. Lett.* **429**: 147–156.

Anders E. and Grevesse N. (1989) Abundances of the elements: Meteoritic and solar. *Geochim. Cosmochim. Acta* **53**: 197–214.

Barrat J.-A., Blichert-Toft J., Gillet P., and Keller F. (2000) The differentiation of eucrites: The role of *in situ* crystallization. *Meteorit. Planet. Sci.* **35**: 1087–1100.

Barrat J.-A., Gillet Ph., Lesourd M., Blichert-Toft J., and Poupeau G. R. (1999) The Tatahouine diogenite: Mineralogical and chemical effects of sixty-three years of terrestrial residence. *Meteorit. Planet. Sci.* **34**: 91–97.

Barrat J.-A., Jambon A., Bohn M., Blichert-Toft J., Sautter V., Göpel C., Gillet Ph, and Boudouma O. (2003) Petrology and geochemistry of the unbrecciated achondrite Northwest Africa 1240 (NWA 1240): An HED parent body impact melt. *Geochim. Cosmochim. Acta* **67**: 3959–3970.

Barrat J.-A. and Yamaguchi A. (2014) Comment on "The origin of eucrites, diogenites, and olivine diogenites: Magma ocean crystallization and shallow magma chamber processes on Vesta" by B. E. Mandler and L. T. Elkins-Tanton. *Meteorit. Planet. Sci.* **49**: 468–472.

Barrat J.-A., Yamaguchi A., Greenwood R. C., Benoit M., Cotton J., Bohn M., and Franchi I. (2008) Geochemistry of diogenites: Still more diversity in their parental melts. *Meteorit. Planet. Sci.* **43**: 1759–1775.

Barrat J.-A., Yamaguchi A., Greenwood R. C., Bohn M., Cotton J., Benoit M., and Franchi I. A. (2007) The Stannern trend eucrites: Contamination of main group eucrite magmas by crustal partial melting. *Geochim. Cosmochim. Acta* **71**: 4108–4124.

Barrat J.-A., Yamaguchi A., Zanda B., Bollinger C., and Bohn M. (2010) Relative chronology of crust formation on asteroid 4 Vesta: Insights from the geochemistry of diogenites. *Geochim. Cosmochim. Acta* **74**: 6218–6231.

Bast R., Scherer E. E., Sprung P., Fischer-Gödde M., Stracke A., and Mezger K. (2015) A rapid and efficient ion-exchange chromatography for Lu–Hf, Sm–Nd, and Rb–Sr geochronology and the routine isotope analysis of sub-ng amounts of Hf by MC-ICP-MS. *J. Anal. At. Spectrom.* **30**: 2323–2333.

Beck A. W., Lawrence D. J., Peplowski P. N., Viviano-Beck C. E., Prettyman T. H., McCoy T. J., McSween H. Y., and Yamashita N. (2017) Igneous lithologies on asteroid (4) Vesta mapped using gamma-ray and neutron data. *Icarus* **286**: 35–45.

Bermingham K. R., Mezger K., Scherer E. E., Horan M. F., Carlson R. W., Upadhyay D., Magna T., and Pack A. (2016) Barium isotope abundances in meteorites and their implications for early Solar System evolution. *Geochim. Cosmochim. Acta* **175**: 282–298.

Beunon H., Chernonozhkin S. M., Mattielli N., Goderis S., Doucet L. S., Debaille V., and Vanhaecke F. (2020) Innovative two-step isolation of Ni prior to stable isotope ratio measurements by MC-ICP-MS: Application to igneous geological reference materials. *J. Anal. At. Spectrom*. **35**: 2213–2223.

Binzel R. P. and Xu S. (1993) Chips off of asteroid 4 Vesta: Evidence for the parent body of basaltic achondrite meteorites. *Science* **260**: 186–191.

Bio-Rad Laboratories (2000) AG® 50W and AG MP-50 cation exchange resins instruction manual. <http://www.bio-rad.com/webroot/web/pdf/lsr/literature/LIT203.pdf>

Birck J. L. and Allègre (1981) $^{87}Rb/^{87}Sr$ study of diogenites. *Earth Planet. Sci. Lett.* **55**: 116–122.

Birck J. L. and Lugmair G. W. (1988) Nickel and chromium isotopes in Allende inclusions. *Earth Planet. Sci. Lett.* **90**: 131–143.

Bland P. A., Zolensky M. E., Benedix G. K., and Sephton M. A. (2006) Weathering of chondritic meteorites. In Meteorites and the early solar system II, edited by Lauretta D. S., Leshin L. A., and McSween H. Y., Tucson, Arizona: The University of Arizona Press. pp. 853–867.

Blichert-Toft J. and Albarède F. (1997) The Lu–Hf isotope geochemistry of chondrites and the evolution of the mantle–crust system. *Earth Planet. Sci. Lett.* **148**: 243–258.

Blichert-Toft J., Boyet M., Télouk P., and Albarède F. (2002) ^{147}Sm–^{143}Nd and ^{176}Lu–^{176}Hf in eucrites and the differentiation of the HED parent body. *Earth Planet. Sci. Lett.* **204**: 167–181.

Blichert-Toft J., Chauvel C., and Albarède F. (1997) Separation of Hf and Lu for high-precision isotope analysis of rock samples by magnetic sector-multiple collector ICP-MS. *Contrib. Mineral. Petrol.* **127**: 248–260.

Bloch E., Watkins J., and Ganguly J. (2017) Diffusion kinetics of lutetium in diopside the effect of thermal metamorphism on Lu–Hf systematics in clinopyroxene. *Geochim. Cosmochim. Acta* **204**: 32–51.

Bogard D. D. and Garrison D. H. (2003) ^{39}Ar–^{40}Ar ages of eucrites and thermal history of asteroid 4 Vesta. *Meteorit. Planet. Sci.* **38**: 669–710.

Bouvier A., Blichert-Toft J., Boyet M., and Albarède F. (2015) ^{147}Sm–^{143}Nd and ^{176}Lu–^{176}Hf systematics of eucrite and angrite meteorites. *Meteorit. Planet. Sci.* **50**: 1896–1911.

Bouvier A., Vervoort J. D., and Patchett P. J. (2008) The Lu–Hf and Sm–Nd isotopic composition of CHUR: Constraints from unequilibrated chondrites and implications for the bulk composition of terrestrial planets. *Earth Planet. Sci. Lett.* **273**: 48–57.

Bowman L. E., Spilde M. N., and Papike J. J. (1997) Automated energy dispersive spectrometer modal analysis applied to the diogenites. *Meteorit. Planet. Sci.* **32**: 869–875.

Boyet M. and Carlson R. W. (2005) ^{142}Nd evidence for early (>4.53 Ga) global differentiation of the silicate Earth. *Science* **309**: 576–581.

Boyet M., Carlson R. W., and Horan M. (2010) Old Sm–Nd ages for cumulate eucrites and redetermination of the solar system initial 146Sm/144Sm ratio. *Earth Planet. Sci. Lett.* **291**: 172–181.

Brennecka G. A. and Kleine T. (2017) A low abundances of ^{135}Cs in the Early Solar System from barium isotopic signatures of volatile-depleted meteorites. *Astrophys. J. Lett.* **837**: L9.

Buchanan P. C., Noguchi T., Bogard D. D., Ebihara M., and Katayama I. (2005) Glass veins in the unequilibrated eucrite Yamato 82202. *Geochim. Cosmochim. Acta* **69**: 1883–1898.

Burnett D. S., Huneke J. C., Podosek F. A., Russ G. P., Turner G., and Wasserburg G. J. (1972) The irradiation history of lunar samples. *Lunar Planet. Sci. Conf*. **III**: 105 (abstract).

Cherniak D. J. and Liang Y. (2007) Rare earth element diffusion in natural enstatite. *Geochim. Cosmochim. Acta* **71**: 1324–1340.

Chernonozhkin S. M., Goderis S., Lobo L., Claeys P., and Vanhaecke F. (2015) Development of an isolation procedure and MC-ICP-MS measurement protocol for the study of stable isotope ratio variations of nickel. *J. Anal. At. Spectrom.* **30**: 1518–1530.

Clenet H, Jutzi M., Barrat J.-A., Asphaug E. I., Benz W., and Gillet P. (2014) A deep crust–mantle boundary in the asteroid 4 Vesta. *Nature* **511**: 303–306.

Conant J. B. and Tuttle N. (1921a) Diacetone alcohol. *Org. Synth.* **1**: 45.

Conant J. B. and Tuttle N. (1921b) Mesityl oxide. *Org. Synth.* **1**: 53.

Consolmagno G. J. and Drake M. J. (1977) Composition and evolution of the eucrite parent body: Evidence from rare earth elements. *Geochim. Cosmochim. Acta* **41**: 1271–1282.

Consolmagno G. J., Golabek G. J., Turrini D., Jutzi M., Sirono S., Svetsov V., and Tsiganis K. (2015) Is Vesta an intact and pristine protoplanet? *Icarus* **254**: 190–201.

Cook D. L., Wadhwa M., Janney P. E., Dauphas N., Clayton R. N., and Davis A. M. (2006) High precision measurements of non-mass-dependent effects in nickel isotopes in meteoritic metal via multicollector ICPMS. *Anal. Chem.* **78**: 8477–8484.

Crozaz G., Floss C., and Wadhwa M. (2003) Chemical alteration and REE mobilization in meteorites from hot and cold deserts. *Geochim. Cosmochim. Acta* **67**: 4727–4741.

Dale C. W., Burton K. W., Greenwood R. C., Gannoun A., Wade J., Wood B. J., and Pearson D. G. (2012) Late accretion on the earliest planetesimals revealed by the highly siderophile elements. *Science* **336**: 72–75.

Davison T. M., Collins G. S., and Ciesla F. J., Numerical modeling of heating in porous planetesimal collisions. *Icarus* **208**: 468–481.

Day J. M. D., Walker R. J., Qin L., and Rumble III D. (2012) Late accretion as a natural consequence of planetary growth. *Natur. Geosci.* **5**: 614–617.

Domanik A., Kolar S., White D. M., and Drake M. J. (2004) Accessory silicate mineral assemblages in the Bilanga meteorites: A petrographic study. *Meteorit. Planet. Sci.* **39**: 567–579.

Elliott T. and Steele R. C. J. (2017) The isotope geochemistry of Ni. *Rev. Mineral. Geochem.* **82**: 511–542.

Elkins-Tanton L. T., Maroon E., Krawczynski M. J., and Grove T. L. (2008) Magma ocean solidification processes on Vesta. *Lunar Planet. Sci. Conf.* **XXXIX**: #1364 (abstract).

Eugster O. and Michel T. H. (1994) Common asteroid break-up of eucrites, diogenites, and howardites and cosmic-ray production rates for noble gases in achondrites. *Geochim. Cosmochim. Acta* **59**: 177–199.

Floran R. J., Prinz M., Hlava P. F., Keil K., Spettel B., and Wänke (1981) Mineralogy, petrology, and trace element geochemistry of the Johnstown meteorite: A brecciated orthopyroxenite with siderophile and REE-rich components. *Geochim. Cosmochim. Acta* **45**: 2385–2391.

Floss C. and Crozaz G. (1991) Ce anomalies in the LEW85300 eucrite: Evidence for REE mobilization during Antarctic weathering. *Earth Planet. Sci. Lett*. **107**: 13–24.

Friedman A. M., Milsted J., Mett D., Henderson D., Lerner J., Harkness A. L., and Rok Op D. J. (1966) Alpha decay half lives of ^{148}Gd ^{150}Gd and ^{146}Sm. *Radiochim. Acta* **5**: 192–194.

Fukuoka T., Boynton W. V., Ma M.-S., and Schmitt R. A. (1977) Genesis of howardites, diogenites, and eucrites. *Proc. Lunar Sci. Conf.* **8**: 187–210.

Gall L., Williams H., Siebert C., and Halliday H. (2012) Determination of mass-dependent variations in nickel isotope compositions using double spiking and MC-ICP-MS. *J. Anal. At. Spectrom.* **27**: 137–145.

Ghiorso M. S., Hirschmann M. M., Reiners P. W., and Kress V. C. III (2002) The pMELTS: A revision of MELTS aimed at improving calculation of phase relations and major element partitioning involved in partial melting of the mantle at pressures up to 3 GPa. *Geochem. Geophys. Geosyst.* **3**: 2001GC000217.

Giddings J. C. (1963) Kinetic origin of tailing in chromatography. *Anal. Chem.* **35**: 1999–2002.

Gooley R. and Moore C. B. (1976) Native metal in diogenite meteorites. *Am. Mineral.* **61**: 373–378.

Gounelle M., Zolensky M. E., Liou J.-C., Bland P. A., and Alard O. (2003) Mineralogy of carbonaceous chondritic microclasts in howardites: Identification of C2 fossil micrometeorites. *Geochim. Cosmochim. Acta* **67**: 507–527.

Gramlich J. W., Machlan L. A., Barnes J. L., and Paulsen P. J. (1989) Absolute isotope abundance ratios and atomic weight of a reference sample of nickel. *J. Res. Natl. Inst. Stand. Technol.* **94**: 347–356.

Greenwood R. C., Barrat J.-A., Yamaguchi A., Franchi I. A., Scott E. R. D., Bottke W. F., and Gibson J. M. (2014) The oxygen isotope composition of diogenites: Evidence for early global melting on a single, compositionally divers, HED parent body. *Earth Planet. Sci. Lett.* **390**: 165–174.

Greenwood R. C., Franchi I. A., Jambon A., Barrat J. A., and Burbine T. H. (2006) Oxygen isotope variation in stony-iron meteorites. *Science* **313**: 1763–1765.

Grossman J. N. (1999) The Meteoritical Bulletin, No. 83, 1999 July. *Meteorit. Planet. Sci.* **34**: A169–A186.

Grossman J. N. and Zipfel J. (2001) The Meteoritical Bulletin, No. 85, 2001 September. *Meteorit. Planet. Sci.* **36**: A293–A322.

Gueguen B., Rouxel O., Ponzevera E., Bekker A., and Fouquet Y. (2013) Nickel isotope variations in terrestrial silicate rocks and geological reference materials measured by MC-ICP-MS. *Geostand. Geoanal. Res.* **37**: 297–317.

Haba M. K., Wotzlaw J.-F., Lai Y.-J., Yamaguchi A., and Schönbächler M. (2019) Mesosiderite formation on asteroid 4 Vesta by a hit-and-run collision. *Natur. Geosci.* **12**: 510–515.

Haba M. K., Yamaguchi A., Horie K., and H. Hidaka (2014) Major and trace elements of zircons from basaltic eucrites: Implications for the formation of zircons on the eucrite parent body. *Earth Planet. Sci. Lett*. **387**: 10–21.

Hans U., Kleine T., and Bourdon B. (2013) Rb–Sr chronology of volatile depletion in differentiated protoplanets: BABI, ADOR and ALL revisited. *Earth Planet. Sci. Lett.* **374**: 204–214.

Harrison T. M., Armstrong R. L., Naeser C. W., and Harakal J. E. (1979) Geochronology and thermal history of the Coast Plutonic Complex, near Prince Rupert, British Columbia. *Can. J. Earth Sci.* **16**: 400–410.

Hidaka H. and Ebihara M. (1995) Determination of the isotopic compositions of samarium and gadolinium by thermal ionization mass spectrometry. *Anal. Chem.* **67**: 1437–1441.

Hidaka H., Ebihara M., and Yoneda S. (1999) High fluences of neutrons determined from Sm and Gd isotopic compositions in aubrites. *Earth Planet. Sci. Lett.* **173**: 41–51.

Hidaka H., Ebihara M., and Yoneda S. (2000) Neutron capture effects on samarium, europium, and gadolinium in Apollo 15 deep drill-core samples. *Meteorit. Planet. Sci*. **35**: 581–589.

Hidaka H., Kondo T., and Yoneda S. (2012) Heterogeneous isotopic anomalies of Sm and Gd in the Norton County meteorite: Evidence for irradiation from the active early Sun. *Astrophys. J.* **746**: 132.

Hidaka H., Mizutani Y., and Yoneda S. (2020) Estimation of thermal and epithermal neutron fluences at the lunar surface from isotopic composition of rare earth elements. *Astrophys. J.* **904**: 183.

Hidaka H., Sakuma K., Nishiizumi K., and Yoneda S. (2017) Isotopic evidence for multi-stage cosmic-ray exposure histories of lunar meteorites: Long residence on the Moon and short transition to the Earth. *Astrophys. J.* **153**: 274.

Hidaka H. and Yoneda S. (2007) Sm and Gd isotopic shifts of Apollo 16 and 17 drill stem samples and their implications for regolith history. *Geochim. Cosmochim. Acta* **71**: 1074–1086.

Hidaka H. and Yoneda S. (2014) Isotopic excesses of proton-rich nuclei related to space weathering observed in a gas-rich meteorite Kapoeta. *Astrophys. J.* **786**: 138.

Hidaka H., Yoneda S., Nishiizumi K., and Caffee M. (2022) The neutron energy spectra of lunar meteorites evaluated from Sm and Er isotopic compositions. *Astrophys. J*. **925**: 209.

Hidaka H. and Yoneda S. (2016) Rb–Sr and Cs–Ba systematics of eucrites. *Annual Meeting of the Meteoritical Society* **79**: #6125 (abstract).

Hublet G., Debaille V., Wimpenny J., and Yin Q.-Z. (2017) Differentiation and magmatic activity in Vesta evidenced by ^{26}Al–^{26}Mg dating in eucrites and diogenites. *Geochim. Cosmochim. Acta* **218**: 73–97.

Hughes H. J., Delvigne C., Korntheuer M., de Jong J., André L., and Cardinal D. (2011) Controlling the mass bias introduced by anionic and organic matrices in silicon isotopic measurements by MC-ICP-MS. *J. Anal. At. Spectrom.* **26**: 1892–1896.

Iizuka T., Jourdan F., Yamaguchi A., Koefoed P., Hibiya Y., Ito K. T. M., and Amelin Y. (2019) The geologic history of Vesta inferred from combined $^{207}Pb/^{206}Pb$ and $^{40}Ar/^{39}Ar$ chronology of basaltic eucrites. *Geochim. Cosmochim. Acta* **267**: 275–299.

Iizuka T., Yamaguchi A., Haba M. K., Amelin Y., Holden P., Zink S., Huyskens M. H., and Ireland T. R. (2015a) Timing of global crustal metamorphism on Vesta as revealed by high precision U–Pb dating and trace element chemistry of eucrite zircon. *Earth Planet. Sci. Lett.* **409**: 182–192.

Iizuka T., Yamaguchi T., Hibiya Y., and Amelin Y. (2015b) Meteorite zircon constraints on the bulk Lu–Hf isotope composition and early differentiation of the Earth. *Proc. Natl. Acad. Sci. USA* **112**: 5331–5336.

Ireland T. J., Tissot F. L. H., Yokochi R., and Dauphas N. (2013) Teflon-HPLC: A novel chromatographic system for application to isotope geochemistry and other industries. *Chem. Geol.* **357**: 203–214.

Kagami S. and Yokoyama T. (2016) Chemical separation of Nd from geological samples for chronological studies using ^{146}Sm–^{142}Nd and ^{147}Sm–^{143}Nd systematics. *Anal. Chim. Acta* **937**: 151–159.

Kaneoka I., Ozima M., and Yanagisawa M. (1979) ^{40}Ar–^{39}Ar age studies of four Yamato-74 meteorites. *Mem. Natl. Inst. Polar Res., Spec. Issue* **12**: 186–206.

Kennedy A. K., Lofgren G. E., and Wasserburg G. J. (1993) An experimental study of trace element partitioning between olivine, orthopyroxene and melt in chondrules: Equilibrium values and kinetic effects. *Earth Planet. Sci. Lett.* **115**: 177–195.

Kinoshita K., Paul M., Kashiv Y., Collon P., Deibel C. M., DiGiovine B., Greene J. P., Henderson D. J., Jiang C. L., Marley S. T., Nakanishi T., Pardo R. C., Rehm K. E., Robertson D., Scott R., Schmitt C., Tang X. D., Vondrasek R., and Yokoyama A. (2012) A shorter ^{146}Sm half-life measured and implications for ^{146}Sm–^{142}Nd chronology in the Solar System. *Science* **335**: 1614–1617.

Klaver M., Ionov D. A., Takazawa E., and Elliot T. (2020) The non-chondritic Ni isotope composition of Earth's mantle. *Geochim. Cosmochim. Acta* **268**: 405–421.

Korkisch J. (1966) Combined ion exchange–solvent extraction (CIESE): A novel separation technique for inorganic ions. *Sep. Sci.* **1**: 159–171.

Korkisch J. and Ahluwalia S. S. (1967) Cation-exchange behavior of several elements in hydrochloric acid–organic solvent media. *Talanta* **14**: 155–170.

Larsen K. K., Wielandt D., and Bizzarro M. (2018) Multi-element ion-exchange chromatography and high-precision MC-ICP-MS isotope analysis of Mg and Ti from sub-mm-sized meteorite inclusions. *J. Anal. At. Spectrom.* **33**: 613–628.

Larsen K. K., Wielandt D., Schiller M., and Bizzarro M. (2016) Chromatographic speciation of Cr(III)-species, inter-species equilibrium isotope fractionation and improved chemical purification strategies for high-precision isotope analysis. *J. Chromatogr. A* **1443**: 162–174.

Lee M. R. and Bland P. A. (2004) Mechanisms of weathering of meteorites recovered from hot and cold deserts and the formations of phyllosilicates. *Geochim. Cosmochim. Acta* **68**: 893–916.

Liang Y., Cherniak D. J., Morgan Z. T., and Hess P. C. (2004) Eu^{2+} and REE^{3+} diffusion in enstatite, diopside, anorthite, and a silicate melt: A database for understanding kinetic fractionation of REE in the lunar mantle and crust. *Lunar Planet. Sci.* **XXXV**: #1894 (abstract).

Lingenfelter R. E., Canfield E. H., and Hampel V. E. (1972) The lunar neutron flux revisited. *Earth Planet. Sci. Lett.* **16**: 355–369.

Lorenzetti S., Eugster O., Busemann H., Marti K., Burbine T. H., and McCoy T. (2003) History and origin of aubrites. *Geochim. Cosmochim. Acta* **67**: 557–571.

Ludwig K. R. (2012) User's manual for Isoplot 3.70. *Berkeley Geochronol. Cent. Spec. Publ.*

Lugmair G. W. and Marti K. (1971) Neutron capture effects in lunar gadolinium and the irradiation histories of some lunar rocks. *Earth Planet. Sci. Lett.* **13**: 32–42.

Lugmair G. W. and Shukolyukov A. (1998) Early solar system timescales according to ^{53}Mn–^{53}Cr systematics. *Geochim. Cosmochim. Acta* **62**: 2863–2886.

Makishima A. and Masuda A. (1993) Primordial Ce isotopic composition of the Solar System. *Chem. Geol.* **106**: 197–205.

Mandler B. E. and Elkins-Tanton L. T. (2013) The origin of eucrites, diogenites, and olivine diogenites: Magma ocean crystallization and shallow magma chamber processes on Vesta. *Meteorit. Planet. Sci.* **48**: 2333–2349.

Marchi S., Bottke W. F., Cohen B. A., Wünnemann K., Kring D. A., McSween H. Y., De Sanctis M. C., O'Brien D. P., Schenk P., Raymond C. A., and Russell C. T. (2013) High-velocity collisions from the lunar cataclysm recorded in asteroidal meteorites. *Nat. Geosci.* **6**: 303–307.

Maréchal C. N., Télouk P., and Albarède F. (1999) Precise analysis of copper and zinc isotopic compositions by plasma-source mass spectrometry. *Chem. Geol.* **156**: 251–272.

Marks N. E., Borg L. E., Hutcheon I. D., Jacobsen B., and Clayton R. N. (2014) Samarium–neodymium chronology and rubidium–strontium systematics of an Allende calcium–aluminum-rich inclusion with implications for ^{146}Sm half-life. *Earth Planet. Sci. Lett.* **405**: 15–24.

Mason B. (1962) Meteorites. Wiley, New York.

Masuda A. and Matsui Y. (1966) The difference in lanthanide abundance pattern between the crust and the chondrite and its possible meaning to the genesis of crust and mantle. *Geochim. Cosmochim. Acta* **30**: 239–250.

McCord T. B., Adams J. B., and Johnson T. V. (1970) Asteroid Vesta: Spectral reflectivity and compositional implications. *Science* **168**: 1445–1447.

McIntyre G. A., Brooks C., Compston W., and Turek A. (1966) The statistical assessment of Rb–Sr isochrons. *J. Geophys. Res.* **71**: 5459–5468.

McKay G., Le L., Wagstaff J., and Crozaz G. (1994) Experimental partitioning of rare earth elements and strontium: Constraints on petrogenesis and redox conditions during crystallization of Antarctic angrite Lewis Cliff 86010. *Geochim. Cosmochim. Acta* **58**: 2911–2919.

Meija J., Coplen T. B., Berglund M., Brand W. A., Bièvre P. D., Gröning M., Holden N. E., Irrgeher J., Loss R. D., Walczyk T., and Prohaska T. (2016) Isotopic compositions of the elements 2013 (IUPAC Technical Report). *Pure Appl. Chem.* **88**: 293–306.

Meissner F., Schmidt-Ott W. D., and Ziegeler L. (1987) Half-life and a-ray energy of ^{146}Sm. *Z. Physik. A – Atomic Nuclei* **327**: 171–174.

Meteoritical Bulletin Database (2020) Retrieved 9 Jan. 2020. http://www.lpi.usra.edu/meteor/

Michel T. H. and Eugster O. (1994) Primitive xenon in diogenites and plutonium-244-fission xenon ages of a diogenite, a howardite, and eucrites. *Meteoritics* **29**: 593–606.

Mitchell J. T. and Tomkins A. G. (2019) On the source of diogenites and olivine diogenites: Compositional diversity from variable fO_2. *Geochim. Cosmochim. Acta* **258**: 37–49.

Mittlefehldt D. W. (1994) The genesis of diogenites and HED parent body petrogenesis. *Geochim. Cosmochim. Acta* **58**: 1537–1552.

Mittlefehldt D. W. (2015) Asteroid (4) Vesta: I. howardite–eucrite–diogenite (HED) clan of meteorites. *Chem. Erde* **75**: 155–183.

Mittlefehldt D. W., Beck A. W., Lee C.-T. A., McSween H. Y. Jr., and Buchanan P. C. (2012) Compositional constraints on the genesis of diogenites. *Meteorit. Planet. Sci.* **47**: 72–98.

Mittlefehldt D. W. and Lindstrom M. M. (1991) Generation of abnormal trace element abundances in Antarctic eucrites by weathering processes. *Geochim. Cosmochim. Acta* **55**: 77–87.

Miura Y. N., Hidaka H., Nishiizumi K., and Kusakabe M. (2007) Noble gas and oxygen isotope studies of aubrites: A clue to origin and histories. *Geochim. Cosmochim. Acta* **71**: 251–270.

Miura Y. N., Nagao K., Sugiura N., Fujitani T., and Warren P. H. (1998) Noble gases, ^{81}Kr–Kr exposure ages and ^{244}Pu–Xe ages of six eucrites, Béréba, Binda, Camel Donga, Juvinas, Millbillillie, and Stannern. *Geochim. Cosmochim. Acta* **62**: 2369–2387.

Mizutani Y., Hidaka H., and Yoneda S. (2020) Chemical separation and determination of the isotopic compositions of dysprosium, erbium, ytterbium in geochemical materials by thermal ionization mass spectrometry. *Geochem. J.* **54**: 381–391.

Moore L. J., Murphy T. J., Barnes I. L., and Paulsen P. J. (1982) Absolute isotopic abundance ratios and atomic weights of a reference sample of strontium. *J. Res. Natl. Bur. Stand.* **87**: 1–8.

Morand P. and Allègre C. J. (1983) Nickel isotopic studies in meteorites. *Earth Planet. Sci. Lett.* **63**: 167–176.

Moynier F., Blichert-Toft J., Telouk P., Luck J.-M., and Albarède F. (2007) Comparative stable isotope geochemistry of Ni, Cu, Zn, and Fe in chondrites and iron meteorites. *Geochim. Cosmochim. Acta* **71**: 4365–4379.

Münker C., Weyer S., Scherer E., and Mezger K. (2001) Separation of high field strength elements (Nb, Ta, Zr, Hf) and Lu from rock samples for MC-ICPMS measurements. *Geochem. Geophys. Geosyst.* **2**: 2001GC000183.

Nakamura N. (1979) A preliminary isotopic study on four Yamato diogenites —Sm–Nd and Rb–Sr systematics—. *Mem. Natl. Inst. Polar Res., Spec. Issue* **15**: 219–226.

Nanne J. A. M., Nimmo F., Cuzzi J. N., and Kleine T. (2019) Origin of the non-carbonaceous–carbonaceous meteorite dichotomy. *Earth Planet. Sci. Lett.* **511**: 44–54.

Neumann W., Breuer D., and Spohn T. (2014) Differentiation of Vesta: Implications for a shallow magma ocean. *Earth Planet. Sci. Lett.* **395**: 267–280.

Nishiizumi K., Caffee M. W., Jull A. J. T., and Reedy R. C. (1996) Exposure history of lunar meteorites Queen Alexandra Range 93069 and 94269. *Meteorit. Planet. Sci.* **31**: 893–896.

Nishikawa Y., Nakamura N., Misawa K., Okano O., Kagami H., and Yamamoto K. (1990) Investigation of the weathering effect on Rb–Sr systematics and trace element abundances in antarctic and non-antarctic meteorites: A case of H-chondrites. *J. Mass Spectrom. Soc. Jpn.* **38**: 115–123.

Notsu K., Mabuchi H., Yoshida O., Matsuda J., and Ozima M. (1973) Evidence of the extinct nuclides ^{146}Sm in “Juvinas” achondrite. *Earth Planet. Sci. Lett.* **19**: 29–36.

Papanastassiou D. A. and Wasserburg G. J. (1969) Initial strontium isotopic abundances and the resolution of small time differentiation in the formation of planetary objects. *Earth Planet. Sci. Lett.* **5**: 361–376.

Parkhurst D. L. and Appelo C. A. J. (2013) Description of input and examples for PHREEQC version 3: A computer program for speciation, batch-reaction, one-dimensional transport, and inverse geochemical calculations. *in: US Geological Survey Techniques and Methods*, Book 6, Modeling Techniques.

Patchett P. J. and Tatsumoto M. (1980) A routine high-precision method for Lu–Hf isotope geochemistry and chronology. *Contrib. Mineral. Petrol.* **75**: 263–267.

Patchett P. J., Vervoort J. D., Söderlund U., and Salters V. J. M. (2004) Lu–Hf and Sm–Nd isotopic systematics in chondrites and their constraints on the Lu–Hf properties of the Earth. *Earth Planet. Sci. Lett.* **222**: 29–41.

Peters S. T. M., Münker C., Pfeifer M., Elfers B.-O., and Sprung P. (2017) Distribution of p-process ^{174}Hf in early solar system materials and the origin of nucleosynthetic Hf and W isotope anomalies in Ca–Al rich inclusions. *Earth Planet. Sci. Lett.* **459**: 70–79.

Prettyman T. H., Mittlefehldt D. W., Yamashita N., Lawrence D. J., Beck A. W., Feldman W. C., McCoy T. J., McSween H. Y., Toplis M. J., Titus T. N., Tricarico P., Reedy R. C., Hendricks J. S., Forni O., Corre L. L., Li J.-Y., Mizzon H., Reddy V., Raymond C. A., and Russell C. T. (2012) Elemental mapping by Dawn reveals Exogenic H in Vesta's regolith. *Science* **338**: 242–246.

Quitté G., Latkoczy C., Schönbächler M., Halliday A. N., and Günther D. (2011) ^{60}Fe–^{60}Ni systematics in the eucrite parent body: A case study of Bouvante and Juvinas. *Geochim. Cosmochim. Acta* **75**: 7698–7706.

Quitté G., Meier M., Latkoczy C., Halliday A. N., and Günther D. (2006) Nickel isotope in iron meteorites–nucleosynthetic anomalies in sulphides with no effects in metals and no trace of ^{60}Fe. *Earth Planet. Sci. Lett.* **242**: 16–25.

Quitté G. and Oberli F. (2006) Quantitative extraction and high precision isotope measurements of nickel by MC-ICPMS. *J. Anal. At. Spectrom.* **21**: 1249–1255.

Regelous M., Elliott T., and Coath C. D. (2008) Nickel isotope heterogeneity in the early Solar System. *Earth Planet. Sci. Lett.* **272**: 330–338.

Render J., Brennecka G. A., Wang S.-J., Wasylenki L. E., and Kleine T. (2018) A distinct nucleosynthetic heritage for early solar system solids recorded by Ni isotope signatures. *Astrophys. J.* **862**: 26.

Righter K. and Drake M. J. (1997) A magma ocean on Vesta: Core formation and petrogenesis of eucrites and diogenites. *Meteorit. Planet. Sci.* **32**: 929–944.

Rudraswami N. G., Sahijpal S., and Bhandari N. (2010) Presence of ^{60}Fe in eucrites Piplia Kalan: A new perspective to the initial ^{60}Fe/^{56}Fe in the early solar system. *Curr. Sci.* **99**: 948–952.

Rugel G., Faestermann T., Knie K., Korschinek G., Poutivstev M., Shumann D., Kivel N., Günther-Leopold I., Winreich R., and Wohlmunther M. (2009) New measurement of the ^{60}Fe half-life. *Phys. Rev. Lett.* **103**: 072502.

Russ G. P. (1973) Apollo 16 neutron stratigraphy. *Earth Planet. Sci. Lett.* **19**: 275–289.

Russ G. P., Burnett D. S., Lingenfelter R. E., and Wasserburg G. J. (1971) Neutron capture on ^{149}Sm in lunar samples. *Earth Planet. Sci. Lett*. **13**: 53–60.

Russ G. P., Burnett D. S., and Wasserburg G. J. (1972) Lunar neutron stratigraphy. *Earth Planet. Sci. Lett.* **15**: 172–186.

Russell C. T., Raymond C. A., Coradini A., McSween H. Y., Zuber M. T., Nathues A., De Sanctis M. C., Jaumann R., Konopliv A. S., Preusker F., Asmar S. W., Park R. S., Gaskell R., Keller H. U., Mottola S., Roatsch T., Scully J. E. C., Smith D. E., Tricarico P., Toplis M. J., Christensen U. R., Feldman W. C., Lawrence D. J., McCoy T. J., Prettyman T. H., Reedy R. C., Sykes M. E., and Titus T. N. (2012) Dawn at Vesta: Testing the protoplanetary paradigm. *Science* **336**: 684–686.

Russell W. A., Papanastassiou D. A., and Tombrello T. A. (1978) Ca isotope fractionation on the Earth and other solar system materials. *Geochim. Cosmochim. Acta* **42**: 1075–1090.

Ruzicka A., Snyder G. A., Taylor L. A. (1997) Vesta as the howardite, eucrite and diogenite parent body: Implications for the size of a core and for large-scale differentiation. *Meteorit. Planet. Sci.* **32**: 825–840.

Sahijpal S., Soni P., and Gupta G. (2007) Numerical simulations of the differentiation of accreting planetesimals with ^{26}Al and ^{60}Fe as the heat sources. *Meteorit. Planet. Sci.* **42**: 1529–1548.

Sakuma K., Hidaka H., and Yoneda S. (2018) Isotopic and chemical evidence for primitive aqueous alteration in the Tagish Lake meteorite. *Astrophys. J.* **853**: 92.

Sato H., Yui M., and Yoshikawa H. (1996) Ionic diffusion coefficients of Cs^{+}, Pb^{2+}, Sm^{3+}, Ni^{2+}, SeO^{2-}_{4} and TcO^{-}_{4} in free water determined from conductivity measurements. *J. Nuclear Sci. Tech.* **33**: 950–955.

Schenk P., O'Brien D. P., Marchi S., Gaskell R., Preusker F., Roatsch T., Jaumann R., Buczkowski D., McCord T., McSween H. Y., Williams D., Yingst A., Raymond C., and Russell C. (2012) The geologically recent giant impact basins at Vesta's south pole. *Science* **336**: 694–697.

Scherer E. E., Cameron K. L., and Blichert-Toft J. (2000) Lu–Hf garnet chronology: Closure temperature relative to the Sm–Nd system and the effects of trace mineral inclusions. *Geochim. Cosmochim. Acta* **64**: 3413–3432.

Schiller M., Baker J., Creech J., Paton C., Millet M.-A., Irving A., and Bizzarro M. (2011) Rapid timescales for magma ocean crystallization on the howardite–eucrite–diogenite parent body. *Astrophys. J. Lett.* **740**: L22.

Schiller M., Connelly J. N., and Bizzarro M. (2017) Lead and Mg isotopic age constraints on the evolution of the HED parent body. *Meteorit. Planet. Sci.* **52**: 1233–1243.

Schwandt C. S. and McKay G. A. (1998) Rare earth element partition coefficients from enstatite/melt synthesis experiments. *Geochim. Cosmochim. Acta* **62**: 2845–2848.

Shannon R. D. (1976) Revised effective ionic radii and systematic studies of interatomic distances in halides and chalcogenides. *Acta Cryst.* **A32**: 751–767.

Shimamura T. and Lugmair G. W. (1983) Ni isotopic compositions in Allende and other meteorites. *Earth Planet. Sci. Lett.* **63**: 177–188.

Shimizu H., Masuda A., and Tanaka T. (1983) Cerium anomaly in REE pattern of Antarctic eucrite. *Mem. Natl. Inst. Polar Res., Spec. Issue* **30**: 341–348

Shukolyukov A. and Lugmair G. W. (1993a) Live iron-60 in the early solar system. *Science* **259**: 1138–1142.

Shukolyukov A. and Lugmair G. W. (1993b) ^{60}Fe in eucrites. *Earth Planet. Sci. Lett.* **119**: 159–166.

Smoliar M. I. (1993) A survey of Rb–Sr systematics of eucrites. *Meteoritics* **28**: 105–113.

Söderlund U., Patchett P. J., Vervoort J. D., and Isachsen C. E. (2004) The ^{176}Lu decay constant determined by Lu–Hf and U–Pb isotope systematics of Precambrian mafic intrusions. *Earth Planet. Sci. Lett.* **219**: 311–324.

Spergel M. S., Reedy R. C., Lazareth O. W., Levy P. W., and Slatest L. A. (1986) Cosmogenic neutron-capture -produced nuclides in stony meteorites. *J. Geophys. Res.* **91**: 483–494.

Spivak-Birndorf L. J., Wang S.-J., Bish D. L., and Wasylenki L. E. (2018) Nickel isotope fractionation during continental weathering. *Chem. Geol.* **476**: 316–326.

Sprung P., Scherer E. E., Upadhyay D., Leya I., and Mezger K. (2010) Non-nucleosynthetic heterogeneity in non-radiogenic stable Hf isotopes: Implications for early solar system chronology. *Earth Planet. Sci. Lett.* **295**: 1–11.

Steele R. C. J., Elliot T., Coath C. D., and Marcel R. (2011) Confirmation of mass-independent Ni isotope variability in iron meteorites. *Geochim. Cosmochim. Acta* **75**: 7906–7925.

Steele R. C. J., Coath C. D., Regelous M., Russell S., and Elliott T. (2012) Neutron-poor nickel isotope anomalies in meteorites. *Astrophys. J.* **758**: 59.

Steenstra E. S., Knibbe J. S., Rai N., and van Westrenen W. (2016) Constraints on core formation in Vesta from metal–silicate partitioning of siderophile elements. *Geochim. Cosmochim. Acta* **177**: 48–61.

Steiger R. H. and Jäger E. (1977) Subcommission on geochronology: Convention on the use of decay constants in geo- and cosmochronology. *Earth Planet. Sci. Lett.* **36**: 359–362.

Stolper E. (1977) Experimental petrology of eucritic meteorites. *Geochim. Cosmochim. Acta* **41**: 587–611.

Strelow F. W. E., Victor A. H., van Zyl C. R., and Eloff C. (1971) Distribution coefficients and cation exchange behavior of elements in hydrochloric acid–acetone. *Anal. Chem.* **43**: 870–876.

Sugiura N., Miyazaki A., and Q.-Z. Yin (2006) Heterogeneous distribution of 60Fe in the early solar nebula: Achondrite evidence. *Earth Planet Space* **58**: 1079–1086.

Sun C. and Liang Y. (2013) Distribution of REE and HFSE between low-Ca pyroxene and lunar picritic melts around multiple saturation points. *Geochim. Cosmochim. Acta* **119**: 340–358.

Takahashi K. and Masuda A. (1990) Young ages of two diogenites and their genetic implications. *Nature* **343**: 540–542.

Takeda H. (1979) A layered-crust model of a howardite parent body. *Icarus* **40**: 455–470.

Takeda H., Mori H., and Yanai K. (1981) Mineralogy of the Yamato diogenites as possible pieces of a single fall. *Mem. Natl. Inst. Polar Res., Spec. Issue* **20**: 81–99.

Tanaka T., Togashi S., Kamioka H., Amakawa H., Kagami H., Hamamoto T., Yuhara M., Orihashi Y., Yoneda S., Shimizu H., Kunimaru T., Takahashi K., Yanagi T., Nakano T., Fujimaki H., Shinjo R., Asahara Y., Tanimizu M., and Dragusanu C. (2000) JNdi-1: A neodymium isotopic reference in consistency with LaJolla neodymium. *Chem. Geol.* **168**: 279–281.

Tang H. and Dauphas N. (2012) Abundance, distribution, and origin of ^{60}Fe in the solar protoplanetary disk. *Earth Planet. Sci. Lett.* **359–360**: 248–263.

Taylor P. D. P., Maeck R., and Blévre P. (1992) Determination of the absolute isotopic composition and atomic weight of a reference sample of natural iron. *Int. J. Mass Spectrom. Ion. Processes* **121**: 111–125.

Teng F. Z. and Yang Y. (2013) Comparison of factors affecting the accuracy of high-precision magnesium isotope analysis by multi-collector inductively coupled plasma mass spectrometry. *Rapid Commun. Mass Spectrom*. **28**: 19–24.

Touboul M., Sprung P., Aciego S. M., Bourdon B., and Kleine T. (2015) Hf–W chronology of the eucrite parent body. *Geochim. Cosmochim. Acta* **156**: 106–121.

Trinquier A., Brick J.-L., Allègre C. J., Göpel C., and Ulfbeck D. (2008) ^{53}Mn–^{53}Cr systematics of the early Solar System revisited. *Geochim. Cosmochim. Acta* **72**: 5146–5163.

Victor A. H. (1986) Separation of nickel from other elements by cation-exchange chromatography in dimethylglyoxime/hydrochloric acid/acetone media. *Anal. Chim. Acta* **183**: 155–161.

Wahlgren M., Orlandini K. A., and Korkisch J. (1970) Specific cation-exchange separation of nickel. *Anal. Chim. Acta* **52**: 551–553.

Wasson J. T. and Kallemeyn G. W. (1988) Composition of chondrites. *Philos. Trans. Royal Soc. A* **325**: 535–544.

Welten K. C., Lindner L., van der Borg K., Loeken T., Scherer P., and Schultz L. (1997) Cosmic-ray exposure ages of diogenites and the recent collisional history of the howardite, eucrite and diogenite parent body/bodies. *Meteorit. Planet. Sci.* **32**: 891–902.

Wilson L. and Keil K. (1996) Volcanic eruptions and intrusions on the asteroid 4 Vesta. *J. Geophys. Res.* **101**: 18927–180940.

Wu G., Zhu J.-M., Wang X., Han G., Tan D., and Wang S.-J. (2019) A novel purification method for high precision measurement of Ni isotopes by double spike MC-ICP-MS. *J. Anal. At. Spectrom.* **34**: 1639–1651.

Yamaguchi A. Barrat J.-A., Greenwood R. C., Shirai N., Okamoto C., Setoyanagi T., Ebihara M., Franchi I. A., and Bohn M. (2009) Crustal partial melting on Vesta: Evidence from highly metamorphosed eucrites. *Geochim. Cosmochim. Acta*. **73**: 7162–7182.

Yamaguchi A., Barrat J.-A., Ito M., and Bohn M. (2011) Posteucritic magmatism on Vesta: Evidence from the petrology and thermal history of diogenites. *J. Geophys. Res.* **116**: E08009.

Yamaguchi A., Barrat J.-A., Shirai N., and Ebihara M. (2015) Petrology and geochemistry of Northwest Africa 5480 diogenite and evidence for a basin-forming event on Vesta. *Meteorit. Planet. Sci.* **50**: 1260–1270.

Yamaguchi A., Mikouchi T., Ito M., Shirai N., Barrat J.-A., Messenger S., and Ebihara M. (2013) Experimental evidence of fast transport in planetary basaltic crusts by high temperature metamorphism. *Earth Planet. Sci. Lett.* **368**: 101–109.

Yang Y.-H., Zhang H.-F., Chu Z.-Y., Xie L.-W., and Wu F.-Y. (2010) Combined chemical separation of Lu, Hf, Rb, Sr, Sm and Nd from a single rock digest and precise and accurate isotope determinations of Lu–Hf, Rb–Sr and Sm–Nd isotope systems using Multi-Collector ICP-MS and TIMS. *Int. J. Mass Spectrom.* **290**: 120–126.

Yao L., Sun C., and Liang Y. (2012) A parameterized model for REE distribution between low-Ca pyroxene and basaltic melts with applications to REE partitioning in low-Ca pyroxene along a mantle adiabat and during pyroxenite-derived melt and peridotite interaction. *Contrib. Mineral. Petrol.* **164**: 261–280.

Yokoyama T., Fukai R., and Nakahara M. (2020) Separation of heavy lanthanoids by flash column chromatography for precise determination of Er and Yb isotope compositions in rock samples. *Geostand. Geoanal. Res.* **44**: 265–285.

Zanetti A., Tiepolo M., Oberti R., and Vannucci R. (2004) Trace-element partitioning in olivine: Modelling of a complete data set from a synthetic hydrous basanite melt. *Lithos* **75**: 39–54.

Zhou Q., Yin Q.-Z., Bottke B., Claeys P., Li X.-H., Wu F.-Y., Li Q.-L., Liu Y., and Tang G.-Q. (2011) Early basaltic volcanism and late heavy bombardment on Vesta: U–Pb ages of small zircons and phosphates in eucrites. *Lunar Planet. Sci.* **XXXXII**: #2575 (abstract).

Zolensky M. E., Weisberg M. K., Buchanan P. C., and Mittlefehldt D. W. (1996) Mineralogy of carbonaceous chondrite clasts in HED meteorites and the Moon. *Meteorit. Planet. Sci.* **31**: 518–537.

Supporting research papers

Saito T., Hidaka H., and Lee S.-G. (2019) ^{176}Lu–^{176}Hf and ^{87}Rb–^{87}Sr systematics and rare earth element abundances of nine diogenite meteorites: Evidence for their crystallization from partial melts of the Vestan mantle. *Astrophys. J.* **877**: 73.

Saito T., Hidaka H., and Yoneda S. (in press) Sm and Gd isotopic shifts in eucrites and implications for their cosmic-ray exposure history. *Astrophys. J.*